$CaCO_3$ DECOMPOSITION ENHANCED BY DIELECTRIC BARRIER DISCHARGE PLASMA.

THE EFFECT OF PLASMA-CATALYSIS.

Guido Giammaria

UNIVERSITY OF TWENTE.

$CaCO_3$ DECOMPOSITION ENHANCED BY DIELECTRIC BARRIER DISCHARGE PLASMA.

THE EFFECT OF PLASMA-CATALYSIS.

Guido Giammaria

The dissertation has been approved by:

Supervisor: Prof. Dr. Ir. L. Lefferts

The research described in this thesis was carried out at the Catalytical Processes and Materials (CPM) group of the University of Twente, the Netherlands. This work is part of the research program “CO2-neutral fuels” with project number 13CO23-2, which is financed by the Netherlands Organization for Scientific Research (NWO).

NWO
Applied and
Engineering Sciences

Cover design: Guido Giammaria
Printed by: Gildeprint, Enschede, The Netherlands
Lay-out: Guido Giammaria
ISBN: 978-90-365-4943-1
DOI: 10.3990/1.9789036549431

$CaCO_3$ DECOMPOSITION ENHANCED BY DIELECTRIC BARRIER DISCHARGE PLASMA.

THE EFFECT OF PLASMA-CATALYSIS.

Dissertation

to obtain
the degree of doctor at the University of Twente
on the authority of the Rector Magnificus
Prof. Dr. T. T. M. Palstra
on account of the decision of the Doctorate Board,
to be publicly defended
on Friday 7th of February 2020 at 12:45

By

Guido Giammaria

born on the 22nd of November 1985
in Anagni, Italy

Graduation Committee:

Chairman:

Prof. Dr. J. L. Herek	University of Twente

Supervisor:

Prof. Dr. Ir. L. Lefferts	University of Twente

Members:

Prof. C. Hardacre	University of Manchester
Dr. V. Meynen	University of Antwerp
Prof. G. J. van Rooij	Technical University of Eindhoven
Prof. G. J. Kramer	University of Utrecht
Prof. J. G. E. Gardeniers	University of Twente
Prof. S. Kersten	University of Twente

Table of contents

Summary

This research aims at the assessment of potential benefits of a Dielectric Barrier Discharge (DBD) non-thermal plasma on the calcium carbonate decomposition, in terms of 1) decomposition temperature decrease and 2) direct conversion to added value chemicals such as CO.

Calcium carbonate decomposition is the regeneration step of the Calcium Looping Cycle, a process to separate CO_2 from flue gases, preventing global warming. In order to efficiently purify a continuous stream from CO_2, we need to recycle the sorbent calcium oxide every time it's highly converted to $CaCO_3$, via decomposition. Unfortunately, $CaCO_3$ decomposition involves very high temperatures, leading to structure instability. Furthermore, the extracted CO_2 must be converted, since storage is highly discouraged.

DBD plasma is a promising technique since it activates very stable molecules like CO_2 at temperatures lower than 100°C. This is due to the strong unbalance between the energies in the plasma: very high for the electrons and for the vibrational modes of the molecules, which seem to channel the activation of CO_2 with less energy cost, rather low for the heavy molecules motion (i.e. temperature). Low temperatures allow solid materials inside the plasma zone, e.g. the decomposing calcium carbonate or any catalyst for further CO_2 conversion. DBD plasma can be also generated and sustained at atmospheric pressure, which is very interesting for applications.

The effect of DBD plasma on $CaCO_3$ decomposition is studied using a systematic approach: firstly, a pure physical plasma is tested by using argon as inert phase. Successively, reactive gases as hydrogen and water vapour are introduced to test any plasma chemistry. The kinetics of the thermal decomposition reaction (without plasma) are also evaluated at the same conditions, serving as blank experiments. A method to distinguish between thermal effect (i.e. increase of temperature) and non-thermal effects of plasma, either physical or chemical, is developed in order to assess the real benefit of plasma. Any effect of plasma beside thermal is considered favourable, since it would allow to lower the decomposition temperature preventing sintering. Any secondary reaction, i.e. conversion of CO_2 to CO or CH_4, will be also evaluated and reported as additional benefit for energy storage application.

The kinetics of $CaCO_3$ decomposition in absence of plasma are addressed in Chapter 2, both in pure argon and in presence of low concentrations of water vapour. We investigate whether steam has a catalytic effect on the decomposition, by comparing the kinetics of the reaction with and without steam by minimizing any mass and heat transfer limitation.

The new method developed to distinguish between thermal and non-thermal effects of plasma in a packed bed DBD reactor is discussed in Chapter 3. The method is tested on calcium carbonate decomposition in argon plasma and consecutive CO_2 decomposition, allowing to discriminate which effect of plasma drives the reaction kinetics and estimate the temperature in the plasma.

In Chapter 4, the Reverse Water Gas Shift (RWGS) reaction is probed in presence of calcium oxide and plasma, as a pre-requirement to study calcium carbonate decomposition in presence of hydrogen plasma. Synergy between calcium oxide and plasma for RWGS is assessed and discussed by discriminating whether it is produced by a thermal effect, by an effect of calcium oxide on the plasma or by new reactions of plasma on the calcium oxide surface.

In Chapter 5, the decomposition of calcium carbonate in hydrogen plasma is addressed, by using the kinetic data obtained for RWGS. The research questions discussed are 1) the effect of hydrogen on the decomposition without plasma, 2) the effect of hydrogen plasma on the decomposition and 3) whether the CO is produced via consecutive RWGS or via direct decomposition of bulk carbonate.

In Chapter 6, the conclusions of this work are summarized, and other routes explored during this research are briefly shown, i.e. $CaCO_3$ decomposition in presence of water vapour plasma and transition metals-doped $CaCO_3$ decomposition in presence of hydrogen. A general assessment on this technology is drawn, together with a few ideas for the future.

Samenvatting

Dit onderzoek is gericht op de evaluatie van mogelijke voordelen van een niet-thermische ‘Dielectric Barrier Discharge’ (Diëlektricum barrière ontlading; DBD) op de calciumcarbonaatontleding, in termen van 1) afname van de ontledingstemperatuur en 2) directe conversie naar chemicaliën met toegevoegde waarde zoals CO.

Calciumcarbonaatontleding is de regeneratiestap in de Calcium Looping Cycle, een proces om CO_2 van rookgassen te scheiden om zo broeikasgasuitstoot de limiteren. Om CO_2 efficiënt van een continue stroom te zuiveren moeten we het sorptiemiddel calciumoxide regenereren elke keer dat het door ontleding in grote mate wordt omgezet in $CaCO_3$. Helaas betreft $CaCO_3$-ontleding zeer hoge temperaturen, wat leidt tot instabiliteit van de structuur. Bovendien, moet de geëxtraheerde CO_2 worden omgezet, omdat opslag sterk wordt afgeraden.

DBD plasma is een veelbelovende techniek, omdat het zeer stabiele moleculen zoals CO_2 bij temperaturen lager dan 100°C activeert. Dit komt door de sterke onbalans tussen de energieën in het plasma: zeer hoog voor de elektronen en voor de vibratiemodi van de moleculen, maar vrij laag voor de beweging van de zware moleculen (d.w.z. temperatuur). Vibrationele activering van CO_2 lijkt te leiden tot een lager benodigde energie. Lagere temperaturen laten plaatsen van vaste materialen binnen de plasmazone toe, b.v. het ontledende calciumcarbonaat of een katalysator voor verdere CO_2-omzetting. DBD-plasma kan ook worden gegenereerd en in stand gehouden worden onder atmosferische druk, wat zeer interessant is voor toepassingen.

Het effect van DBD-plasma op de ontleding van $CaCO_3$ wordt bestudeerd door middel van een systematische aanpak: ten eerste wordt een zuiver fysiek plasma getest met argon als inerte fase. Achtereenvolgens worden reactieve gassen zoals waterstof en waterdamp geïntroduceerd om elke plasmachemie te testen. De kinetiek van de thermische ontledingsreactie (zonder plasma) wordt ook geëvalueerd onder dezelfde omstandigheden. Deze experimenten zullen als blanco fungeren. Om onderscheid te maken tussen thermisch effect (d.w.z. toename van temperatuur) en niet-thermische effecten van plasma, fysisch of chemisch, is een methode ontwikkeld om het werkelijke voordeel van plasma te beoordelen. Elk effect van plasma naast thermisch wordt als gunstig beschouwd, omdat het de ontledingstemperatuur zou kunnen verlagen om zo

sinteren kan voorkomen. Elke secundaire reactie, d.w.z. omzetting van CO_2 in CO of CH_4, zal ook worden geëvalueerd en gerapporteerd als extra voordeel voor toepassing van energieopslag.

De kinetiek van $CaCO_3$-ontbinding in afwezigheid van plasma in zowel zuiver argon als in aanwezigheid van lage concentraties waterdamp zal worden behandeld in Hoofdstuk 2. We onderzoeken of stoom een katalytisch effect heeft op de ontleding, door de kinetiek van de reactie te vergelijken met en zonder stoom door massa en warmteoverdracht te minimaliseren.

In Hoofdstuk 3 wordt een nieuwe methode besproken die is ontwikkeld om onderscheid te kunnen maken tussen thermische en niet-thermische effecten van plasma in een gepakte DBD-reactor. De methode wordt getest op calciumcarbonaatontleding in argonplasma en opeenvolgende CO_2-ontleding, waardoor kan worden bepaald welk effect van het plasma de reactiekinetiek stuurt. Hiernaast kan met deze methode een schatting worden gemaakt van de temperatuur in het plasma.

Als een vooronderzoek om de ontleding van calciumcarbonaat te bestuderen in aanwezigheid van waterstofplasma wordt in Hoofdstuk 4 de Reverse Water Gas Shift (RWGS) reactie onderzocht in aanwezigheid van calciumoxide en plasma. Synergie tussen calciumoxide en plasma voor RWGS wordt beoordeeld en besproken door te onderscheiden of het wordt geproduceerd door een thermisch effect, door een effect van calciumoxide op het plasma of door nieuwe reacties van plasma op het calciumoxideoppervlak.

In Hoofdstuk 5 wordt de ontleding van calciumcarbonaat in waterstofplasma behandeld met behulp van de kinetische gegevens die zijn verkregen voor RWGS. De besproken onderzoeksvragen zijn 1) het effect van waterstof op de ontleding zonder plasma, 2) het effect van waterstofplasma op de ontleding en 3) of het CO wordt geproduceerd via opeenvolgende RWGS of via directe ontleding van bulkcarbonaat.

In Hoofdstuk 6 worden de conclusies van dit werk samengevat en andere routes die tijdens dit onderzoek zijn verkend kort weergegeven, d.w.z. $CaCO_3$-ontleding in aanwezigheid van waterdampplasma en met overgangsmetalen gedoteerde $CaCO_3$-ontleding in aanwezigheid van waterstof. Er wordt een algemene beoordeling van deze technologie gemaakt, samen met enkele ideeën voor de toekomst.

Chapter 1

Introduction

1.1 Global warming and energy economy

After tough negotiations, on 12 December 2015 most of the countries in the World signed the Paris Agreement, which main concerns are 1) to limit the increase of the global temperature "to well below 2 °C above pre-industrial levels and to pursue efforts to limit the temperature increase to 1.5 °C" and 2) to reduce poverty in the less developed countries [1]. To achieve these objectives, the net carbon emission should reach level zero by 2050 and major efforts must be made by the western World.

Therefore, the global economy must change. Figure 1.1 shows that the energy demand is rapidly increasing in the last 25 years [2]. Nowadays, 80 to 90% of the energy feedstock is still composed by carbon sources, which contribute to emit CO_2 in the atmosphere and must be eventually replaced by hydrogen, biofuels or renewable electrical energy from solar and wind. Figure 1.2 shows the levelized cost of electricity produced in power plants using different renewable technologies and commissioned either on 2010 or on 2018 [3]. As a comparison, it shows also the cost range of energy generated by fossil sources. Thanks to recent advancements in renewable technologies, the price of renewable electrical energy dropped significantly, especially in case of hydropower and geothermal, which are currently cheaper than energy from fossil sources, since they cost less than 0.1 USD kWh^{-1}.

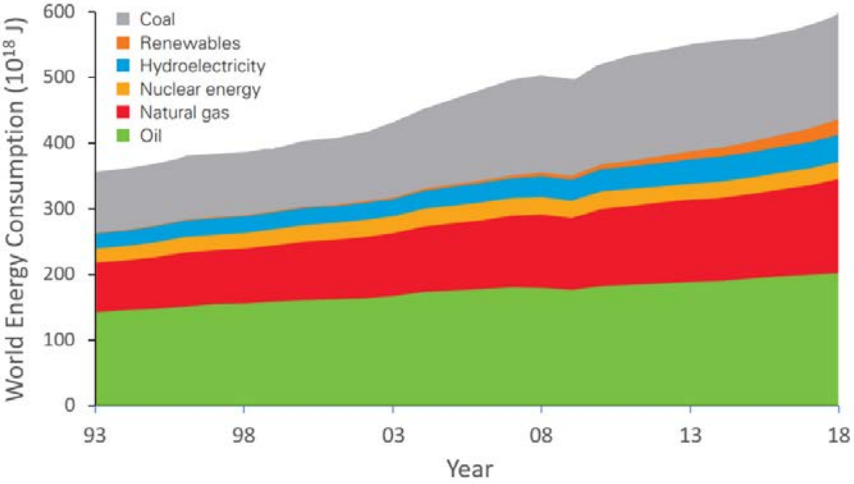

***Figure 1.1**: Global energy consumption by source in the last 25 years, adapted from [2].*

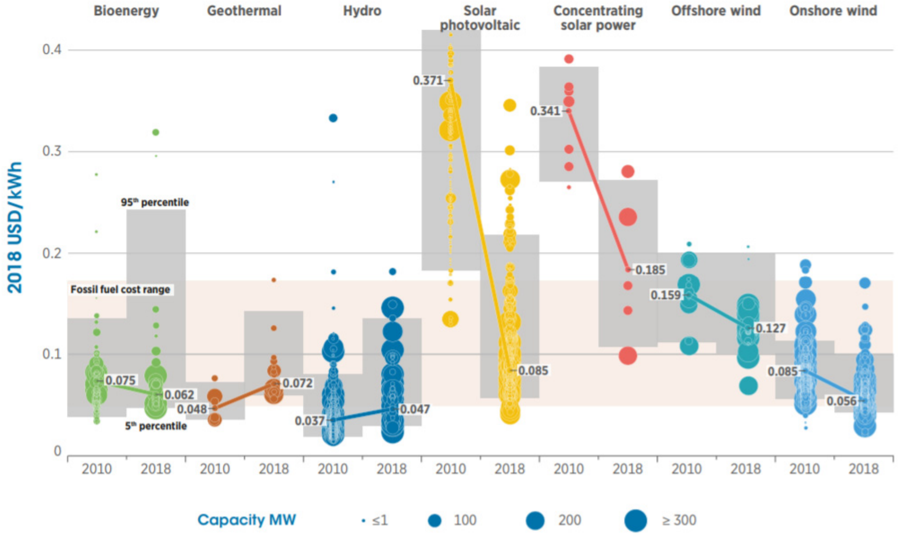

***Figure 1.2**: Global levelized cost of electricity from utility-scale renewable power generation technologies, 2010-2018. The diameter of the circles represents the size of the project. The vertical bars represent the interval of costs between percentiles 5 and 95 for each technology. The horizontal bar indicates the cost range of fossil fuels [3].*

Although it seems that the rapid increase in efficiency would allow electrification, renewable technology will not replace fossil fuels in the next decade for two logistic reasons, i.e. 1) renewable energies are intermittent and storage is an issue and 2) they aren't located homogeneously on the Earth and transportation is also an issue, e.g. the sun shines more intense on the equator, while most of the energy demanding countries (US, European Union, China) are far from the equator [4]. Furthermore, there is one economical reason, which is that the major players in the energy economy, sometimes supported by local administrations, would rather rely on still durable fossil sources than invest on renewable sources, e.g. the United states can still rely on natural gas for 90 years and on coal for 300 years [5].

Therefore, CO_2 emissions won't be avoided sufficiently to allow a carbon-neutral economy, but they can be prevented to reach the atmosphere by applying technologies for CO_2 separation and conversion.

1.2 Carbon Capture and Storage or Utilization

Carbon Capture and Storage (CCS) or Utilization (CCU) refers to a set of technologies being developed for the capture, transport, storage and utilization of CO_2. Great research efforts have been performed in the last decades on CO_2 separation from flue gases, syngas and ambient air. Figure 1.3 summarizes the current development progress of different CCS technologies on the Technology readiness level (TRL) scale [6]. The most populated regions are TRL 3, TRL 6 and TRL 7 development phases. The progression of a technology beyond TRL 3 requires further research funding, whereas advancing technologies beyond TRL 7 and finally introducing them into commerce needs significant financial investments and commercial interest.

The most developed option (TRL9) is flue gas scrubbing using amine-based sorbents [7], which has been utilized in two commercial-scale post-combustion capture facilities in coal-fired power plants, Boundary Dam [8] and Petra Nova [9]. Amine-based sorbents, e.g. mono-ethanolamine, react strongly with acid gases like CO_2 and has an ability to remove high fractions of CO_2, even at the low CO_2 concentrations [10]. Typically, Mono-ethanolamine can capture 85% to 90% of the CO_2 from the flue gas of a coal-fired plant, which is one of the most effective solvent to capture CO_2. However, the interaction of these sorbents with sulphur-oxide and oxygen, always present in flue gases, as well as their corrosive nature, represent a major issue for its operation.

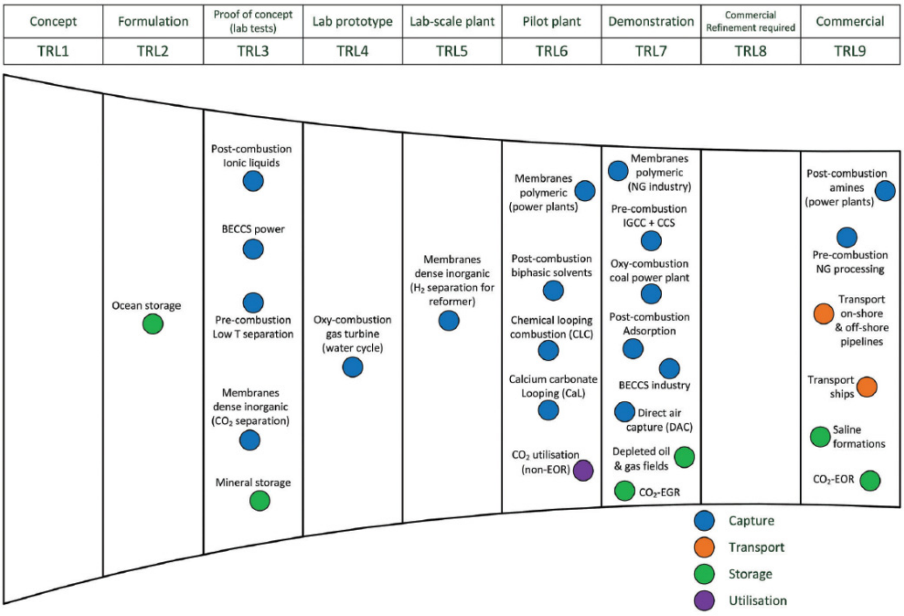

Figure 1.3: *State of the art for CCS and CCU technologies development [6]. The circles represent different technologies and are shown as function of the TRL achieved so far.*

Technologies based on polymeric membranes are also developed until demonstration level (TRL7). The Polaris membrane has been tested in pilot plants (1 MW) to remove CO_2 from syngas at room temperature and pressures up to 40 bar [11]. Membranes which can stand high temperatures applicable in power plants are indeed more challenging and still under development [12].

A rather new hot topic is CO_2 capture directly from air, although the very low CO_2 concentration present in air makes it much less efficient respect to operating on flue gases. A first plant for Direct Air Capture (DAC) was recently opened in Hinwil, Switzerland, which is capable to remove 900 tons CO_2/year [13].

Adsorption processes have been researched from the early 1990s, aiming at the development of adsorbents with high CO_2 capture capacity, high CO_2 selectivity and tolerance towards impurities. For this purpose, both classical materials, e.g. metal oxides, zeolites and carbons, and new materials, e.g. metalorganic frameworks, hydrotalcites and polymers, have been explored [14].

The main advantage of CO_2 capture via adsorption on solids is that it can be fitted to old plants with minor modifications, leading to low footprint and costs. In addition, these technologies can be applied in a large range of temperatures and pressures by choosing the right sorbent, allowing different applications. Moreover, solid sorbents are much more stable and then safer than amine sorbents, which makes such technology the way to follow [15].

Nevertheless, several challenges have still to be addressed, which blocked this technology at the pilot plant stage (TRL7). For instance, process design is still an issue, since 1) adsorption is by nature an exothermic process and heat dissipation has to be managed in order to avoid high temperature raises [16] and 2) the process requires regeneration of the sorbent in a separate step, induced either by pressure swing or temperature swing. Vacuum Swing Adsorption (VSA) has been tested for post-combustion capture [17], although the major challenge is the energy cost, since high vacuum is required in order to have high CO_2 concentration in the outlet (i.e. 10 kPa for 95% CO_2) [18]. Temperature Swing Adsorption is much more attractive, since it's scalable and heat is much cheaper than vacuum, but it slows down the process significantly, since heating and cooling takes time [19].

1.3 Calcium Looping Cycle

A valid alternative is mineral carbonation of calcium oxide. Although the idea of using lime to capture CO_2 is ca 100 years old, just at the end of the 1990s the Calcium Looping Cycle (CLC) process was proposed by Shimizu et al. [20]. The CLC consists in two fluidized beds for CaO carbonation (for capture) and calcination (for recycling) respectively, which is capable to scrub CO_2 from flue gases. A scheme of the CLC process is presented in figure 1.4 [6]. The carbonation is an exothermic reaction ($\Delta H_0 = -179$ kJ/mol) [21] but is kinetically hindered, therefore must be performed at elevated temperatures (600°C) to speed up the process. The calcination is endothermic and requires high temperatures in order to achieve high CO_2 concentrations in the outlet (> 950°C to have 100% CO_2 at atmospheric pressure) [22].

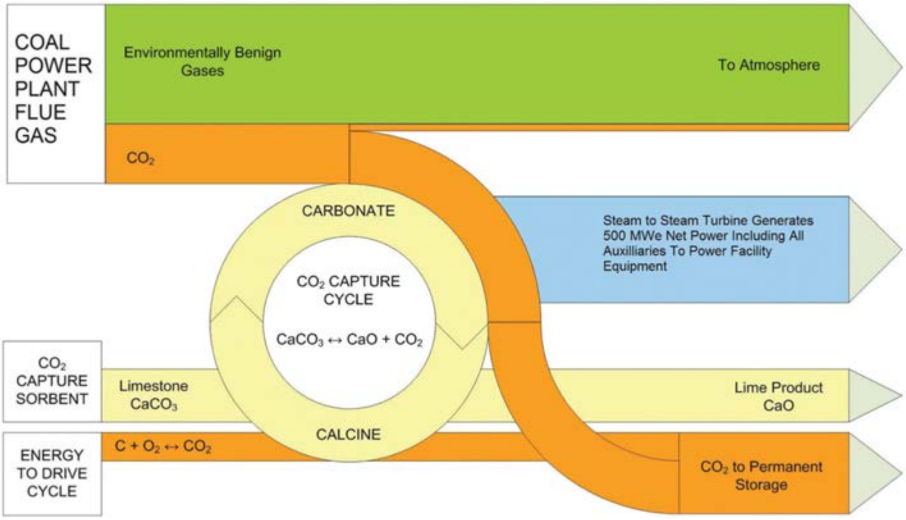

***Figure 1.4**: Schematic of the CLC process [6].*

The CLC process has several advantages. Firstly, the heat lost in the absorber and the calciner can be recovered via a steam cycle, producing more power. Secondly, the raw material is calcite, one of the most abundant and cheapest on earth. Finally, cement industry would make a good use of spent calcium oxide as construction material, allowing to cut the disposing costs [23]. Moreover, the high temperatures involved are well suitable for flue gases.

The main disadvantage is that calcination temperatures result in sintering, decreasing the CO_2 capture capacity when calcium oxide is recycled several times [24]. The impact of cycling on the calcium oxide microstructure has been widely studied and substantial decrease of the surface area as well as closure of meso- and micro- pores were reported [25]. Several attempts have been made to enhance the long-term capture capacity of calcium oxide, by e.g. exploring different synthesis methods and precursors as well as addition of oxides as support material, mixing with other elements, doping, core-shell materials and nano-structured composites were explored [26]. Moreover, CLC also needs repetitive temperature swings, which means switching reactor or moving beds, either way slowing down the process.

Clearly, there is need to replace heat generated from fossil fuels with another source of energy for the calcination reaction, but no definitive solution is found so far. The use of co-reactants like H_2 and H_2O seems to reduce the decomposition temperature to some extent [27, 28], although the effects of such gases on the decomposition are still under investigation. Heating up with an electrical oven would allow much faster temperature swings than burners and pricewise it seems a viable solution, since the lower price of renewable energy as discussed above, but the heat provided by electrical sources still leads to sintering of $CaCO_3$. Besides classical heat, other techniques are being explored. For instance, calcium carbonate in aqueous solution has been decomposed in electrochemical cells producing calcium bicarbonate for CO_2 storage in the ocean [29]. Calcium carbonate has also been decomposed in microwaves [30], which have been proven to heat up the dielectric materials surface rather than the bulk [31]. Anisotropic heating is also studied in non-thermal plasmas, which is the topic of this thesis and will be explained more in detail in the following paragraph. As additional benefit, non-thermal plasmas enable CO_2 activation and conversion [32], which is interesting for energy storage.

1.4 Non-thermal plasma for $CaCO_3$ decomposition and CO_2 conversion

1.4.1 General

Plasma is referred as the fourth state of matter. It is composed by a gas with a significant number of electrons not bound to their molecules, which are in turn converted into positive reactive ions and vibrationally activated molecules. Both ions and activated molecules are referred to *active species*, which make the plasma a conductive media, internally interactive and responsive to electromagnetic fields [33].

Plasma is a multicomponent system and can exhibit multiple temperatures. At the beginning of plasma generation, electrons get kinetic energy from the electric field, which means they initially have much higher temperature than the rest of the species [33]. Successively, collisions between electrons and heavy particles distribute the excess energy and equilibrate the temperature. A plasma in a quasi-equilibrium state is defined *thermal*, otherwise *non-thermal*.

1.4.2 Non-thermal plasma

Non thermal plasma can exist very far away from equilibrium, since it provides high concentrations of chemically reactive species while keeping bulk temperatures as low as room temperature. The electron temperature is the highest in the system, typically between 10^4 and 10^5 K, followed by the temperature of the vibrational excitations of molecules, on the order of 10^3 K, while the translational temperature of the heavy species is at the most 10^1-10^2 K higher than the applied temperature [33]. The fact that the plasma energy is channelled much more selectively to specific molecular bonds respect to conventional thermal energy, makes a non-thermal plasma suitable for chemical processes.

Non thermal plasma is usually generated either at low pressures or at low power levels, or in kind of pulsed discharge systems. In literature, a non-thermal plasma is named in different ways, based on the technique used to generate it (e.g. Dielectric Barrier Discharge, Plasma needle, Plasma jet), and on the characteristics of the plasma itself (e.g. filamentary discharge, glow discharge and surface discharge) [33]. Non-thermal plasmas have several applications in the fields of catalysis, such as waste gas treatment, CO_2 conversion and reforming of hydrocarbons [34, 35], food treatment [36] and medicine [37]

1.4.3 Dielectric Barrier Discharge

Dielectric Barrier Discharge plasma (DBD) is especially attractive for catalytic applications, since it can be easily integrated in a catalytic reactor. Figure 1.5 shows a typical schematic of a DBD setup, which includes the use of a dielectric layer between the two electrodes in order to have several microfilaments uniformly distributed in the plasma zone, instead of a single spark. The applied voltage has an amplitude between 1 and 10 kV and frequency between 10 and 100 kHz, the discharge gap is between 0.1 and 3 cm. DBD is suitable for operation at atmospheric pressure, which makes it very appealing from the perspective of applications [33]

Although DBD plasma is suitable for converting molecules already in the gas phase, often a solid catalyst is added in the plasma zone to enhance the reaction rate or to promote a product by shifting the selectivity [34]. Figure 1.6 shows the two possible configurations of a plasma-catalytic system: either after the plasma zone, which is referred as *post-plasma configuration*, or inside the plasma zone, which is referred as *in-plasma configuration*.

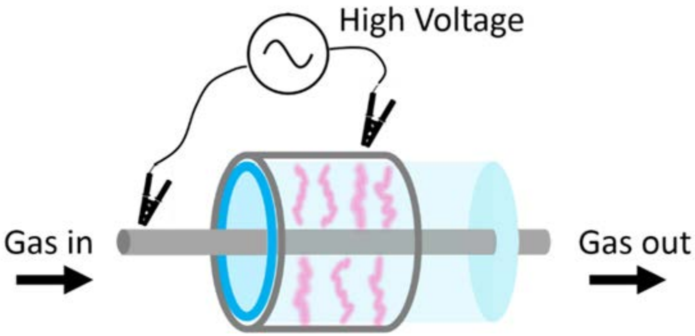

Figure 1.5*: Simplification of a DBD setup. The transparent cylinder is a tubular plug flow reactor, made of a dielectric material. In grey the two electrodes, in pink the electrical micro-filaments.*

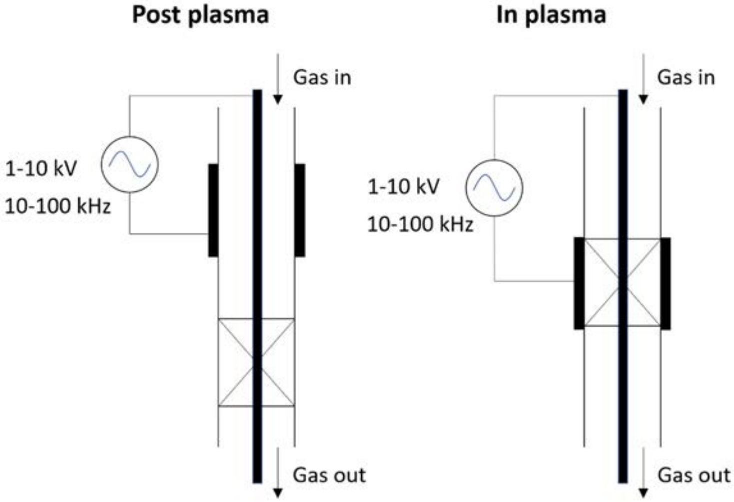

Figure 1.6*: Post-plasma and in-plasma configurations of a DBD reactor. The black rectangles represent the section of the electrodes; the crossed rectangle represents the packed bed.*

In the post-plasma configuration, only the longest living active species interact with the catalyst and the plasma effect on the catalyst is to alter the gas composition on its surface, while the catalyst doesn’t have any effect on the plasma. In the in-plasma configuration, plasma and catalyst are reciprocally influenced in several ways and all the active species can in principle interact with the catalyst [34, 38]. The effects of plasma on the catalyst can be 1) change in gas composition and consequent modification of reaction pathways, 2) physical modification of the catalyst surface and subsurface by etching, poisoning, changing in oxidation state and activation by photon irradiation, and 3) formation of hotspots on the catalyst surface. The effects of the catalyst on the plasma are 1) change in the electric field distribution with enhancement close to the roughness of surface, 2) change in the discharge type, e.g. from filamentary to surface discharge, 3) formation of micro-discharges in pores and 4) presence of pollutants in plasma.

Due to the presence of the mentioned cross-effects, the reaction rate obtained *in-plasma* likely differs from the sum of the reaction rates obtained applying only the catalyst and only the plasma in the reactor at the same conditions of temperature and gases composition. If the former is higher than the latter, it is referred as synergy, which is reported by several studies for different plasma-catalytic reactions [38].

1.4.4 Potential of DBD for CO_2 conversion and $CaCO_3$ decomposition

DBD plasma has a vast range of applications in chemical processes. Ozone generation for water treatment, surface modification via thin films deposition and generation of VUV excimers for lamps and TV displays are already commercially available [39]. Abatement of pollution e.g. VOC, NO_x and SO_x are performed at pilot scale [40], while applications of DBD for energy storage, e.g. coupling of methane [41], conversion of CO_2 into fuels like methanol or syngas [32] and synthesis of ammonia [43] still need further study in the laboratories.

For all these reactions, promising results were presented in terms of high conversion and selectivity, although a major issue of DBD remains the low energy efficiency achieved, i.e., the ratio between chemical energy stored in the produced molecules and electrical energy applied. Focusing on CO_2 conversion, figure 1.7 shows the results in terms of conversion and energy efficiency of a set of studies on CO_2 splitting in DBD and other plasmas [44]. Up to 40% conversion and 15 % efficiency has been obtained using DBD, while much better results have been obtained with microwave plasma, as apparently the CO_2 vibrational states are more selectively excited at microwaves frequencies [45]. Similar trend has been found for CO_2 hydrogenation, CO_2 conversion in presence of water and dry reforming of methane [44]. On the other hand, DBD plasma is much easier to generate and provides better selectivity, since the presence of a catalysts in the plasma zone is not allowed in microwave plasma due to gas temperatures on the order of 1000 K.

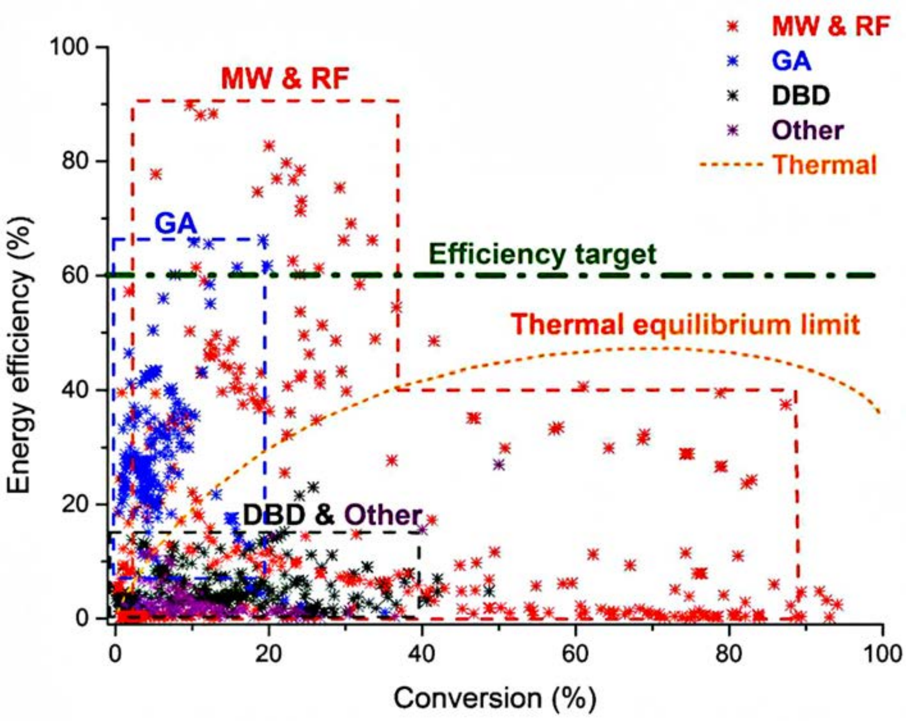

__Figure 1.7__: Conversions and energy efficiencies reported in literature at 2017 for CO_2 splitting in different types of plasma, adapted from [44]. MW stays for microwaves plasma, RF stays for radiofrequency plasma, GA stays for gliding arc plasma.

Whether DBD plasma could enhance the decomposition of calcium carbonate is still unknown. Active species in DBD have energies of typically 10 eV, which rules out erosion and etching processes since they require higher energies [46]. Nevertheless, chemically reactive plasmas, e.g. hydrogen, could react with the surface of calcium carbonate, enabling decomposition at lower temperatures.

1.5 Scope of the thesis

This study aims to report on the effect of DBD plasma on calcium carbonate decomposition in terms of reaction rate and products distribution. Our goal is to assess any enhancement of the decomposition rate and to distinguish whether it is caused by a thermal effect (i.e. increase of the gas temperature), physical or chemical effect of plasma. Any effect of plasma beside thermal is considered favourable, since it would allow to lower the decomposition temperature preventing sintering of $CaCO_3$.

This study is performed systematically: firstly, a pure physical plasma is tested by using argon as inert phase. Successively, reactive gases as hydrogen and water vapour are introduced to test any plasma chemistry. The kinetics of the thermal decomposition reaction (without plasma) are also evaluated at the same conditions, serving as blank experiments. A method to distinguish between thermal effect and physico-chemical effects of plasma is developed in order to assess the real benefit of plasma. Any secondary reaction, i.e. conversion of CO_2 to CO or CH_4, will be also evaluated and reported as additional benefit for energy storage application.

In Chapter 2, the $CaCO_3$ decomposition reaction without plasma in presence of low concentrations of steam in argon is addressed. We investigate whether steam has a catalytic effect on the decomposition, by comparing the kinetics of the reaction with and without steam by minimizing any mass and heat transfer limitation.

In Chapter 3, a new method is developed to distinguish between thermal and non-thermal effects of plasma on reactions occurring on the surface of a packed bed DBD plasma reactor. The method is tested on calcium carbonate decomposition in argon plasma and consecutive CO_2 decomposition, allowing to discriminate which effect of plasma drives the reaction kinetics and estimate the temperature in the plasma.

In Chapter 4, the Reverse Water Gas Shift (RWGS) reaction is probed in presence of calcium oxide and plasma, as a pre-requirement to study calcium carbonate decomposition in presence of hydrogen plasma. Synergy between calcium oxide and plasma for RWGS is assessed and discussed by discriminating whether it is produced by a thermal effect, by an effect of calcium oxide on the plasma or by new reactions of plasma on the calcium oxide surface.

In Chapter 5, the decomposition of calcium carbonate in hydrogen plasma is addressed, by using the kinetic data obtained for RWGS. The research questions discussed are 1) the effect of hydrogen on the decomposition without plasma, 2) the effect of hydrogen plasma on the decomposition and 3) whether the CO is produced via consecutive RWGS or via direct decomposition of bulk carbonate.

In the last chapter the main results of this thesis are summarized and the effect of DBD plasma on calcium carbonate decomposition and consecutive reactions is put into perspective. Other routes explored during this Ph.D., e.g. calcium carbonate decomposition in presence of steam plasma, are shortly discussed.

References

[1] United Nations. Paris agreement, **2015**.

https://unfccc.int/process-and-meetings/the-paris-agreement/the-paris-agreement

[2] BP Statistical Review of World Energy, **2019**.

https://www.bp.com/content/dam/bp/business-sites/en/global/corporate/pdfs/energy-economics/statistical-review/bp-stats-review-2019-full-report.pdf

[3] International Renewable Energy Agency, Renewable Power Generation Costs, **2019**.

https://www.irena.org/publications/2019/May/Renewable-power-generation-costs-in-2018

[4] World Bank Group. Global Solar Atlas, **2019**. *GlobalSolarAtlas.info*.

[5] U.S. Energy Information Administration, **2018**.

https://www.eia.gov/energyexplained/coal/how-much-coal-is-left.php

[6] M. Bui, C. S. Adjiman, A. Bardow, E. J. Anthony, A. Boston, S. Brown, P. S. Fennell, S. Fuss, A. Galindo, L. A. Hackett, J. P. Hallett, H. J. Herzog, G. Jackson, J. Kemper, S. Krevor, G. C. Maitland, M. Matuszewski, I. S. Metcalfe, C. Petit, G. Puxty, J. Reimer, D. M. Reiner, E. S. Rubin, S. A. Scott, N. Shah, B. Smit, J. P. M. Trusler, P. Webley, J. Wilcox, and N. Mac Dowell. Carbon Capture and Storage (CCS): The Way Forward. *Energy and Environmental Science* **2018**, 11, 5, 1062–1176.

[7] R. R. Bottoms. US Patent, application 1783901, **1930**.

[8] M. Campbell. Technology Innovation & Advancements for Shell Cansolv CO_2 capture solvents. *Energy Procedia* **2014**, 63, 801–807.

[9] DOE, Petra Nova – W.A. Parish Project, Office of Fossil Energy, U.S. Department of Energy (DOE), **2017.**

http://energy.gov/fe/petra-nova-wa-parish-project

[10] E. J. Anthony. Carbon Capture and Storage and Carbon Capture, Utilization and Storage 2017. Coal in the 21st century: energy needs, chemicals and environmental controls, *RCS* **2017**, 198-215.

[11] MTR, PolarisTM membrane: CO_2 removal from syngas, Membrane Technology & Research **2017**.

http://www.mtrinc.com/co2_removal_from_syngas.html

[12] Air Products and NTNU Enter Licensing Agreement for Carbon Capture Technology **2019**. *https://www.chemicalprocessing.com/industrynews/2017/air-products-and-ntnu-enter-licensing-agreement-for-carbon-capture-technology/*

[13] J. Owen-Jones, Grand opening of Climeworks commercial DAC plant, Gasworld, **2017**. *https://www.gasworld.com/grand-opening-worlds-first-dac-plant/2012895.article.*

[14] J. A. Arran Gibson, E. Manzago, E. Shiko, A. G. Greenaway, A. V. Gromov, M. M. Lozinska, D. Friedrich, E. E.B. Campbell, P. A. Wright, and S. Brandani. Adsorption Materials and Processes for Carbon Capture from Gas-Fired Power Plants: AMPGas. *Industrial and Engineering Chemistry Research* **2016**, 55, 13, 3840–3851.

[15] J. D. Figueroa, T. Fout, S. Plasynski, H. McIlvried and R. D. Srivastava. Advances in CO_2 Capture Technology—The U.S. Department of Energy's Carbon Sequestration Program. *International Journal of Greenhouse Gas Control* **2008**, 2, 1, 9-20.

[16] K. Kim, Y. Son, W. B. Lee and K. S. Lee. Moving bed adsorption process with internal heat integration for carbon dioxide capture. *Int. J. Greenhouse Gas Control* **2013**, 17, 13–24.

[17] C. Shen, Z. Liu, P. Li and J. Yu. Two-Stage VPSA Process for CO_2 Capture from Flue Gas Using Activated Carbon Beads. *Ind. Eng. Chem. Res.* **2012**, 51, 5011–5021.

[18] S. Krishnamurthy, V. R. Rao, S. Guntuka, P. Sharratt, R. Haghpanah, A. Rajendran, M. Amanullah, I. A. Karimi and S. Farooq. CO_2 capture from dry flue gas by vacuum swing adsorption: A pilot plant study. *AIChE J.* **2014**, 60, 1830–1842.

[19] W. Zhang, H. Liu, C. Sun, T. C. Drage and C. E. Snape. Performance of polyethyleneimine–silica adsorbent for post-combustion CO_2 capture in a bubbling fluidized bed. *Chem. Eng. J.* **2014**, 251, 293–303.

[20] T. Shimizu, T. Hirama, H. Hosoda, K. Kitano, M. Inagaki, and K. Tejima. A Twin Fluid-Bed Reactor for Removal of CO_2 from Combustion Processes. Chem. Eng. Res. Des. **1999**, 77, 62–68.

[21] B. J. McBride, M. J. Zehe, S. Gordon. NASA Glenn Coefficients for Calculating Thermodynamic Properties of Individual Species. NASA/TP-2002-211556

[22] D. P. Hanak, C. Biliyok, E. J. Anthony, and V. Manovic. Modelling and comparison of calcium looping and chemical solvent scrubbing retrofits for CO_2 capture from coal-fired power plant. *Int. J. Greenhouse Gas Control* **2015**, 42, 226–236.

[23] C. Dean, T. Hills, N. Florin, D. Dugwell and P. S. Fennell. Integrating calcium looping CO_2 capture with the manufacture of cement. *Energy Procedia* **2013**, 37, 7078–7090.

[24] R. H. Borgwardt. Sintering of nascent calcium oxide. *Chemical Engineering Science* **1989,** 44, 53-60.

[25] P.S. Fennell, R. Pacciani, J. S. Dennis, J. F. Davidson, and A. N. Hayhurst. The effects of repeated cycles of calcination and carbonation on a variety of different limestones, as measured in a hot fluidized bed of sand. *Energy & Fuels* **2007**, 21, 2072-2081.

[26] W. Liu, N. W. Low, B. Feng, G. Wang, and J.C. Diniz da Costa. Calcium precursors for the production of CaO sorbents for multicycle CO_2 capture. *Environ. Sci. Technol.* **2010**, 44, 841-847.

[27] A. Reller, C. Padeste, and P. Hug. Formation of organic compounds from metal carbonates. *Nature* **1987**, 329, 8, 527-529.

[28] Y. Wang, and W. J. Thomson. The effects of steam and carbon dioxide on calcite decomposition using Dynamic X-Ray Diffraction. *Chemical Engineering Science* **1995**, 50, 9, 1373-1382.

[29] G. H. Rau. Electrochemical splitting of calcium carbonate to increase solution alkalinity: implications for mitigation of carbon dioxide and ocean acidity. *Environ. Sci. Tech.* **2008**, 42, 23, 8935-8940.

[30] M. Fall, G. Esquenazi, S. Allan, and H. Shulman. Rapid Limestone Calcination Using Microwave Assist Technology. *ACEEE Summer Study on Energy Efficiency in Industry* **2011**.

[31] B. García-Baños, J. J. Reinosa, F. L. Peñaranda-Foix, J. F. Fernández, and J. M. Catalá-Civera. Temperature Assessment of Microwave-Enhanced Heating Processes. *Nature Scientific Reports* **2019**, 9, 10809.

[32] B. Ashford, and X. Tu. Non-thermal plasma technology for the conversion of CO_2. *Current Opinion in Green and Sustainable Chemistry* **2017**, 3, 45–49.

[33] A. Fridman. Plasma Chemistry. *Cambridge University Press,* Cambridge, UK, **2008**.

[34] E. C. Neyts, K. Ostrikov, M. K. Sunkara, and A. Bogaerts. Plasma Catalysis: Synergistic Effects at the Nanoscale. *Chemical Reviews* **2015**, 115, 24, 13408–13446.

[35] J. C. Whitehead. Plasma-Catalysis: The Known Knowns, the Known Unknowns and the Unknown Unknowns. *Journal of Physics D: Applied Physics* **2016**, 49, 24, 243001.

[36] N. N. Misra, O. Schlüter, P. J. Cullen. Cold plasma in food and agriculture: fundamentals and applications. *Academic Press* **2016**.

[37] J. Gay-Mimbrera, M. C. García, B. Isla-Tejera, A. Rodero-Serrano, A. V. García-Nieto, and J. Ruano. Clinical and Biological Principles of Cold Atmospheric Plasma Application in Skin Cancer. *Advances in Therapy* **2016**, 33, 6, 894–909.

[38] E. C. Neyts, and A. Bogaerts. Understanding Plasma Catalysis through Modelling and Simulation - A Review. *Journal of Physics D: Applied Physics* **2014**, 47, 22.

[39] U. Kogelschatz “Dielectric-barrier Discharges: Their History, Discharge Physics, and Industrial Applications” Plasma Chemistry and Plasma Processing **2003**, 23, 1, 1-46.

[40] T. Matsumoto, D. Wang, T. Namihira, and H. Akiyama. Air Pollution - A Comprehensive Perspective. Non-Thermal Plasma Technic for Air Pollution Control. InTechOpen **2012**.

[41] T. Nozaki, and K. Okazaki. Non-thermal plasma catalysis of methane: Principles, energy efficiency, and applications. *Catalysis Today* **2013**, 211, 29–38.

[42] C. Boyadjian, A. Agiral, H. Gardeniers, L. Lefferts, and K. Seshan. Oxidative Conversion of Hexane to Olefins-Influence of Plasma and Catalyst on Reaction Pathways. *Plasma Chem Plasma Proc*. **2011**, 31, 291-306.

[43] H. H. Kim, Y. Teramoto, A. Ogata, H. Takagi, and T. Nanba. Atmospheric-Pressure Nonthermal Plasma Synthesis of Ammonia over Ruthenium Catalysts. *Plasma Processes and Polymers* **2017**, 14, 6, 1–9.

[44] R. Snoeckx, and A. Bogaerts. Plasma Technology-a Novel Solution for CO2 Conversion? *Ph.D. thesis* **2017**.

[45] G. J. Van Rooij, D. C. van den Bekerom, N. Den Harder, T. Minea, G. Berden, W. A. Bongers, R. Engeln, M. F. Graswinckel, E. Zoethout, and M. C. M. van de Sanden. Taming microwave plasma to beat thermodynamics in CO_2 dissociation. *Faraday Discuss.* **2015**, 183, 233–248.

[46] R. Behrisch. Sputtering by Particle bombardment. *Springer*, Berlin **1981**. ISBN 978-3-540-10521-3

Chapter 2

Catalytic Effect of Water on Calcium Carbonate Decomposition

Summary

The search for cheap solutions for carbon dioxide capture in order to prevent global warming is still challenging. Calcium oxide may be a suitable sorbent, but the regeneration process from calcium carbonate requires too high temperatures, causing sintering and decreasing sorption capacity. In Chapter 2, the effect of steam on the decomposition of the carbonate is investigated. A clear rate-enhancing effect up to a factor of 4 is observed when steam concentrations up to 1.25% are applied during isothermal reactions at temperatures between 590 and 650°C. This results in a decrease of the apparent activation barrier from 201 to 140 kJ mol^{-1}, caused by the opening of a new reaction pathway. The kinetics of steam catalysed decomposition of $CaCO_3$ is discussed and a simple reaction scheme is proposed, including estimation of kinetic constants. The new pathway proceeds via formation of a stable surface bicarbonate followed by decomposition to surface OH groups, which then decompose by desorbing H_2O.

2.1 Introduction

Global warming caused by emission of greenhouse gases (GHGs) is a major issue both environmentally and economically. Carbon-dioxide, the most important among GHGs, reached an average concentration of more than 0.04%, increasing the global temperature of ca. 1°C above the pre-industrial level [1]. In order to prevent an increase of more than 2°C in the next decades as stated by the Paris Agreement [2], a large implementation of Carbon Capture and Storage (CCS) or Utilization (CCU) as well as low-carbon emission technologies is needed [3].

CCS refers to a group of technologies developed to capture and store CO_2 from combustion in flue gasses of power plants. The most developed option to capture CO_2 is flue gas scrubbing using amine-based sorbents, e.g. monoethanolamide [4, 5]. However, the interaction of these sorbents with sulphur dioxide and oxygen, always present in flue gas, as well as its corrosive nature represent major issues for practical operation. A possible alternative is mineral carbonation of rocks as serpentine $Mg_3Si_2O_5(OH)_4$ or calcium oxide, requiring rather high temperatures [6]. The carbonation (for capture) and calcination (for recycling) of calcium oxide, referred as Calcium Looping Cycle, is widely discussed in literature [7].

However, the calcination reaction requires high temperatures in order to achieve high CO_2 concentrations in the outlet, i.e. at least 950°C to obtain pure CO_2 at atmospheric pressure [8]. Such temperatures result in sintering, decreasing the CO_2 capture capacity when calcium oxide is recycled [9-12]. The impact of cycling on the calcium oxide microstructure has been widely studied and substantial decrease of the surface area as well as closure of meso- and micro- pores were reported [11, 12]. Different synthesis methods and precursors as well as addition of oxides as support material, mixing with other elements, doping, core-shell materials and nano-structured composites were explored in order to improve thermal stability of calcium oxide [13-18]. Another approach would be to induce decomposition at lower temperatures by using a non-thermal plasma, as discussed in this thesis.

The kinetics of calcium carbonate decomposition determines the required residence time and the size of the decomposition reactor in case of moving-bed technology. Unfortunately, kinetic data reported so far are inconsistent [19-22]. A wide distribution of activation energies ranging from 100 to 300 kJ mol-1 are reported in a review by Maciejewski and Reller [23], concluding that the observations are strongly dependent on re-absorption of CO_2, caused by slow transport of CO_2 in the bed. The effect of CO_2 partial pressure on $CaCO_3$ decomposition was also studied by Darroudi and Searcy [24], reporting that CO_2 significantly retards the decomposition even when the reaction is far out of equilibrium.

The effect of water vapour on the decomposition kinetics has been widely investigated as well, but the results are controversial. In first place, it was observed that the presence of water accelerates sintering [25] and the effect was ascribed to an enhancement of surface diffusion. On the other hand, several studies of Anthony et al. report that water regenerates spent sorbents, causing an increase in the capture capacity, as well as reduces sintering if applied during every calcination cycle [26-29]. Several studies observed that the decomposition rate increases substantially when low concentrations of water are present [26, 27, 30, 31], suggesting that water has a catalytic effect on the decomposition reaction. The topic has been explored by Wang and Thompson [32], performing carbonate decomposition in a XRD setup at temperatures below 500°C and water concentrations up to 0.2 bar. They explained the catalytic effect of H_2O with a Langmuir-Hinshelwood kinetic model and reported an increased activation barrier for the new catalytic pathway. Li et al. reported that the enhancement of heat transfer coefficient caused by water causes an increase of the $CaCO_3$ decomposition rate [33]. On the other hand, Kraisha et al. and Yin et al. reported that the combined effect of decreasing CO_2 gas phase diffusivity and increasing heat transfer coefficient induced by water, resulted in an overall decrease in the reaction rate [31, 34].

The methods used up to now to investigate the kinetics of calcium-carbonate decomposition in presence of steam, i.e. TGA and XRD, operate with sample cups containing stagnant gas causing significant mass transfer limitation and consequently re-adsorption of CO_2. The goal of Chapter 2 is to determine the effect of steam on the kinetics of calcium-carbonate decomposition, minimizing mass transfer effects by using a packed-bed in a plug flow reactor, a small amount of a low-surface-area-carbonate and high flow-rate to obtain reliable data. Therefore, the decomposition is studied at relatively low temperature as compared to temperatures used in practice.

2.2 Materials and methods

2.2.1 Sample preparation

In order to study the catalytic effect of H_2O on $CaCO_3$ decomposition, calcium oxide has been synthesized by calcination of calcium L-Ascorbate di-hydrate (99%, Sigma-Aldrich) in 20% O_2 in N_2 at atmospheric pressure and 900°C for 30 min. The calcined product was pelletized (pressure 160 bar), crushed and sieved in order to obtain a sample in form of particles, sized between 250 and 300 µm.

2.2.2 Characterization

The specific surface area, pore volume and pore size distribution of the sample were measured either in CaO form as well as in $CaCO_3$ form, after carbonation. The sample was first degassed at 300°C in vacuum for 3 hours. The BET surface area, pore volume and BJH pore size distribution were calculated based on the N_2 adsorption isotherm at -196°C in a Micrometrics Tristar 3000 analyzer. Crystal structure was determined by means of X-Ray Diffraction in a Bruker D8 spectrometer; crystallite sizes were estimated based on the width of the peaks using the Scherrer equation. The morphology of the samples was characterized with a JEOL-LA6010 Scanning Electron Microscope and the composition was determined with X-Ray Fluorescence analysis (XRF) in a Bruker S8 Tiger. Thermo-Gravimetric Analysis was performed with a Mettler-Toledo TGA/SDTA 851e thermal balance.

2.2.3 Setup

Figure 2.1 shows a schematic representation of the equipment used to measure absorption and desorption of CO_2 on CaO. The fixed bed reactor can be fed with either pure Ar, or a mixture of Ar containing 5% CO_2 or a mixture of Ar and H_2O, varying the H_2O concentration up to 1.25%. Different H_2O concentrations are obtained by diluting the 1.25% H_2O in Ar stream, obtained by bubbling pure Ar in a H_2O reservoir kept at a fixed temperature of 10.5 ± 0.1 °C. The temperature of the oven is controlled by an Eurotherm controller with an accuracy of ±0.5°C between room temperature and

1000°C. The isothermal zone at 900°C is 8 cm long, defined as the position in the reactor with temperature variation less then ±1°C. A Quadrupole Mass Spectrometer Pfeiffer QMS200 measures the composition of the gas downstream of the reactor. The MS signal for CO_2 (44 m/e) is calibrated for CO_2 concentrations between 0.16% and 5%, resulting in a linear relationship as shown in Figure A2.1 of the Appendix A2. The sample, typically 5 mg, is packed in the reactor, a quartz tube with 4-mm inner diameter, together with 70 mg of SiO_2 particles of the same size in order to ensure uniform distribution of the gas flow. SiO_2 is inert to CO_2 and H_2O at the temperatures of operation.

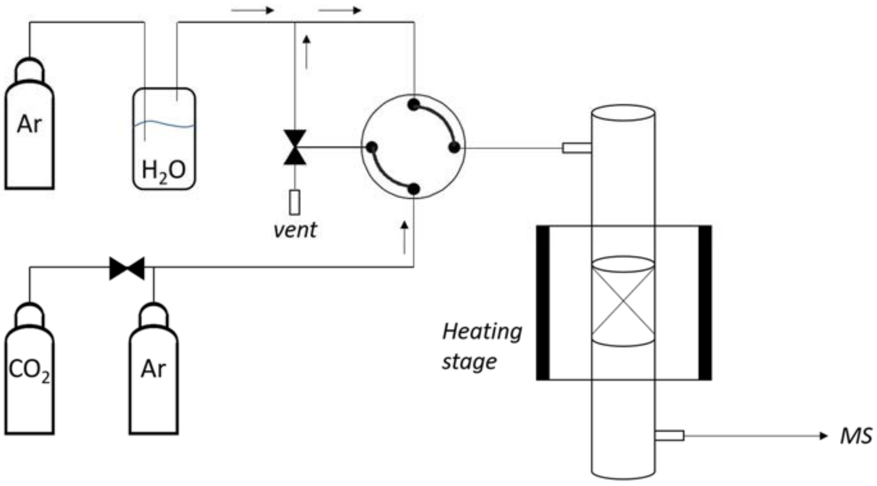

Figure 2.1: *Schematic of the setup to study decomposition of $CaCO_3$.*

2.2.4 Experimental procedure

2.2.4.1 CO_2 absorption

The sample is pre-treated in Ar at 750°C for 30 minutes in order to completely remove absorbed CO_2 and H_2O from ambient. Complete desorption is confirmed by MS analysis. After the pre-treatment, the temperature is decreased and then kept constant at 630°C in order to perform isothermal absorption of CO_2, converting CaO to $CaCO_3$. The experiment starts by instantly changing the composition of the gas from pure Ar to 5%

CO_2 in Ar, while the total flow is always 90 ml min^{-1}. The sample is exposed to CO_2 in a CO_2-Ar mixture until CO_2 absorption diminishes and the sample is saturated. Successively, the sample is heated or cooled to the temperature at which decomposition will be measured.

2.2.4.2 $CaCO_3$ decomposition

The decomposition measurement is initiated by removing CO_2 from the gas mixture, by changing the gas to either pure Ar or Ar containing up to 1.25% H_2O. Isothermal decomposition experiments have been done at four different temperatures, i.e. 590, 610, 630, 650°C, and H_2O concentrations between 0 and 1.25%. These temperatures were selected to ensure sufficiently slow decomposition of $CaCO_3$, preventing too fast exhaustion.

The decomposition is measured by monitoring the CO_2 concentration in the exit of the reactor with MS till complete conversion of $CaCO_3$ has been achieved. Next, the temperature is changed back to 630°C in order to form $CaCO_3$ in 5% CO_2 in Ar for the next measurement.

2.3 Results

2.3.1 Sample characterization

Weight measurement before and after the synthesis using a microbalance as well as the TGA measurement confirm that calcium L-ascorbate decomposed completely to calcium oxide during calcination. Calcium oxide is a reactive material in ambient conditions, since it tends to carbonate and hydrate in a timescale of hours. This influences the BET surface area, varying from 23 m^2/g after 5 minutes exposure to ambient conditions, to 16 m^2/g after several days of exposure. Figure 2.2 shows a thermo-gravimetric analysis (TGA) of a sample stored for several days in ambient conditions, showing that the sample loses around 39% of its mass in two steps. First, $Ca(OH)_2$ decomposes between 350 and 400°C, accounting for 20% of the total weight loss and second, $CaCO_3$ decomposes above 550°C, accounting for the remaining 80%. The sample desorbs 8.6 mmol of water and 18.6 mmol of CO_2, forming 27.7 mmol of

CaO. This implies that CaO is almost completely converted to $Ca(OH)_2$ and $CaCO_3$ in ambient conditions for several days. XRF measurement right after treatment at 1100°C in air shows that the sample is composed of mainly CaO (99.12%) with impurities of SiO_2 (0.16%), MgO (0.12%) and Al_2O_3 (0.095%).

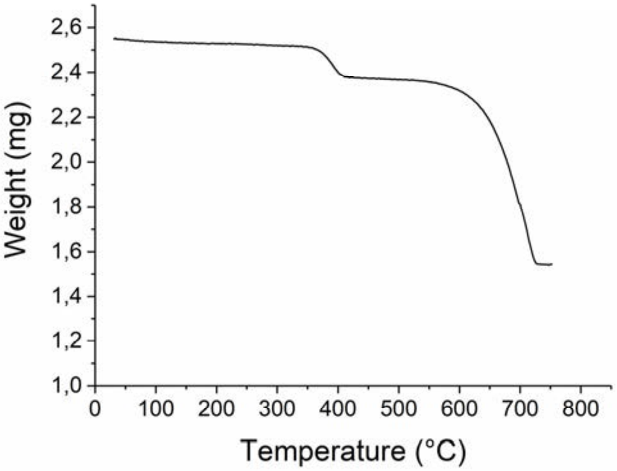

Figure 2.2: *TGA of CaO sample exposed for several days in ambient conditions: heat up from 20 to 750°C at 15°C min^{-1}; isothermal at 750°C for 30 minutes.*

Figure 2.3(a,b) shows XRD and SEM results obtained on samples after several days in ambient conditions. The XRD result shows the most prominent calcite phase of $CaCO_3$ and a relatively small calcium hydroxide peak. The main peak of CaO is also visible, although very low in intensity. This confirms that CaO is almost completely converted to a mixture of $CaCO_3$ and $Ca(OH)_2$ during long exposure to ambient conditions. The average crystal size calculated with the Scherrer equation for $CaCO_3$ is 17 nm, while SEM shows polycrystalline grains in the order of 100 nm. Figure 2.3c shows the XRD spectrum of the same sample after CO_2 absorption: the hydroxide peaks disappeared, while small peaks of calcium oxide are still visible, meaning that the sample is not entirely converted to $CaCO_3$.

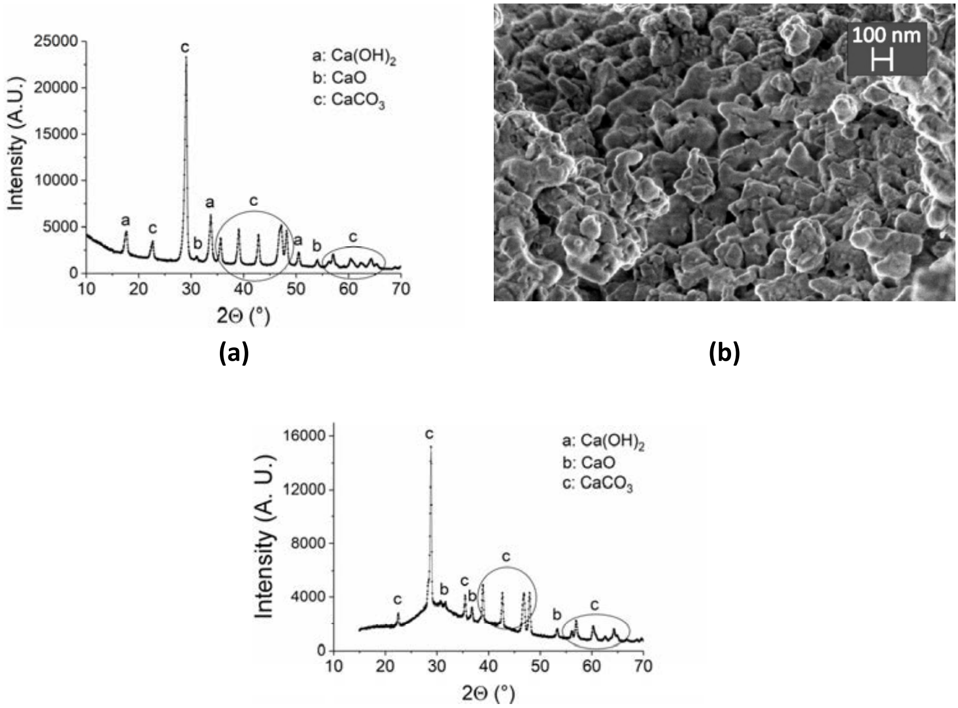

(a) (b)

(c)

***Figure 2.3**: XRD spectrum **(a)** and SEM picture **(b)** of CaO sample after several days of exposure to ambient conditions; XRD spectrum of the sample after CO_2 absorption **(c)**.*

2.3.2 CO_2 absorption – desorption cycles

Figure 2.4a shows a typical example of a CO_2 absorption experiment on a ca. 80 mg CaO sample by measuring the CO_2 concentration during exposure of the catalyst to 5% CO_2 in Ar at 630°C. Clearly, the absorption saturated after typically 20 minutes. It also shows the result of a blank experiment showing that the CO_2 concentration increases to the feed concentration within 10 s when CO_2 is applied. In order to correct for minor variation in the sensitivity, the MS is calibrated for CO_2 based on the signal obtained with the feed composition, assuming linear calibration as presented in figure A2.1. The initial absorption in the first minute is close to the thermodynamic equilibrium. Formation of $CaCO_3$ at such high temperatures induces a significant decrease in surface area to 7 m^2/g, suggesting sintering and/or closure of pores caused by expansion of the material when converting CaO to $CaCO_3$.

Figure 2.4b shows the result of an isothermal decomposition experiment of the $CaCO_3$ layer in Ar, resulting from the absorption experiment in figure 2.4a, showing that the CO_2 concentration generated via decomposition is about constant during the first 2 hours, within 10%. In general, this is observed during decomposition of the first 50% of $CaCO_3$ present initially. The amount of CO_2 absorbed and desorbed are respectively 49.8 and 52.2 mg, resulting in 0.62 ± 0.015 g_{CO2}/g_{CaO}, demonstrating that the mass balance closes within 5%. This amount corresponds approximatively to 79% conversion of CaO. The thickness of the $CaCO_3$ layer is in the order of 35 nm, assuming the surface area is 15 m^2/g, estimated based on the average of the surface areas of 23 to 7 m^2/g for respectively CaO and the carbonated sample. The CO_2 concentration during decomposition in Figure 2.4b is typically 0.35%, implying that the rate of decomposition is not controlled by thermodynamics as the equilibrium CO_2 concentration at 630°C is 0.7% [8]. Nevertheless, it cannot be ruled out that re-adsorption of CO_2 occurs in the bed and therefore the concentration of CO_2 during decomposition was further decreased by decreasing the amount to typically 5 mg carbonated sample, which is equivalent to 3 mg CaO.

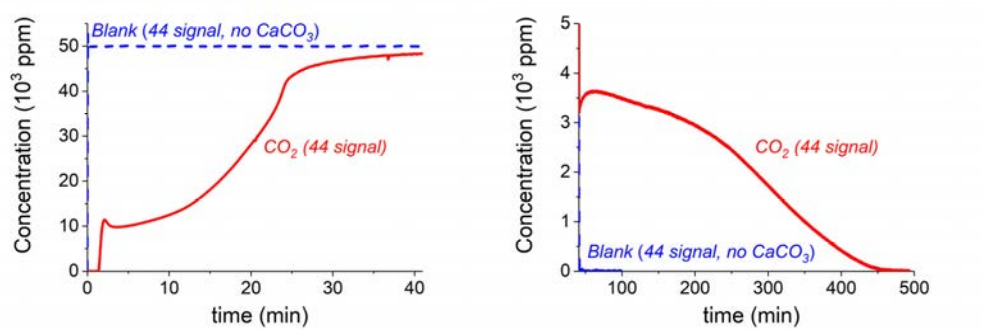

(a) **(b)**

Figure 2.4: *CO_2 concentration (solid line) monitored by Mass Spectrometry during CO_2 absorption* ***(a)*** *and desorption* ***(b)****; the dashed lines on both* ***(a)*** *and* ***(b)*** *present the blank experiments, demonstrating very fast response in both experiments. The amount of CaO is 82 mg, temperature is 630°C, flow-rate is 30 ml min^{-1}, absorption and desorption have been performed respectively in 5% CO_2 in Ar and in pure Ar.*

Figure 2.5 shows the concentration of CO_2 during the initial stage of decomposition during the absorption–desorption cycles at 630°C in absence of H_2O. The CO_2

concentration decreases during the first 40 cycles, indicating a significant aging of the sample. After 40 cycles, the decay partly stabilizes and hereafter experiments were performed with varying temperatures and H_2O concentrations (cycles 41-131). It is well known that continuous recycling of CaO induces sintering and closure of the small pores, reducing the surface area [9-12]. Consequently, the capture capacity is reduced and a smaller fraction of CaO is converted due to slow diffusion in the $CaCO_3$ layer. Also, the initial decomposition rate decreases, causing a drop in the initial CO_2 concentration as observed in figure 2.5.

Variation of both temperature and H_2O concentration was studied on the same sample after aging via 40 adsorption-desorption cycles, as described above. The aging caused also a decrease in the CO_2 capture capacity, from 0.68 g_{CO2}/g_{CaO} (cycle 1) to 0.27 g_{CO2}/g_{CaO} (cycle 40), based on the amount of CO_2 desorbed. Every 5-10 cycles, an experiment at standard conditions (630°C in absence of water) was repeated to judge stability of the sample. Minor degradation is still observed after cycle 40 and the deviation in the standard experiment is used to correct the CO_2 concentrations obtained in experiments, varying H_2O concentrations and temperatures. The trend in aging during cycles 40 – 60 shows a linear decrease with 5% in the CO_2 concentration during those 20 cycles. On the other hand, after cycle 60 the sample partially recovered its capture capacity (from 0.24 to 0.58 g_{CO2}/g_{CaO}) causing an increase of 21% in the CO_2 concentration during decomposition. We suggest this is due to interaction of the sample with H_2O in ambient conditions for 5 weeks storage after cycle 60, in agreement with similar observations in literature reporting that steam can regenerate spent CaO after calcination [26-29]. Consequently, aging after cycle 61 is slightly stronger, with a linear decrease of 25% during 70 cycles.

Figure 2.6 shows a typical example of a CO_2 -absorption and -desorption experiment on a 5 mg sample $CaCO_3$ in the absence of water; this specific example is the 45th cycle. The absorption process is very fast and the amount of $CaCO_3$ formed cannot be determined accurately, because the time resolution of the MS is 2.5 s, which is not negligible compared to the typical time needed for saturation of 3 mg CaO, as shown in the inset of figure 2.6a. The amount of CO_2 desorbing can be calculated much more accurately based on the result in Figure 2.6b, resulting in 0.27 g_{CO2}/g_{CaO}. The result also confirms a constant desorption rate during typically 20 minutes in this case, as discussed above. This value is roughly a factor 2 smaller than the value measured on the large (80 mg) CaO sample in Figure 2.4, which is in order of magnitude in agreement with the aging effect observed in Figure 2.5, comparing cycle 45 with the first cycle.

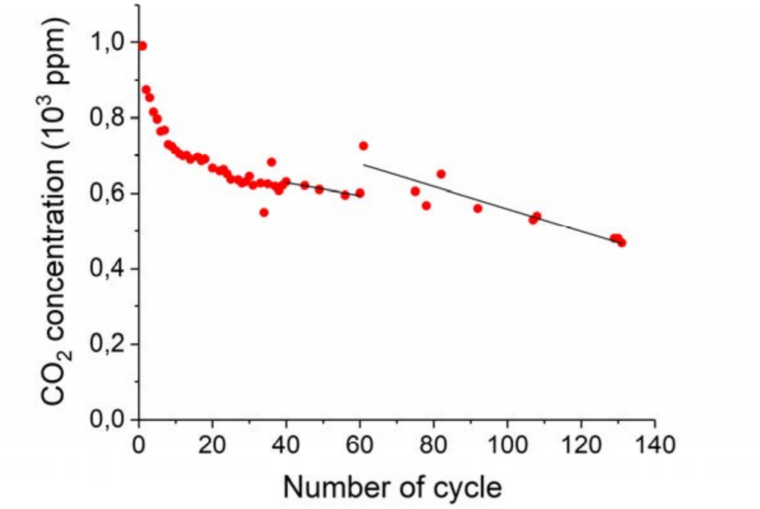

Figure 2.5: *CO_2 concentration at the first stage of decomposition of 5 mg $CaCO_3$ for different cumulative number of cycles. The decompositions are performed at standard conditions, i.e. 630°C in absence of H_2O in the gas mixture.*

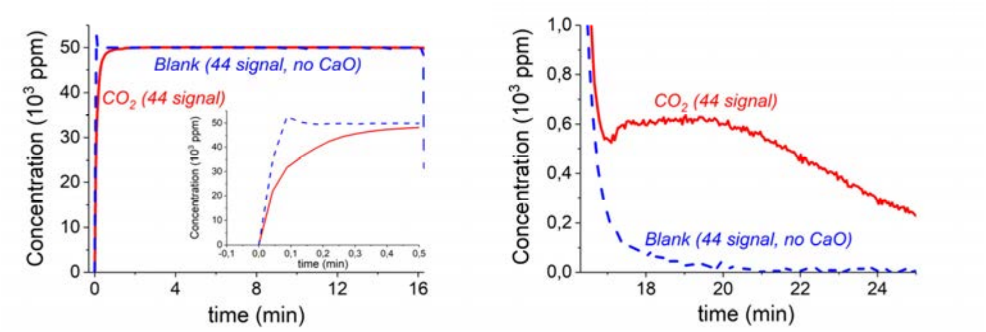

(a) **(b)**

Figure 2.6: *CO_2 concentration (solid line) monitored by Mass Spectrometry during CO_2 absorption **(a)** and desorption **(b)**; the dashed lines in both **(a)** and **(b)** present the blank experiments. The amount of CaO is 3 mg, temperature is 630°C, flow-rate is 90 ml min^{-1}. The absorption and desorption have been performed respectively in 5% CO_2 in Ar and in pure Ar.*

Figure 2.7 shows a typical result of a decomposition experiment of the aged, 3 mg carbonated sample in presence of steam (cycle 48). Compared with figure 2.6b, it is clear that H_2O enhances the decomposition, reducing the time needed for total CO_2 removal. Although CO_2 removal initiates at the same time when the Ar-H_2O mixture is introduced, a slower response of water is observed, which is an artefact caused by adsorption of water on the tubing in the equipment. This also explains that the CO_2 concentration first decreases, followed by an increase after about 30 seconds when water reached the reactor, enhancing $CaCO_3$ decomposition.

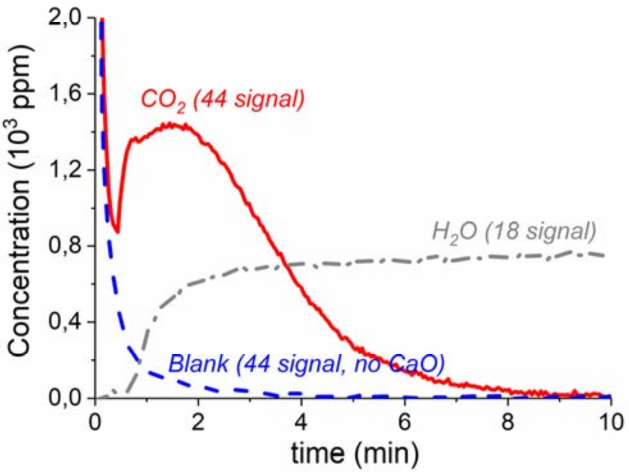

***Figure 2.7**: CO_2 (solid line) and H_2O (dash-dotted line) concentration monitored by Mass Spectrometry during CO_2 desorption in 0.075% H_2O in Ar; the dashed line presents the CO_2 concentration in a blank experiment. The amount of CaO is 3 mg, temperature is 630°C, flow-rate is 90 ml min^{-1}.*

2.3.3 Kinetic data

The experiment as presented in Figure 2.7 have been performed at temperatures between 590 and 650°C and with water concentrations varying between 0 and 1.25%. In all cases, the CO_2 concentration is far below the equilibrium concentration. The initial plateau value in the CO_2 concentration as observed in Figure 2.7 is used to calculate the rate of the decomposition reaction:

$$CaCO_3 \rightleftharpoons CaO + CO_2$$

$$R_{CO2} = C_{CO2} \cdot f_m = C_{CO2} \cdot \frac{f_v}{22400}$$

where R_{CO2} is the decomposition rate in mole CO_2 per second, C_{CO2} is the CO_2 concentration measured (fraction), f_m is the total molar gas flow in mol s^{-1} and f_v is the volumetric flow in ml s^{-1}.

Figure 2.8 presents the resulting data on the effect of H_2O partial pressure on the decomposition rate. Clearly, the decomposition rate is significantly influenced, even at low water concentration, approaching an asymptotic value when further increasing the water concentration. The inset in Figure 2.8 clarifies details at low water concentration. In some experiments, the CO_2 concentration will reach the plateau for a relatively short time (less than 2 minutes) due to rapid exhaustion. The results of these experiments are labelled with an asterisk indicating that the plateau is maintained shorter than 2 minutes, since this could lead to an underestimation of the reaction rate. Obviously, this is the case in experiments with relatively high decomposition rates. The error margin in the reaction rate is based on the reproducibility of the experiments. The experiments with a plateau shorter than 1 minute have been discarded. The error margin in the partial pressure is caused by minor water contamination (<5 ppm) in argon and inaccuracy in the flow rates when mixing argon and water saturated argon.

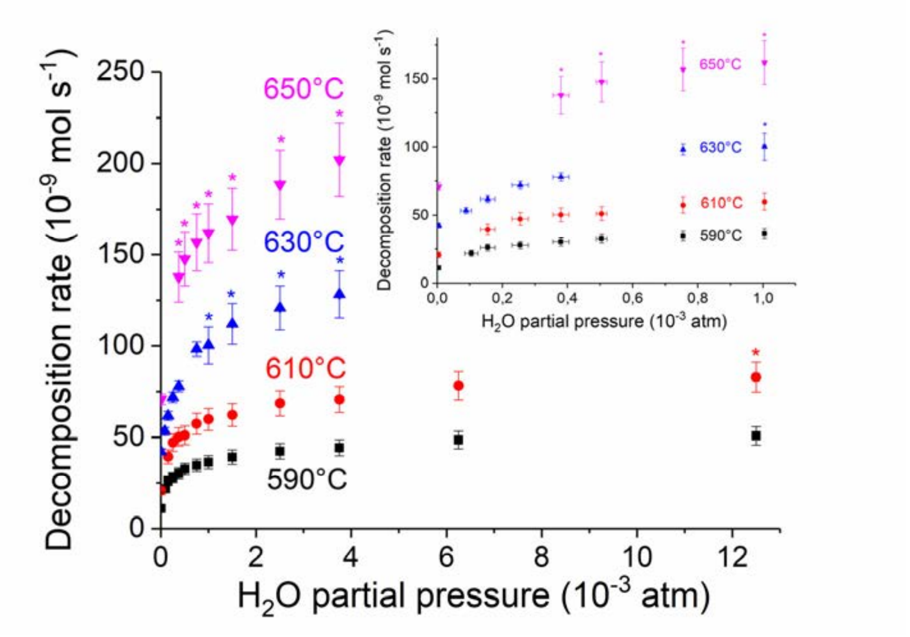

***Figure 2.8**: $CaCO_3$ decomposition rates at different temperatures and H_2O concentrations. The experiments with a narrow initial plateau, between 1 and 2 minutes, are labelled with an *.*

2.4 Discussion

It is clear from the result in Figure 2.8 that water enhances the decomposition of $CaCO_3$. We will first discuss the results of $CaCO_3$ decomposition in the absence of water and then discuss the effect of water.

2.4.1 *Decomposition kinetics of $CaCO_3$ without H_2O*

Figure 2.9 shows the Arrhenius plot of the decomposition rates obtained in argon atmosphere according the data in Figure 2.8. The experimental activation energy is 201 kJ mol^{-1} which is slightly higher than the ΔH of calcium-carbonate decomposition at 600°C, i.e. 171 kJ mol^{-1} [8]. This would indicate that the decomposition might be slightly activated.

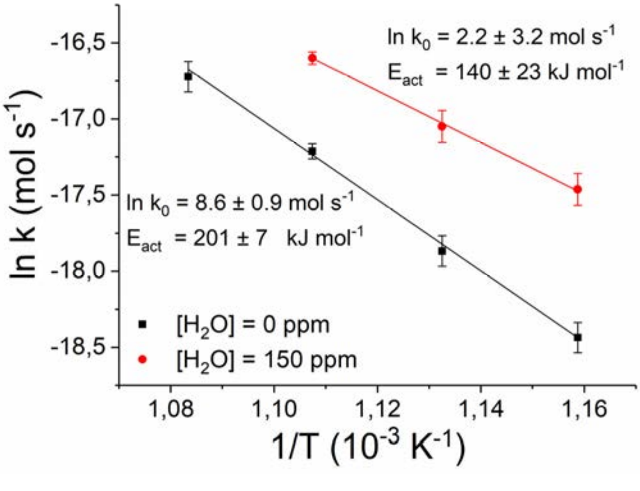

Figure 2.9: *Arrhenius plots for $CaCO_3$ decomposition in argon and 0.015% water in argon.*

$CaCO_3$ decomposition kinetics have been thoroughly investigated previously. Activation energies between 100 and 300 kJ mol^{-1} have been reported [19-23], agreeing reasonably with our result thanks to the large scatter in literature. The variation in the reported values is remarkably high, which is probably caused by re-absorption of CO_2

in the sample caused by mass transfer limitations as discussed by Beruto and Searcy [19, 22]. If re-absorption occurs and the equilibrium between calcium carbonate and calcium oxide is established locally in the sample, the apparent activation energy decreases approaching the ΔH value. Re-adsorption depends on the design of the reactor, the morphology of the sample as well as the experimental conditions. A plug flow reactor suffers less from re-adsorption effects [35] compared to samples in cups with stagnant gas-phase as used in TGA [36-38] and XRD experiments [32]. Gallagher [20] reported an activation energy of 205 kJ mol^{-1} after minimizing the re-absorption by diminishing the sample size, similarly to our finding 201 kJ mol^{-1}, indicating that re-absorption has no significant effect in this study.

2.4.2 Effect of water

The introduction of 0.015% of water reduces the activation barrier to 140±23 kJ mol^{-1}, as shown in Figure 2.9. This suggests that the presence of water opens a new reaction-pathway for calcium carbonate decomposition.

The effect of water on the decomposition rate is a catalytic effect, because no other products are formed. The gas phase contains exclusively CO_2 and presence of H_2, CH_4 and O_2 can be excluded based on MS results. Furthermore, formation of stable $Ca(OH)_2$ can be excluded as well, as no water desorption is detected when heating a sample to 950°C, after complete decomposition of $CaCO_3$ in the presence of water. This agrees with the fact that the H_2O partial pressures used are typically two orders of magnitude smaller than the H_2O equilibrium pressure at the experimental temperatures [8] and it is clear that no hydroxide is formed. Furthermore, the enhancing effect is more or less immediate as can be seen in Figure 2.7. In short, the reaction equation is not influenced, but the rate is, hence the effect of water is catalytic in nature.

Several groups observed an influence of water on $CaCO_3$ decomposition rate, but general agreement on the mechanism is still lacking. MacIntire et al. [39] and McIntosh et al. [40] proposed that the enhancement of the rate is caused by surface reaction with H_2O and by different growth of CaO crystals. Berger et al. and Li et al. [30, 33] ascribed it to improved heat transfer between gas and solid when H_2O is present. This argument was proposed also by Wang et al. [41], while Yin and Saulov [34] observed a maximum increase in decomposition rate for 2.2% H_2O, followed by a decrease at higher H_2O concentrations, explained by retardation of CO_2 diffusion in the gas phase in presence of moisture. Li et al. [33] also observed that the capture capacity of CaO is enhanced by steam during carbonation, explained by the fact that OH^- ions, formed via dissociative adsorption of H_2O, diffuse faster than O^{2-} ions in the growing $CaCO_3$ layer. Although we assume that OH is present also on $CaCO_3$ surface during decomposition, we rule out that enhancement of decomposition is caused by a similar effect on transport in the $CaCO_3$ layer, based on the fact that a steady decomposition rate is observed as shown in e.g. figure 2.6b, indicating that diffusion through the shrinking $CaCO_3$ is not rate determining. Only Wang and Thompson [32] gave a quantitative description of the catalytic effect, studying $CaCO_3$ decomposition in presence of H_2O with in-situ XRD at relatively low temperatures (400 – 480°C) and calculated activation energies of 197 kJ mol^{-1} in absence of water and 247 ± 17 kJ mol^{-1} at 0.2 bar of H_2O.

We exclude significant contributions of heat transfer and CO_2 diffusion, since enhancement is observed at very low H_2O concentrations. The activation barrier measured in presence of water (140 kJ mol^{-1}) is substantially different from the value reported by Wang (247 kJ mol^{-1}). This discrepancy might be due to the mild temperature used by Wang. In any case, catalysis is usually accompanied by a decrease in activation barriers, as observed in this study.

To better understand the mechanism of the catalytic effect of H_2O, we propose three assumptions:

A. The catalytic effect occurs via adsorption of H_2O according Langmuir adsorption isotherm.
B. The number of $CaCO_3$ surface sites at the surface is constant for all the experiments. This is in line with the correction for the variation in surface area during the measurements, as described earlier.
C. The diffusion of CO_3^{2-} ions in $CaCO_3$ is fast compared to the rate of decomposition, implying that the concentration of CaO sites on the surface is negligible. This assumption is supported by the fact that the decomposition rate is essentially constant till about 50% of the $CaCO_3$ is decomposed.

In addition to direct decomposition of $CaCO_3$ in absence of water (k_2), an alternative pathway involving water proceeds via an intermediate species formed by dissociative adsorption of water, namely $\mathrm{CaHCO_3 \cdot OH_s}$ (scheme 1), as suggested by Stipp based on an XPS study of H_2O adsorption on calcium carbonate at room temperature [42]. H_2O adsorption is assumed to be in equilibrium and the formation of $\mathrm{CaHCO_3 \cdot OH_s}$ can be described with equilibrium constant K_1. Hence the formation of $CaHCO_3 \cdot OH_s$ is much faster than the r.d.s., i.e. the decomposition of the intermediate (k_3).

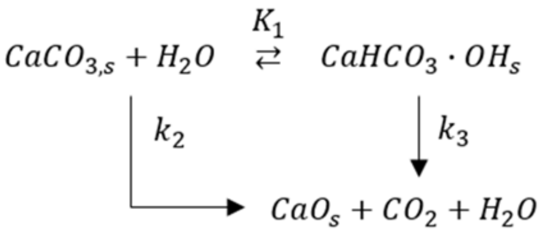

Scheme 2.1: *Proposed reaction scheme for $CaCO_3$ decomposition in presence of water vapour*

From now on the intermediate is labelled as I, while the concentrations (e.g. $[CaCO_3]$) represent densities of sites at the surface in moles $CaCO_3$ per square meter. Three reactions contribute:

Chapter 1	$CaCO_3 + H_2O \rightleftharpoons I$	$K_1 = \frac{[I]}{[CaCO_3] \cdot p_{H2O}}$
Chapter 2	$CaCO_3 \rightarrow CaO + CO_2$	$k_2 = k_{02} \cdot \exp(-\frac{E_{a2}}{RT})$
Chapter 3	$I \rightarrow CaO_s + CO_2 + H_2O$	$k_3 = k_{03} \cdot \exp(-\frac{E_{a3}}{RT})$

From assumption B, it follows that the number of reactive sites is constant. According to de Leeuw and Parker [43], the dominant surface of calcite is the {1014} which density of sites is

$$[CaCO_3]_0 \equiv [CaCO_3] + [I] = 8.1 \cdot 10^{-6}\ mols/m^2$$

Since reaction 1. is in equilibrium, we can derive the following equations:

$$K_1 = \frac{[I]}{\{[CaCO_3]_0 - [I]\} \cdot p_{H2O}}$$

Rearrangement results in a Langmuir adsorption equation:

$$\frac{[I]}{[CaCO_3]_0} \equiv \theta_I = \frac{K_1 \cdot p_{H2O}}{1 + K_1 \cdot p_{H2O}}$$

$$\frac{[CaCO_3]}{[CaCO_3]_0} = 1 - \theta_I = \frac{1}{1 + K_1 \cdot p_{H2O}}$$

Thus, the rate of $CaCO_3$ decomposition is equal to the sum of the rates of 2) and 3):

$$R_{CO2} = R_2 + R_3 = k_2 \cdot (1 - \theta_I) \cdot [CaCO_3]_0 + k_3 \cdot \theta_I \cdot [CaCO_3]_0$$

Rearrangement results in:

$$\frac{R_{CO2}}{[CaCO_3]_0} = \frac{k_2 + k_3 \cdot K_1 \cdot p_{H2O}}{1 + K_1 \cdot p_{H2O}} \tag{2.1}$$

Equation (2.1) has been used to fit the experimental data in figure 2.9 (R_{CO2}), obtaining values for K_1, k_2 and k_3 at different temperatures using MATLAB. The code is shown in detail in Appendix A2 and an example of fit is shown in Figure A2.2.

Temperature (°C)	**K_1 (bar^{-1})**	**k_2 (10^{-3} m^2 s^{-1})**	**k_3 (10^{-3} m^2 s^{-1})**
590	3420 ± 910	1.36 ± 0.14	6.05 ± 0.32
610	2750 ± 940	2.55 ± 0.25	10.1 ± 0.5
630	1790 ± 820	5.21 ± 0.21	18 ± 2.8
650	1260 ± 320	8.75 ± 0.35	30.8 ± 1.9

***Table 2.1**: Rate constants k_2 and k_3 as well as equilibrium constant K_1 obtained by data fitting with the proposed model*

Figure 2.10 shows the Arrhenius plot of the decomposition reaction of the intermediate (k_3) according the results presented in Table 1. The activation energy is 181±14 kJ mol^{-1}, slightly lower than the experimental activation barrier of 201±7 kJ mol^{-1} found in absence of water but it should be noted that the error margins do not allow a firm conclusion. Figure 2.11 presents the Van 't Hoff plot for step 1, i.e. the formation of I. Although the scattering is quite high, it can be concluded that K_1 decreases with temperature, indicating that ΔH is negative. Obviously, the value (-110±60 kJ mol^{-1}) is rather inaccurate but the adsorption is clearly exothermic, as would be expected for chemisorption. The ΔS can be estimated to be -66±60 J mol^{-1} K^{-1}; the scatter makes any firm conclusion impossible, but a slightly negative value would again be consistent with chemisorption of water.

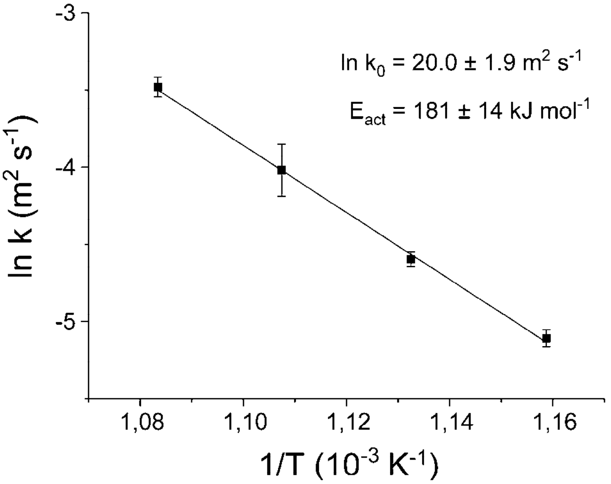

Figure 2.10: *Arrhenius plot for reaction 3, decomposition of the intermediate species.*

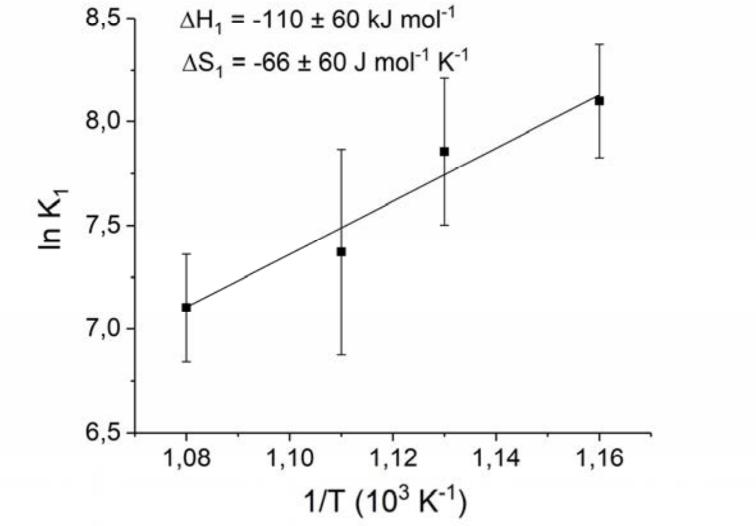

***Figure 2.11**: Van 't Hoff plot of for H_2O adsorption on $CaCO_3$.*

Figure 2.12 presents an energy diagram for the discussed scheme. An activation energy of 201 ± 7 kJ mol^{-1} has been calculated for the pathway without water (step 2), slightly larger than the ΔH value of 171 kJ mol^{-1}, based on thermodynamics [8], indicating that the reaction is slightly activated as discussed previously. Dissociative chemisorption of water (step 1) exhibits a ΔH value of -110±60 kJ mol^{-1}, implying that the formation of the intermediate species is favourable, despite the relatively large error margin. The decomposition of the intermediate (step 3) has an activation energy of 180 ± 14 kJ mol^{-1}. In figure 2.12 it is considered that step 3 is not only endothermic but might also be slightly activated. Even in case we assume that there is no additional activation barrier, considering also the maximal cumulative error margins in both ΔH_1, as well as in E_{act} of step 3, the energy level of the product of step 3 is between -5 kJ mol^{-1} and +14kJ mol^{-1}, defining the energy of the reactant as zero. It is clear that the energy gap of 281±60 kJ mol^{-1} between the intermediate and the final state cannot be bridged. In case decomposition of I would be also activated, the gap becomes even bigger. Therefore, we propose that the decomposition of the intermediate proceeds via a two-step process, i.e. via surface OH groups, as presented in the alternative scheme below:

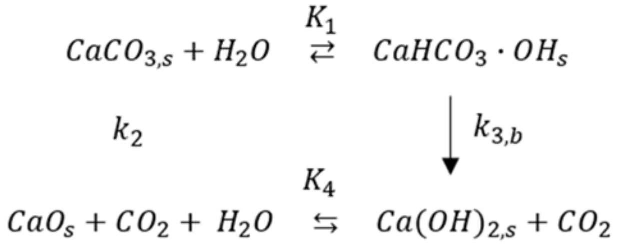

Scheme 2.2: *Reaction scheme for $CaCO_3$ decomposition in presence of water vapour, corrected for the formation of calcium hydroxide.*

The essential difference is that the intermediate decomposes to CO_2 and OH groups on the surface of CaO, whereas associative desorption of water is the fourth step closing the catalytic cycle. It should be noted that kinetics cannot be distinguish between the two models in scheme 1 and 2 as equilibrium 4 is at the side of CaO, CO_2 and water, implying that the surface concentration of surface OH groups is very low, as will be discussed further below.

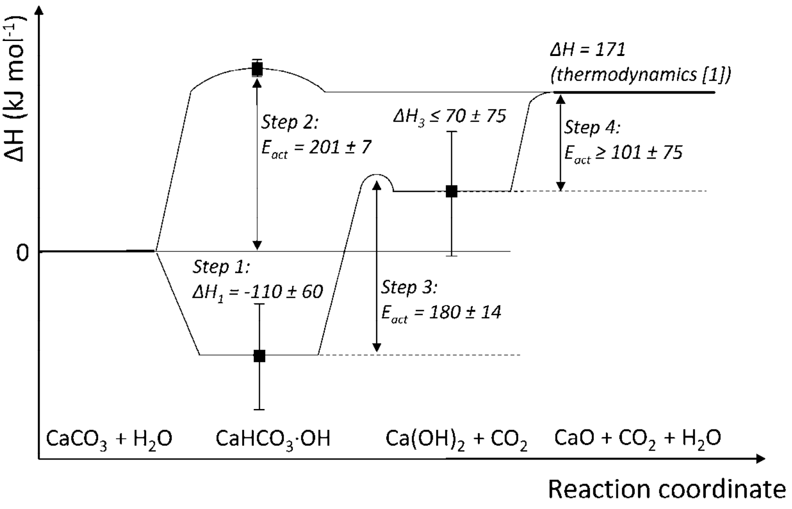

Figure 2.12*: Enthalpy scheme for direct decomposition (Step 2), decomposition via dissociative adsorption of water on $CaCO_3$ (steps 2 and 3, failing to close the energy gap), and via dissociative adsorption of water on $CaCO_3$ and surface OH (steps 2,3 and 4).*

Figure 2.12 illustrates that reaction 4 must account at least for 101 ± 75 kJ mol^{-1} according to the energy balance between the ΔH of reaction 1, the activation energy of reaction 3 and the ΔH calcium-carbonate decomposition according thermodynamics.

Remarkably, thermodynamics of decomposition of calcium hydroxide fits very well in this picture: the ΔH is 98 kJ mol^{-1} and ΔG is -10 kJ mol^{-1} at 600°C [8]. The increase in entropy of reaction 4 pushes the equilibrium towards the product calcium-oxide at such high temperature, resulting in a very low coverage of residual calcium hydroxide. It seems reasonable to use thermodynamic data of bulk $Ca(OH)_2$ despite the fact that surface OH groups are actually involved, because theoretical calculations of adsorption of water on CaO result in very similar numbers for ΔH. Carrasco et al. calculated an energy of -96 kJ mol^{-1} for the adsorption of a single H_2O molecule on a CaO cell at room temperature using an ab-initio method [44], while Manzano et al. [45] and Fujimori et al. [46] performed DFT analysis on adsorption of different numbers of H_2O molecules on CaO, reporting adsorption energies of respectively -112 ± 20 kJ mol^{-1} and -104 ± 6 kJ mol^{-1}. Also experimental values agree reasonably well: Fubini et al. [47] obtained a complete coverage of $Ca(OH)_2$ at 0.015 bar by dosing small amounts of H_2O on CaO at room temperature, calculating an adsorption energy of -140 ± 5 kJ mol^{-1}. It should be noted that in this case a multilayer is formed. Unfortunately, it was not possible to confirm the presence of bicarbonate and OH groups experimentally with in-situ IR spectroscopy because of the high temperature required.

2.5 Conclusions

The catalytic effect of water on calcium carbonate decomposition is demonstrated by measuring the decomposition rate at different temperatures and water concentrations. The experiments are designed to minimize any effects of mass transfer and re-adsorption of CO_2.The decomposition rate increases asymptotically, with a factor between 3 and 5 for typical H_2O concentrations of 0.5% or higher. The apparent activation energy substantially decreases from 201 to 140 kJ mol^{-1} with introduction of only 0.015% H_2O showing no further change when water content is increased.

Water provides access to an alternative pathway for $CaCO_3$ decomposition by dissociative chemisorption on the carbonate surface. The mechanism has been described with a simple kinetic scheme and rates constants, equilibrium constants and activation energies have been calculated. Chemisorption of water is exothermic with a ΔH of -110 kJ mol^{-1}. The decomposition of the intermediate species is a two-step process, probably via surface-OH, showing an activation energy of 181 kJ mol^{-1} for the decomposition to CO_2 and surface OH groups. Associative desorption of water is entropy driven and accounts for an additional enthalpy increase of 100 kJ mol^{-1}.

References

[1] NASA. Global Climate Change Vital Signs of the Planet **2018**.

https://climate.nasa.gov/

[2] United Nations Climate Change. The Paris Agreement **2015**.

https://unfccc.int/process-and-meetings/the-paris-agreement/the-paris-agreement

[3] International Energy Agency. World Energy Outlook **2017**.

https://www.iea.org/weo2017/

[4] E. J. Anthony. Carbon Capture and Storage and Carbon Capture, Utilization and Storage 2017. *Coal in the 21st century: energy needs, chemicals and environmental controls* **2017** 198-215.

[5] M. Bui, C. S. Adjiman, A. Bardow, E. J. Anthony, A. Boston, S. Brown, P. S. Fennell, S. Fuss, A. Galindo, L. A. Hackett, J. P. Hallett, H. J. Herzog, G. Jackson, J. Kemper, S. Krevor, G. C. Maitland, M. Matuszewski, I. S. Metcalfe, C. Petit, G. Puxty, J. Reimer, D. M. Reiner, E. S. Rubin, S. A. Scott, N. Shah, B. Smit, J. P. M. Trusler, P. Webley, J. Wilcox, and N. Mac Dowell. Carbon capture and storage (CCS): the way forward. *Energy Environm. Sci.* **2018**, 11, 1062-1176.

[6] D. Y. C. Leung, G. Caramanna, and M. M. Maroto-Valer. An overview of current status of carbon dioxide capture and storage technologies. *Renewable and Sustainable Energy Reviews* **2014**, 39, 426-443.

[7] J. Blamey, E.J. Anthony, J. Wang, and P.S. Fennell. The calcium looping cycle for large-scale CO_2 capture. *Progress in Energy and Combustion Science* **2010**, 36, 260-279.

[8] B. J. McBride, M. J. Zehe, and S. Gordon. NASA Glenn Coefficients for Calculating Thermodynamic Properties of Individual Species **2002**.

https://www.grc.nasa.gov/WWW/CEAWeb/TP-2002-21556.htm

[9] R. Barker. The reversibility of the reaction $CaCO_3 \rightleftharpoons CaO + CO_2$. *Journal of Chemical technology and Biotechnology* **1973**, 23, 733-742.

[10] R. H. Borgwardt. Sintering of nascent calcium oxide. *Chemical Engineering Science* **1989**, 44, 53-60.

[11] P.S. Fennell, R. Pacciani, J. S. Dennis, J. F. Davidson, and A. N. Hayhurst. The effects of repeated cycles of calcination and carbonation on a variety of different limestones, as measured in a hot fluidized bed of sand. *Energy & Fuels* **2007**, 21, 2072-2081.

[12] A. I. Lysikov, A. N. Salanov, and A. G. Okunev. Change of CO_2 carrying capacity of CaO in isothermal recarbonation-decomposition cycles. *Ind. Eng. Chem. Res.* **2007**, 46, 4633-4638.

[13] W. Liu, N. W. Low, B. Feng, G. Wang, and J.C. Diniz da Costa. Calcium precursors for the production of CaO sorbents for multicycle CO_2 capture. *Environ. Sci. Technol.* **2010**, 44, 841-847.

[14] C. Luo, Y. Zheng, N. Ding, Q. Wu, G. Bian, and C. Zheng. Development and performance of CaO/La_2O_3 sorbents during calcium looping cycles for CO_2 capture. *Ind. Eng. Chem. Res.* **2010**, 49, 11778-11784.

[15] M. Broda, and C. R. Müller. Synthesis of highly efficient, Ca-based, Al_2O_3-stabilized, carbon gel-templated CO_2 sorbents. *Adv. Mater.* **2012**, 24, 3059-3064.

[16] A. M. Kierzkowska, R. Pacciani, and C. R. Müller. CaO-based CO_2 sorbents: from fundamentals to the development of new, highly effective materials. *ChemSusChem* **2013**, 6, 1130-1148.

[17] X. Ma, Y. Li, L. Duan, E. J. Anthony, and H. Liu. CO_2 capture performance of calcium-based synthetic sorbent with hollow core-shell structure under calcium looping conditions. *Applied Energy* **2018**, 225, 402-412.

[18] J. Chen, L. Duan, F. Donat, C. R. Müller, E. J. Anthony, and M. Fan. Self-activated, nanostructured composite for improved CaL-CLC technology. *Chemical Engineering Journal* **2018**, 351, 1038-1046.

[19] D. Beruto, and A. Searcy. Use of the Langmuir Method for Kinetic Studies of Decomposition Reactions: Calcite ($CaCO_3$). *J. Chem. Soc., Faraday Trans.* **1974**, 1, 70, 2145-2153.

[20] P. K. Gallagher, and D. W Johnson. The effects of sample size and heating rate on the kinetics of the thermal decomposition of $CaCO_3$. *Thermochimica Acta* **1973**, 6, 67-83.

[21] A. L. Draper, and L. K. Sveum. The Analysis of thermal data. *Thermochimica Acta* **1970**, 1, 345-365.

[22] D.T. Beruto, A. W. Searcy, and M. G. Kim. Microstructure, kinetic, structure, thermodynamic analysis for calcite decomposition: free-surface and powder bed experiments. *Thermochimica Acta* **2004**, 424, 99-109.

[23] M. Maciejewsky, and A. Reller. How (un)reliable are kinetic data of reversible solid-state decomposition processes? *Thermochimica Acta* **1987**, 110, 145-152.

[24] T. Darroudi, and A. W. Searcy. Effect of CO_2 pressure on the rate of decomposition of calcite. *J. Phys. Chem.* **1981**, 85, 3971-3974.

[25] R. H. Borgwardt. Calcium oxide sintering in atmospheres containing water and carbon dioxide. *Ind. Eng. Chem. Res.* **1989**, 28, 493-500.

[26] F. Donat, N. H. Florin, E. J. Anthony, and P. S. Fennell. Influence of high-temperature steam on the reactivity of CaO sorbent for CO_2 capture. *Environ. Sci. Technol.* **2012**, 46, 1262-1269.

[27] S. Champagne, D. Y. Lu, A. Macchi, R. T. Symonds, and E. J. Anthony. Influence of steam during injection during calcination on the reactivity of CaO-based sorbent for carbon capture. *Ind. Eng. Chem. Res.* **2013**, 52, 2241-2246.

[28] Y. Wu, J. Blamey, E. J. Anthony, and P. S. Fennell. Morphological Changes of Limestone Sorbent Particles during Carbonation/Calcination Looping Cycles in a Thermogravimetric Analyzer (TGA) and Reactivation with Steam. *Energy Fuels* **2010**, 24, 2768-2776.

[29] M. Kavosh, K. Patchigolla, E. J. Anthony, and J. E. Oakey. Carbonation performance of lime for cyclic CO_2 capture following limestone calcination in steam/CO_2 atmosphere. *Applied Energy* **2014**, 131, 499-507.

[30] E.E. Berger. Effect of steam on the decomposition of limestone. *Industrial and Engineering Chemistry* **1927**, 19, 594-596.

[31] Y.H. Khraisha, and D.R. Dugwell. Effect of water-vapor on the calcination of limestone and raw meal in a suspension reactor. *Chemical Engineering Research and Design* **1991**, 69, 76–78.

[32] Y. Wang, and W. J. Thomson. The effects of steam and carbon dioxide on calcite decomposition using Dynamic X-Ray Diffraction. *Chemical Engineering Science* **1995**, 50, 9, 1373-1382.

[33] Z. H. Li, Y. Wang, K. Xu, J. Z. Yang, S. B. Niu, and H. Yao. Effect of steam on CaO regeneration, carbonation and hydration reactions for CO_2 capture. *Fuel Processing Technology* **2016**, 151, 101-106.

[34] J. Yin, X. Kang, C. Qin, B. Feng, A. Veeraragavan, and D. Saulov. Modeling of $CaCO_3$ decomposition under CO_2/H_2O atmosphere in calcium looping processes. *Fuel Processing Technology* **2014**, 125, 125-138.

[35] R. H. Borgwardt. Calcination kinetics and surface area of dispersed limestone particles. *AlChE Journal* **1985**, 31, 103-111.

[36] T. R. Rao. Kinetics of calcium carbonate decomposition. *Chem. Eng. Technol.* **1996**, 19, 373-377.

[37] F. Garcia-Labiano, A. Abad, L. F. de Diego, P. Gayan, and J. Adanez. Calcination of calcium-based sorbents at pressure in a broad range of CO_2 concentrations. *Chemical Engineering Science* **2002**, 57, 2381-2393.

[38] J. Yin, C. Qin, B. Feng, L. Ge, C. Luo, W. Liu, and H. An. Calcium looping for CO_2 capture at a constant high temperature. *Energy & Fuels* **2014**, 28, 307-318.

[39] W.H. MacIntire, and T.B. Stansel. Steam catalysis in calcinations of dolomite and limestone fines. *Industrial and Engineering Chemistry* **1953**, 45, 1548-1555.

[40] R.M. McIntosh, J.H. Sharp, and F.W. Wilburn. The thermal decomposition of dolomite. *Thermochimica Acta* **1990**, 165, 281-296.

[41] Y. Wang, S. Lin, and Y. Suzuki. Limestone calcination with CO_2 capture (II): decomposition in CO_2/steam and CO_2/N_2 atmosphere. *Energy & Fuels* **2008**, 22, 2326-2331.

[42] S.L.S. Stipp. Where the bulk terminates: Experimental evidence for restructuring, chemibonded OH – and H +, adsorbed water and hydrocarbons on calcite surfaces. *Molecular Simulations* **2002**, 28, 6-7, 497-516.

[43] N.H. de Leeuw, and S.C. Parker. Surface structure and morphology of calcium carbonate polymorphs calcite, aragonite, and vaterite: an atomistic approach. *J. Phys. Chem. B* **1998**, 102, 2914-2922.

[44] J. Carrasco, F. Illas, and N. Lopez. Dynamic ion pairs in the adsorption of isolated water molecules on alkaline-earth oxide (001) surfaces. *Physical Review Letters* **2008**, 100, 016101, 1-4.

[45] H. Manzano, R. J. M. Pellenq, F. Ulm, M. J. Buehler, and A. C. T. van Duin. Hydration of calcium oxide surface predicted by Reactive Force Field Molecular Dynamics. *Langmuir* **2012**, 28, 4187-4197.

[46] Y. Fujimori, X. Zhao, X. Shao, S. V. Levchenko, N. Nilius, M. Sterrer, and H. Freund. Interaction of water with the CaO(001) surface. *J. Phys. Chem. C* **2016**, 120, 5565-5576.

[47] B. Fubini, V. Bolis, M. Bailes, and F. S. Stone. The reactivity of oxides with water vapor. *Solid State Ionics* **1989**, 32/33, 258-272.

Chapter 3

Plasma Catalysis: Distinguishing between Thermal and Chemical Effects

Summary

The goal of Chapter 3 is to develop a method to distinguish between plasma chemistry and thermal effects in a Dielectric Barrier Discharge non-equilibrium plasma containing a packed bed of porous particles. Decomposition of $CaCO_3$ in Ar plasma is used as a model reaction and $CaCO_3$ samples were prepared with different external surface area, via the particle size, as well as with different internal surface area, via pore morphology. Also, the effect of the CO_2 in gas phase on the formation of products during plasma enhanced decomposition is measured. The internal surface area is not exposed to plasma and relates to thermal effect only, whereas both plasma and thermal effects occur at the external surface area. Decomposition rates were in our case found to be influenced by internal surface changes only and thermal decomposition is concluded to dominate. This is further supported by the slow response in the CO_2 concentration at a timescale of typically 1 minute upon changes in discharge power. The thermal effect is estimated based on the kinetics of the $CaCO_3$ decomposition, resulting in a temperature increase within 80 °C for plasma power from 0 to 6 W. In contrast, CO_2 dissociation to CO and O_2 is controlled by plasma chemistry as this reaction is thermodynamically impossible without plasma, in agreement with fast response within a few seconds of the CO concentration when changing plasma power. CO forms exclusively via consecutive dissociation of CO_2 in the gas phase and not directly from $CaCO_3$. In Chapter 5, this methodology is used to distinguish between thermal effects and plasma–chemical effects in more reactive plasma, containing, e.g., H_2.

3.1 Introduction

Plasma catalysis is receiving more and more attention in the last few years, since the specific interactions between plasma and catalyst surface may lead to synergistic effects [1–4]. One of the earliest plasma catalytic applications is the abatement of volatile organic compounds (VOC) [5,6], while in the last decade research has been focused more on CO_2 conversion [7–9], conversion of hydrocarbons via reforming, and coupling [10–12], as well as activation of N_2 [13,14]. Reforming of hydrocarbons is an example of an endothermic reaction, where plasma catalysis holds promise because of activation of hydrocarbons at low temperature, but also because electrical energy would be used to generate the required heat. Methane coupling and CO_2 dissociation are examples of thermodynamically hill-up reactions, which are clearly more challenging.

Non-equilibrium plasma, e.g., microwave of Dielectric Barrier Discharge (DBD) plasma, is especially attractive because it operates at relatively low temperatures [15–17]. Consequently, catalyst sintering is prevented. Moreover, low temperatures are a necessity to enable catalysis in the first place, facilitating initial adsorption that decreases entropy. Starting and stopping plasma reactors is much faster than usual thermal reactors, which is an advantage when fast capacity changes are required, e.g., in connection with intermittent energy supply and storage.

DBD plasma is frequently used for studying plasma catalytic conversion. The high AC voltages applied at relatively low frequency (50 to 10^5 Hz) produces a non-equilibrium plasma with very high electron temperatures (1–10 eV equal to 10^4–10^5 K), high vibrational temperatures (10^3 K), and rather low rotational and translational temperatures in the plasma zone, typically in the order or smaller than 100 K [6,15–17]. The fact that energy would be directed directly to bond breaking, without the need to heat up the gas mixture completely, is very attractive as heat exchangers to recover the heat would become redundant. The presence of a dielectric between the two electrodes prevents the formation of hot plasma in a single spark, forming instead several microfilaments, resulting in a more uniform plasma. The low gas temperature allows the application of a catalyst directly in the plasma generation zone without fast deactivation, maximizing the interaction between active species and the catalytic phase. Furthermore, DBD plasma can be generated at atmospheric pressure, which is interesting from the application point of view. Very promising results were presented in the last years on several topics, such as CO_2 conversion [9,18–27] and CH_4 reforming [12,13,28–34], in terms of high conversion and selectivity. However, the main issue of DBD remains the low energy efficiency achieved, i.e., the ratio between chemical energy stored in the produced molecules and electrical energy applied, which rarely surpasses 10%. This is explained by dissociative excitation by electron impact, involving a large activation barrier, dominating over vibrational excitation [7,35–37]. A more suitable technique for vibrational excitation is microwave plasma, which uses GHz frequencies [38–40]. However, the temperature increase is more pronounced in microwave plasma, limiting the opportunities for plasma catalysis.

Interaction between plasma and catalyst can proceed in many ways [1–4]. Obviously, the plasma will introduce new chemical species including activated species, radicals, and ions, which may all adsorb on the catalyst opening new reaction pathways and influencing the products distribution. Plasma can also induce photocatalytic effects by UV irradiation, impingement of charged particles and thermal fluctuations. The surface and subsurface of a catalyst can be modified by plasma via poisoning, implantation, sputtering, and etching. The presence of a catalyst influences the plasma by changing the electrical field distribution, but also modifying the free volume and the residence time in the plasma zone. Plasma also affects the temperature of the system, obviously influencing reaction rates of chemical reactions.

Unfortunately, it is not possible to measure the temperature in a DBD plasma catalytic reactor directly. Application of a thermocouple inside the plasma is not possible due to the high electric fields present. Nevertheless, thermocouples were used a few millimetres outside the plasma zone inside the reactor tube, or outside the reactor tube just alongside the plasma zone [41–44]. Furthermore, many attempts have been done to measure temperatures indirectly, for instance by emission spectroscopy of UV–Vis radiation probing electronic transitions in nitrogen and hydroxyl groups [45–48], by UV absorption spectroscopy [47], or by infrared emission [23,44]. Unfortunately, these methods have serious limitation depending on the reactor material properties as well as the packed bed properties.

Chapter 3 proposes a method to distinguish between thermal effect and plasma chemistry effects in fixed bed DBD plasma reactors. The decomposition of calcium carbonate is used as a model system for packed beds containing porous particles. It is well known that thermal decomposition results in the formation of exclusively CaO and CO_2 [49], whereas formation of CO would indicate that plasma chemistry is involved. A pure thermal effect is likely when using an Ar plasma, since no chemistry is expected between activated argon species and $CaCO_3$. The choice for $CaCO_3$ as model system in combination with a DBD reactor is inspired by its relevance for CO_2 separation. The calcium looping cycle consists of carbonation of CaO for capturing followed by calcination of $CaCO_3$ in order to recycle calcium oxide and to produce pure CO_2 [49]. Bottleneck is the calcination reaction that requires high temperatures in order to achieve high CO_2 concentrations in the outlet, i.e., at least 950 °C to achieve 1 bar CO_2 [50]. Such temperatures result in sintering, decreasing the CO_2 capture capacity when calcium oxide is recycled multiple times [51–53]. Using a DBD plasma during the calcium carbonate decomposition might circumvent the need for such high temperatures, and in addition CO_2 will be converted by plasma into CO, converting electrical energy into chemical energy and producing an added-value product.

The method to distinguish between thermal and plasma chemistry is based on the fact that plasma cannot exist in the pores inside particles if they are smaller than a few micrometres, as can be understood from Paschen's Law, which is generally accepted [54,55]. It was recently reported in a theoretical study that penetration of plasma in pores is possible to some extent [56]; however, we will discuss that under our conditions the plasma is limited to the interparticle volume and the external surface area is exposed under the conditions applied. The internal surface area, caused by the presence of small pores in the material is not exposed to the plasma, but would be influenced by any thermal effect. The theory is explained in detail in the section Methods in Appendix A3 and shown in Figure A3.1. The method then consists of two approaches: first, the effects of both the internal surface area as well as external surface area will be explored, and second, the dynamics of the performance on changing plasma power will be evaluated. Decomposition rate and eventual further reactions of the carbon dioxide product will be assessed. Argon plasma is used as a reference for the method to be developed as to distinguish between thermal effects and plasma–chemical effects.

3.2 Materials and methods

3.2.1 Plasma reactor

Figure 3.1 shows a schematic representation of the equipment used to measure plasma enhanced decomposition of $CaCO_3$. The fixed bed reactor is fed with either pure Ar, or a mixture of Ar containing 5% CO_2. The temperature of the oven is controlled with a Eurotherm controller with an accuracy of ± 0.5 °C between room temperature and 1000 °C. The isothermal zone is 8 cm long at 900 °C, defined as the part of the reactor with less than ±1 °C temperature variation. A Quadrupole Mass Spectrometer (MS) measures the composition of the gas downstream of the reactor. The MS signals for CO_2 (44 m/e) and CO (28 m/e) are calibrated between 0.16% and 5%, resulting in a linear relationship. The reactor is a 4 mm inner- and 6 mm outer diameter quartz tube. The inner electrode is a stainless-steel rod of 1 mm diameter placed coaxially in the centre of the reactor section. The outer electrode is a 1 cm long stainless-steel tube with 6 mm inner diameter, enclosing a plasma zone of 0.035 cm^3 in volume. The amount of $CaCO_3$ sample was limited to 10.5 ± 0.3 mg in order to prevent CO_2 concentrations approaching thermodynamic equilibrium, thus minimizing reabsorption of CO_2. The 10 mg sample was mixed with 90 mg α-Al_2O_3, filling the plasma zone completely and preventing any bypassing. An AC voltage of up to 10 kV peak to peak was applied to the inner electrode with a frequency of 23.5 kHz using a PMV 500–4000 power supply, while the outer electrode is connected to the ground via a probe capacitor of capacity 4 nF. The power of the plasma was calculated using the Lissajous method by measuring the voltage on the inner electrode with a Tektronix P6015A high voltage probe and on the outer electrode with a TT–HV 250 voltage probe, as described in the literature [57]. A sample of Lissajous plot is shown in Figure A3.2 in appendix A3.

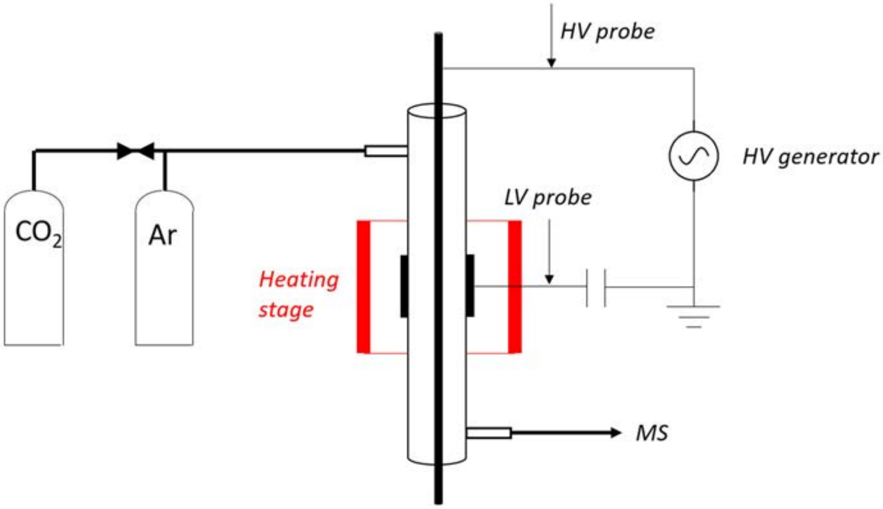

Figure 3.1: Schematic of the setup to study decomposition of $CaCO_3$ in Ar plasma. The generator can provide up to 30 kV peak to peak with a frequency range of 23.5 to 66 kHz. The plasma zone is 1 cm long and the reactor is a quartz tube with 6mm outer diameter and 4mm inner diameter. The inner electrode is a stainless-steel rod of 1mm diameter.

3.2.2 Calcium oxides preparation

Three different precursors have been used to synthesize calcium oxide, respectively (batch I) calcium L-ascorbate-di-hydrate (99%, Sigma-Aldrich, St. Louis, MO, USA), (batch II) calcium D-gluconate-monohydrate (99%, Alfa Aesar, Haverhill, MA, USA), and (batch III) calcium carbonate (99%, Sigma-Aldrich, St. Louis, MO, USA). The precursors were calcined in 20% O_2 in N_2 at atmospheric pressure, heating the sample to 900 °C (heating rate 15 ^{o}C/min), and keeping the temperature at 900 °C for 3 h. The calcined products were pelletized (pressure 160 bar), crushed and sieved in different particle size range: 250–300 µm, 100–125 µm, and 38–45 µm.

3.2.3 Carbonation

Five $CaCO_3$ samples have been produced via carbonation of CaO. The oxide synthesized from calcium ascorbate (batch II) has been treated in situ with 5% CO_2 in Ar at 630 °C for 4 h (heating rate 15 °C/min), the other two batches I and III were treated in a calcination oven with 20% CO_2 in N_2 at 630 °C for 5 h (heating rate 15 °C/min). The oxide synthesized from calcium carbonate (III) was consecutively sintered in pure CO_2 at 900 °C for 24 h (heating rate 15 °C/min), as summarized in Table 3.1. The resulting three samples (A, B, and C) were crushed and sieved, obtaining particles sizes in the range between 250 and 300 µm. The material made from $CaCO_3$ was also obtained with smaller particles, between 100 and 125 µm (sample D) and between 38 and 45 µm (sample E), respectively.

3.2.4 Characterization

The specific surface area, pore volume, and pore size distribution of the samples were measured both in CaO form as well as in $CaCO_3$ form, after carbonation. The samples were first degassed at 300 °C in vacuum for 3 h. The surface area was calculated based on the BET isotherm for N_2 adsorption at −196 °C in a Tristar 3000 analyser (Micromeritics, Norcross, GA, USA). The pore size distribution was measured by Hg porosimetry. The chemical composition was determined with X-ray fluorescence analysis in a S8 Tiger (Bruker, Billerica, MA, USA).

3.2.5 Experimental procedure

The carbonated samples (ex situ) were heated up in 5% CO_2 in Ar to the temperature at which decomposition is to be measured, in order to prevent any premature decomposition. The decomposition reaction is initiated by switching the gas composition from 5% CO_2 to pure Ar, at a constant flow rate of 30 mL/min. Isothermal decomposition experiments have been performed at different plasma powers by varying the applied voltage. The plasma power was varied during the experiment in case of low decomposition rates, allowing observations of steady state CO_2 concentrations for each plasma power. In case $CaCO_3$ is exhausted too fast, only one single power was applied. The rate of decomposition is calculated based on the sum of CO_2 and CO concentrations in the exit of the reactor as measured with MS.

Sample C (Table 3.1, ex calcium carbonate, 250–300 µm) was measured by performing 20 carbonation-decomposition cycles. The sample was re-carbonated, after a decomposition experiment, in the reactor (in situ) by CO_2 absorption at 630 °C in 5% CO_2 in Ar for 30 min in a constant flow of 90 mL/min. The carbonated samples were decomposed using a constant power plasma in the presence of a relatively low CO_2 concentration in the feed, varied between 0 to 3200 ppm. During these 20 cycles, blank experiments were done every few cycles by decomposing in the absence of plasma, in order to ensure that the sample did not change in the course of the experiments.

Blank experiments were performed with 100mg of α-Al_2O_3 with particles size of 250 to 300 µm in the absence of any $CaCO_3$, operating with low CO_2 concentrations in the feed, i.e., 1000, 2000, and 3200 ppm. The plasma power was varied between 0 and 10 W and the responses of the CO and CO_2 concentrations were measured with MS.

3.3 Results

X-ray fluorescence (XRF) measurements confirmed the purity of CaO (99.12%) containing some minor impurities, i.e., SiO_2 (0.16%), MgO (0.12%), and Al_2O_3 (0.095%).

Table 3.1 in the Materials and Methods Section presents the surface area and particles sizes of the five prepared samples. The surface areas reported for samples A and B are well reproducible, but it should be noted that systematic errors may be larger, given the relatively low value of the surface areas. The surface area of batch III (samples C–E) is below the detection limit of the N_2 physisorption equipment, from which we deduce that the surface area is below 0.5 m^2/g. In any case, the total surface of the samples increases in the order C<B<A. Remarkably, the surface areas of the parent oxides are much higher, confirming the theory that formation of a carbonate layer induces closure of small pores, due to the lower density of $CaCO_3$ (2.71 g cm^{-3}) compared to CaO (3.35 g cm^{-3}). However, the order in surface area remains the same, reassuring that the surface area of the samples is in the order A>B>C=D=E. Figure 3.2 shows the pore size distribution measured with mercury porosimetry for the carbonated samples synthesized from calcium ascorbate (sample B, Figure 3.2a) and from calcium carbonate (sample C, Figure 3.2b). Sintering at 900°C for 24 h (sample C) causes formation of large pores of typically 400 nm, compared to sample A which was treated with CO_2 only at 630°C. Remarkably, the pore volume of the sintered sample is ca. 20%, much larger than sample B (ca. 5%), indicating that smaller pores collapsed favouring enlargement of the bigger pores.

Code	**Precursor (Batch #)**	**Carbonation Time (h)**	**Sintering Time (h)**	**CaO S.S.A. ($m^2\ g^{-1}$)**	**$CaCO_3$ S.S.A. ($m^2\ g^{-1}$)**	**Diameter (μm)**
A	Ca Gluc. (I)	5	0	46	1.7 ± 0.1	250–300
B	Ca Asc. (II)	4	0	23	0.8 ± 0.1	250–300
C	$CaCO_3$ (III)	5	24	10	<0.5	250–300
D	$CaCO_3$ (III)	5	24	10	<0.5	100–125
E	$CaCO_3$ (III)	5	24	10	<0.5	38–45

Table 3.1: *Characteristics of the samples prepared from three different precursors.*

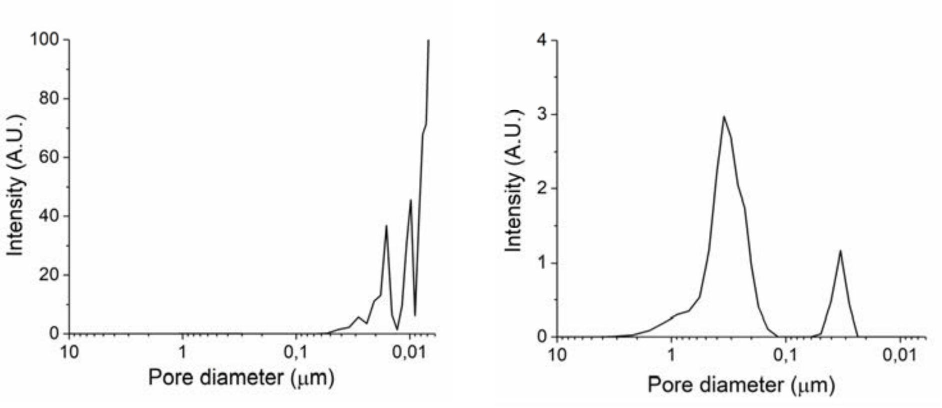

(a) **(b)**

***Figure 3.2**: **(a)** Pore size distribution for sample B batch II and **(b)** pore size distribution for sample C batch III according Hg porosimetry.*

Figure 3.3 presents the results of isothermal decomposition at 630 °C of the carbonated samples A–C, showing that the CO_2 concentration generated via decomposition is within 10% constant during typically 20 min, after an induction time of a few minutes. In general, this is observed when decomposition is limited to max 50% of $CaCO_3$ present initially. The amounts of CO_2 desorbed from the samples A, B, and C are 4, 3.8, and 2.8 mg, respectively, equivalent with 0.66, 0.61, and 0.39 g_{CO2}/g_{CaO}, respectively. The amounts of CO_2 decrease in the same order as surface area. It can be estimated that the thickness of the $CaCO_3$ layer is in the order of 30 nm for all three sample. This is consistent with the observation that the maximum CO_2 concentration during decomposition experiments, between 900 to 1700 ppm, which is significantly lower than the 7000 ppm thermodynamic equilibrium CO_2 concentration at 630 °C [50]. Consequently, the CO_2 concentration is determined by kinetics, instead of thermodynamics, and thus also by the surface area.

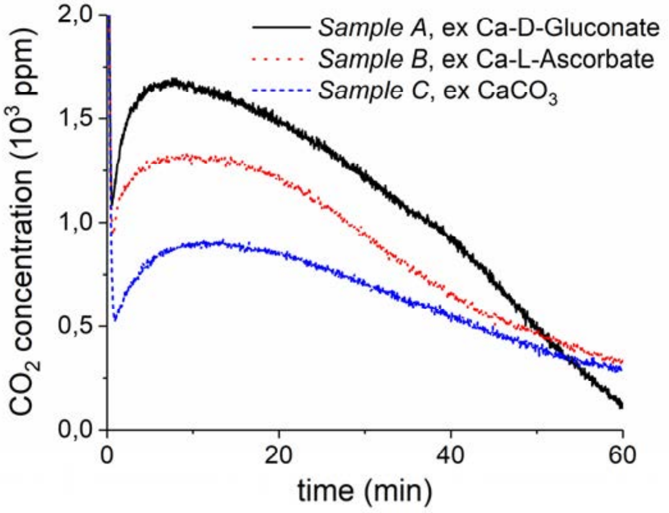

Figure 3.3: *CO_2 concentration monitored by mass spectrometry during decomposition of carbonated sample A (solid line), sample B (dotted line), and sample C (dashed line). The temperature is 630 °C, flow rate is 30 mL min^{-1}, and the gas is pure Ar.*

Figure 3.4 presents the effect of plasma power on the decomposition of carbonated sample C. No plasma was applied during the first two minutes and CO_2 is the only product observed, while in the presence of plasma CO and O_2 are also produced, next to CO_2. Every two minutes a different voltage is applied, and the power is measured after ca. 1 minute. Changing the plasma power causes a fast response of the CO concentration in the order of seconds, while the CO_2 concentration needs typically a minute to stabilize. The O_2 concentration shows a delay; this effect is not understood at this time, but it may be speculated that interaction with CaO is responsible. Figure 3.4 shows that steady-state decomposition was achieved for the two lower plasma power values. The highest power setting of 9.6 W caused exhaustion so that the product concentrations are likely to be underestimated. Additional experiments were performed at constant maximum power as shown in Figure 3.5. Two experiments were performed at 2.1 W and demonstrate a reproducibility within ±5%, even though plasma was applied with a 1.5 min delay in the second experiment (Figure 3.5b). Figure 3.5c is performed at 4.4 W, showing a higher decomposition rate and shorter steady state duration. Therefore, the power was not further increased for this sample and in general the maximum power was limited to 5.1 W.

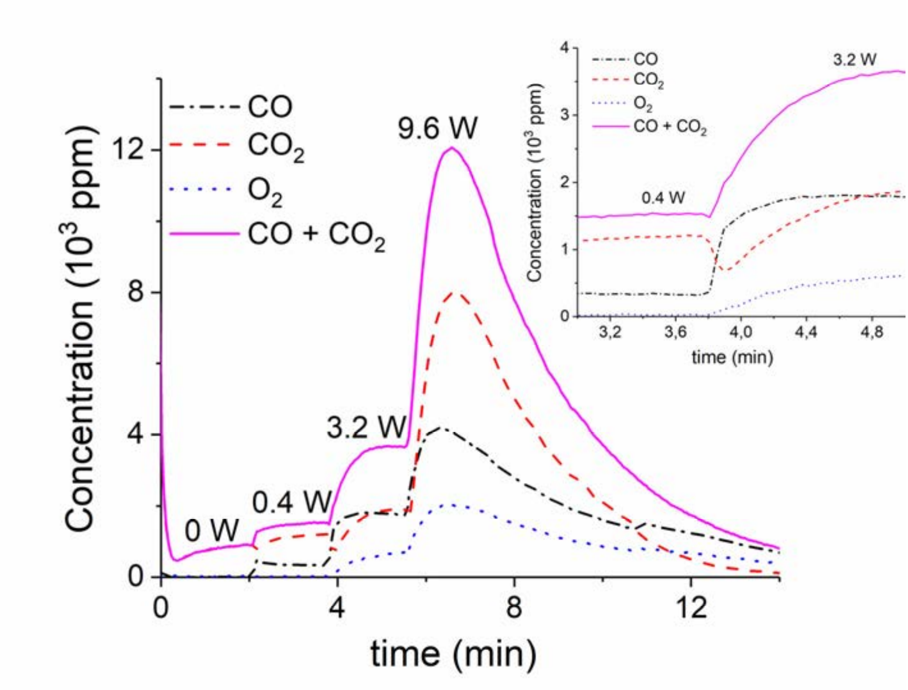

__Figure 3.4:__ Concentration of the products of $CaCO_3$ decomposition (sample C) as function of time at 630 °C in pure argon, flow rate of 30 mL/min, plasma power is changed every 2 min with values of 0, 0.4, 3.2, and 9.6 W.

Figure 3.6 shows three typical results on the effect of the specific surface area on the decomposition at 2.1 W plasma power, by comparing the samples A (ex-calcium gluconate, Figure 3.6a), B (ex-calcium ascorbate, Figure 3.6b), and C (ex-calcium carbonate Figure 3.6c), keeping particle size constant (250–300 μm). The total decomposition rate, as calculated based on the sum of the rates of formation of CO and CO_2, seems to increase with increasing specific surface area, as also observed in the absence of plasma. During the decomposition of sample B, the power has been turned off after 9 min, resulting in a rapid decrease in the CO and CO + CO_2 concentrations. Figure 3.7 presents all data on the decomposition rate measured on the three samples when changing the plasma power, showing that the rate of decomposition at the same power is significantly lower for the sample with the lowest specific surface area. The difference between sample A and B is not larger than experimental scatter, although the data suggest a slightly higher rate for sample A.

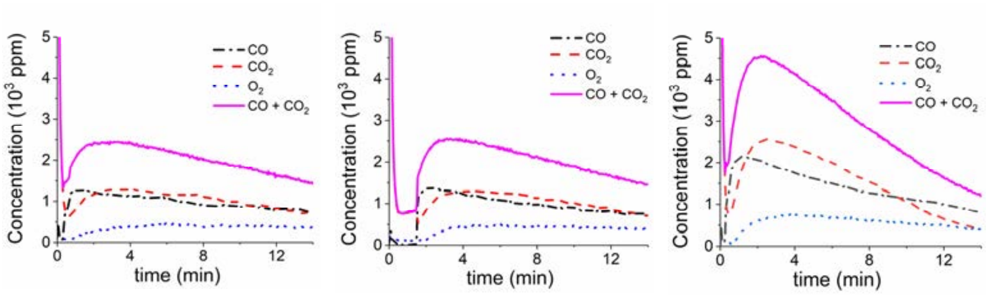

(a) (b) (c)

***Figure 3.5**: Concentration of the products of $CaCO_3$ decomposition (sample C) as function of time at 630 °C in pure argon, flow rate of 30 mL min^{-1}, plasma power is 2.1 W **(a,b)** and 4.4 W **(c)**. Plasma is turned on at the beginning of decomposition **(a,c)** or after 1.5 min **(b)**.*

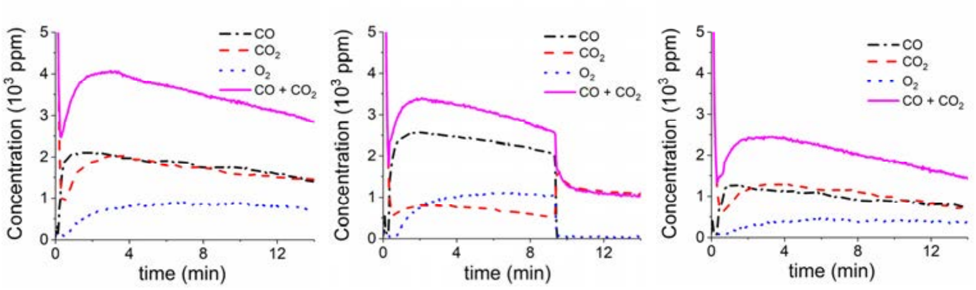

(a) (b) (c)

***Figure 3.6**: Concentration of the products of decomposition of sample A **(a)**, sample B **(b)**, and sample C **(c)**, with a temperature of 630°C in pure argon and flow rate of 30 ml min^{-1}; plasma power is 2.1 ± 0.1 W.*

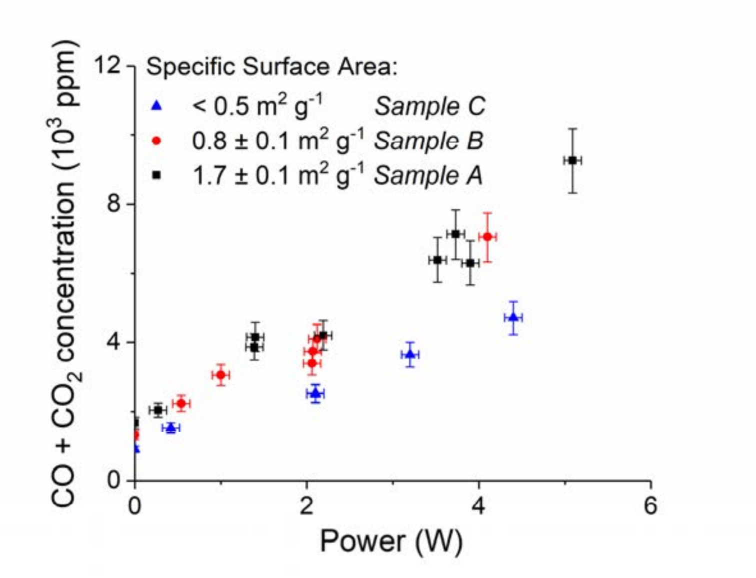

Figure 3.7: *Sum of CO_2 and CO concentrations plotted as function of power obtained during decomposition of $CaCO_3$ samples A, B, and C with different surface areas; all the experiments performed at 630°C, in pure argon, and flow rate 30 ml min^{-1}.*

Figure 3.8 shows the influence of particles size on $CaCO_3$ decomposition by comparing sample C (250–300 µm, Figure 3.7a), D (100–125 µm, Figure 3.7b), and E (38–45 µm, Figure 3.7c) at plasma powers varying between 1.3 and 2.1 W. Figure 3.8d shows details on the response time after switching on the plasma for the three samples. The time to reach steady state is 50, 40, and 10 seconds for samples C, D, and E, respectively. These times are in reasonable agreement with the Fourier times of $CaCO_3$ particles of these sizes. The different powers do not allow direct comparison of the decomposition rates. Instead, the effect of plasma power on the decomposition rate for samples C, D, and E is presented in Figure 3.9, showing that the particle size has no effect on the decomposition rate within experimental error. All the experiments addressed in Figures 3.7 and 3.9 are shown in detail in Figures A3.3–A3.7 in appendix A3.

Figure 3.10 shows the results of a series of plasma enhanced decomposition experiments in the presence CO_2 in the feed gas, measured on sample C. All experiments were done with one sample by performing 22 carbonation and decomposition cycles. The stability of the sample was verified by repeating decomposition measurements in the absence of plasma, demonstrating invariable results within 5%.

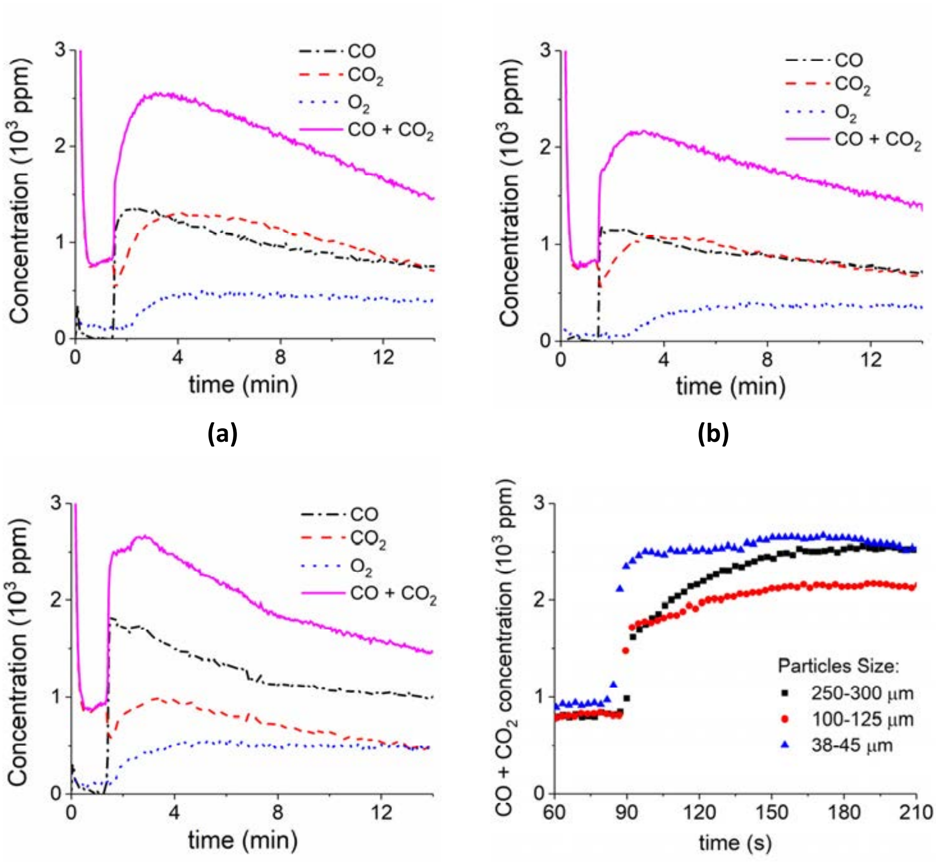

(a) (b)

(c) (d)

Figure 3.8*: Concentration of the products of decomposition of sample C* ***(a)****, sample D* ***(b)****, and sample E* ***(c)*** *as function of time with a temperature of 630 °C in pure argon and flow rate of 30 ml min^{-1}; plasma power is 2.1 W for sample C, 1.3 W for sample D, and 1.7 W for sample E.* ***(d)*** *Initial response of CO + CO$_2$ concentration after activating the plasma for all three samples.*

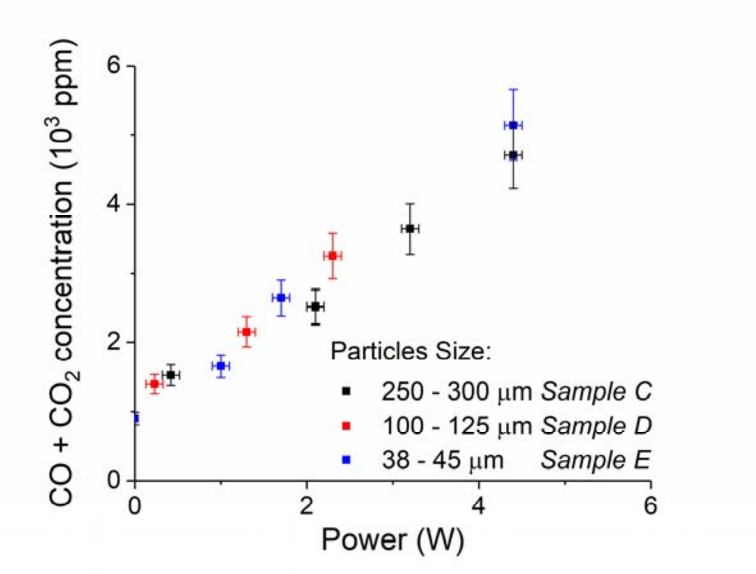

***Figure 3.9**: Sum of CO_2 and CO concentrations as function of power during decomposition of $CaCO_3$ samples with different particles size (samples C, D, and E); all the experiments were performed at 630°C, in pure argon, and at a flow rate 30 ml min^{-1}.*

Figure 3.11 shows the effect of CO_2 in the feed on plasma-enhanced decomposition at similar plasma powers, i.e., between 1.3 and 1.5 W. The reaction rate substantially decreases in presence of extra CO_2, as can be estimated based on the sum of the concentrations of CO and CO_2 minus the CO_2 concentration at the inlet. Furthermore, the CO concentration increases with increasing CO_2 concentration.

In order to correct for the differences in power, additional experiments at other plasma powers were performed as shown in Figures A3.8–A3.11 in Appendix A3 and the results allowed interpolation of the CO and CO_2 values to 1.5 W plasma power, resulting in Figure 3.11. As the CO_2 concentration varies along the axis of the reactor, an averaged value is calculated according to Equation (3.1):

$$[CO_2]_{ave} = \frac{[CO_2]_{in} + [CO_2]_{out}}{2} \tag{3.1}$$

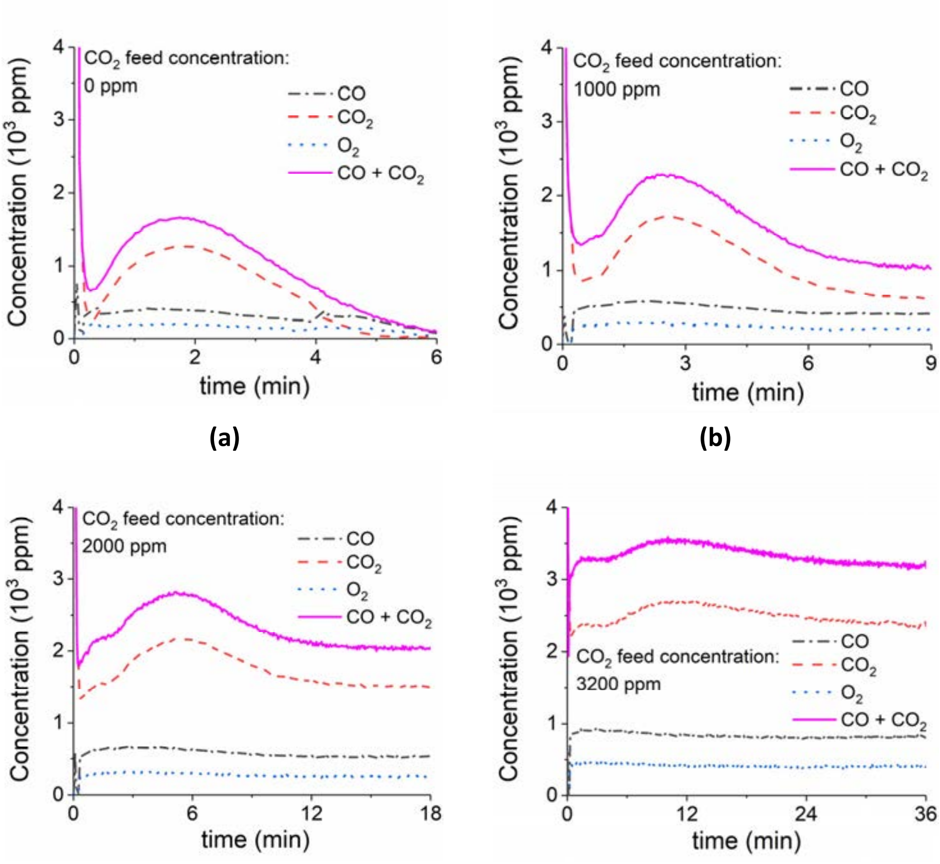

(a) **(b)**

(c) **(d)**

Figure 3.10: *CO + CO$_2$ (solid line), CO$_2$ (dashed line), CO (dash-dotted line), and O$_2$ concentrations monitored by mass spectrometry during CaCO$_3$ decomposition in different CO$_2$ feed concentrations in Ar and different plasma power. The amount of CaO is 6 mg, temperature is 630 °C, and flow rate is 90 ml min^{-1}. The fed CO$_2$ concentration is 0 ppm* ***(a)****, 1000 ppm* ***(b)****, 2000 ppm* ***(c)****, and 3200 ppm* ***(d)****. The plasma power is 1.5 W* ***(a)****, 1.3 W* ***(b)****, 1.3 W* ***(c)****, and 1.5 W* ***(d)****.*

The spread in the CO$_2$ concentration provides the window of concentrations occurring along the axis of the reactor; note this is not an error margin. Figure 3.12 confirms that the CO concentration indeed increases with increasing CO$_2$ concentration in the gas phase and this is observed for both CaCO$_3$ as well as the blank experiment with α-Al$_2$O$_3$ only, which is shown in Figure A3.12 in Appendix A3.

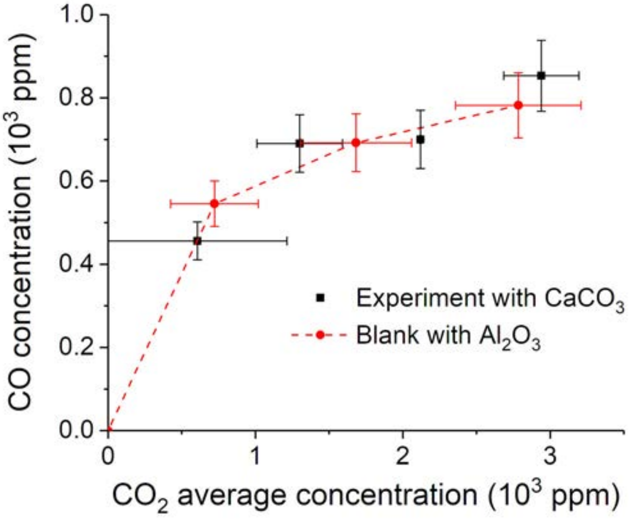

Figure 3.11*: CO outlet concentration vs. CO_2 average concentration obtained in a packed bed of 10 mg $CaCO_3$ and 90 mg Al_2O_3 at 630°C with different CO_2 concentrations in Ar and flow rate of 90 ml min^{-1} (squares); all results interpolated to 1.5 W plasma power. The same experiment was also performed with 100 mg Al_2O_3 only (circles). Error margins of the CO concentration are provided, as well as the window of the CO_2 concentrations (note these are not error margins).*

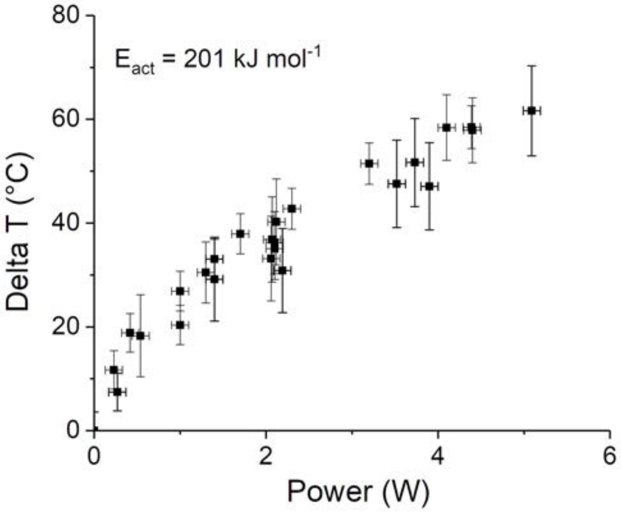

Figure 3.12*: Average increase of temperature in the plasma zone as function of power during the $CaCO_3$ decomposition previously shown. The activation barrier has been calculated in Chapter 2.*

3.4 Discussion

Scheme 3.1 presents a simple reaction scheme describing $CaCO_3$ decomposition, both in the absence and presence of plasma. Thermal decomposition without plasma involves exclusively R_1 (solid arrow), whereas in the presence of plasma both R_2 and R_3 might contribute. The observed enhancement of decomposition by plasma might be caused by plasma chemistry according R_2 and/or by enhancing R_1 via increasing temperature, as will be discussed below. Furthermore, we will discuss whether R_2 or R_3 is responsible for the formation of CO.

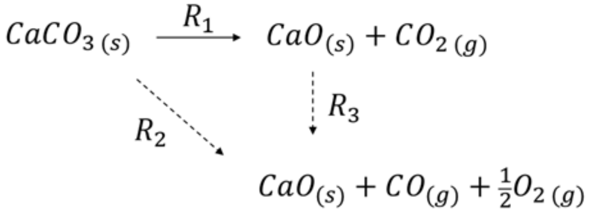

***Scheme 3.1**: $CaCO_3$ decomposition in Ar plasma.*

3.4.1 Formation of CO

Figure 3.11 shows that the CO formation rate is not affected by the presence of $CaCO_3$ in the plasma at low CO_2 feed concentrations. It is enhanced by feeding additional CO_2. Hence, we conclude that CO formation occurs only in the gas phase (R_3) and not on the $CaCO_3$ surface (R_2). The trend in Figure 3.11 also indicates that the order of CO formation in the CO_2 concentration is clearly smaller than one. This is qualitatively in line with the results of Ramakers et al. [25] and Butterworth et al. [27], reporting that Ar can enhance the activation of CO_2, which is attributed to the fact that the electron density is enhanced because Ar is much easier ionized than CO_2. On the other hand, one may also speculate that higher CO_2 concentration increases the probability of recombination of CO and O, quenching the reaction.

The formation of CO responds extremely fast to switching the plasma on, as can be seen in Figures 3.4, 3.5, 3.6 and 3.8, much faster than the CO_2 response as will be discussed below. This is in line with the conclusion that CO formation is plasma controlled. In cases when CO_2 concentration increase slowly in time (Figures 3.5 and 3.6), it can be seen that the CO concentration follows, which is in line with the conclusion that the consecutive pathway R_3 is dominant over R_2.

3.4.2 *Thermal effect or plasma chemistry?*

The decomposition rate at a fixed power depends on the total surface area, as can be observed from Figure 3.7. On the other hand, the decomposition rate remains constant within experimental error when varying the particles size and consequently the external surface area, as shown in Figure 3.9. Therefore, the external surface area has no influence on the rate of decomposition at any power. According to the Paschen's law, typically plasma cannot exist in pores smaller than 6 µm, implying that any plasma chemistry on the surface of $CaCO_3$ can exclusively contribute at the external surface of the particles. A recent work [56] revealed that penetration into relatively large pores is possible; however, the pores in $CaCO_3$ are much smaller, the electrical field is two orders of magnitude lower compared to [56], and the calculated penetration depth is limited to 5 µm, which is much smaller than the particle size used. Therefore, it seems reasonable to assume that penetration of plasma in this study is negligible. As the external surface area has no significant effect, we conclude that R_2 does not contribute. The enhancing effect of plasma power on the decomposition rate, as well as the observation that increasing the specific surface area increases the rate of decomposition (both in Figure 3.7), both suggest that plasma induced temperature increase is responsible for the increase in the decomposition rate. In fact, this is a result that can be expected operating with an Ar plasma because a chemical reaction between Ar ions and $CaCO_3$ would not be expected. The effect of DBD plasma containing H_2 in which plasma induced chemical reactions are much more likely, will be discussed in Chapters 5 using the methodology developed in this study.

Figure 3.12 shows the apparent temperature increase, as estimated based on the temperature that would be required to account for the increase in decomposition rate, based on the kinetics of the decomposition reaction calculated in Chapter 2. Remarkably, all observations converge to a single line independent of both surface area and particle size. The order of magnitude of the temperature increase is quite similar to results reported in literature. Typical temperatures estimated in DBD plasmas range up to typically 200 K [17,23,41–48]. It should be noted that determination of the temperature is cumbersome, e.g., the temperature of the exiting gas provides only a minimum value because of rapid heat exchange between small reactors and environment, whereas infrared cameras and UV–Vis spectroscopy measurements have limited accuracy. Nevertheless, the order of magnitude agrees well with our observations. In short, although experimental details vary, a temperature increase of 50 °C due to 4 W plasma power input is concluded.

The temperature regulation of the oven played an important role in our study. It stabilized the temperature at a few millimetres outside the low voltage electrode at 630 °C. Therefore, any power input from the plasma will result in a decrease of the electrical power to the oven. Hence, the temperature effect of the plasma is actually larger than estimated above, in contrast to all experiments performed at room temperature without any kind of temperature control.

The conclusion that thermal effects are dominant is further supported by the fact that the typical response time of the decomposition rate is in the order of one minute for large particles and somewhat faster for small particles (Figures 3.5 and 3.8d). The order of magnitude agrees well with the Fourier time of $CaCO_3$ particles of the sizes used. In any case, the response times are longer than response times observed for CO formation, as discussed above, which is in line with the conclusion that decomposition is thermally controlled, whereas CO_2 dissociation is obviously plasma controlled.

The conclusion is also reinforced by the fact that the sum of CO_2 and CO concentrations obtained by decomposition of sample C at 630 °C and 3.2 W plasma power corresponds to the CO_2 concentration obtained by decomposition at 680 °C (i.e., increasing the temperature of 50 °C as calculated in Figure 3.12) without plasma of the same sample, as observed by comparing figures A3.5a and A3.13 in Appendix A.

The proposed method is validated, since it enables to distinguish between thermal and plasma chemistry effect on the decomposition rate. This method is applicable to other systems in which a plasma is in contact with a fixed bed of porous particles, including supported catalysts. It should be noted that in general the increase in gas temperature in a DBD plasma cannot be neglected, as done frequently in many studies. Second, only the external surface of catalysts particles interacts with plasma: plasma–catalyst synergy is therefore maximal for nonporous catalytic materials. This method is going to be applied for $CaCO_3$ decomposition in H_2 plasma, discussed in Chapter 5.

3.5 Conclusions

The effect of argon plasma on calcium carbonate decomposition was herein assessed by means of a comparative method which allowed us to distinguish between thermal effects and plasma chemistry, based on reaction rates and dynamics. It represents a systematic method to distinguish between thermal effects versus plasma chemistry effect in fixed DBD plasma applications. Application of a DBD Ar plasma causes two effects when decomposing $CaCO_3$.

First, the rate of $CaCO_3$ decomposition increases. We conclude that this effect is purely a thermal effect, based on the fact that the rate of decomposition is enhanced when the total surface area is increased, whereas the external surface area has no influence. If the contact of plasma with $CaCO_3$ would dominate, the opposite would be expected. Furthermore, the dynamics of $CaCO_3$ decomposition follow the dynamics of heat transfer in $CaCO_3$ particles.

Second, plasma induces formation of CO. We conclude that this occurs via decomposition of CO_2 in the gas phase, based on the observation that the rate of CO formation is ruled by the CO_2 concentration as well as the observation that dynamic changes are very fast, as expected for plasma effect.

References

[1] E. C. Neyts, K. Ostrikov, M. K. Sunkara, and A. Bogaerts. Plasma Catalysis: Synergistic Effects at the Nanoscale. *Chem. Rev.* **2015**, 115, 13408–13446.

[2] E. C. Neyts, and A. Bogaerts. Understanding plasma catalysis through modelling and simulation—A review. *J. Phys. D Appl. Phys.* **2014**, 47, 224010.

[3] E. C. Neyts, K. Ostrikov, M. K. Sunkara, and A. Bogaerts. Plasma-Surface Interactions in Plasma Catalysis. *Plasma Chem. Plasma Process.* **2014**, 36, 13408–13446.

[4] J. C. Whitehead. Plasma-catalysis: The known knowns, the known unknowns and the unknown unknowns. *J. Phys. D Appl. Phys.* **2016**, 49, 243001.

[5] H. L. Chen, H. M. Lee, S. H. Chen, M. B. Chang, S. J. Yu, and S. N. Li. Removal of volatile organic compounds by single-stage and two-stage plasma catalysis systems: A review of the performance enhancement mechanisms, current status, and suitable applications. *Environ. Sci. Technol.* **2009**, 43, 2216–2227.

[6] D. Dobslaw, A. Schulz, S. Helbich, C. Dobslaw, and K. H. Engesser. VOC removal and odor abatement by a low-cost plasma enhanced biotrickling filter process. *J. Environ. Chem. Eng.* **2017**, 5, 5501–5511.

[7] T. Kozàk, and A. Bogaerts. Splitting of CO_2 by vibrational excitation in non-equilibrium plasmas: A reaction kinetics model. *Plasma Sources Sci. Technol.* **2014**, 23, 045004.

[8] B. Ashford, and X. Tu. Non-thermal plasma technology for the conversion of CO_2. *Curr. Opin. Green Sustain. Chem.* **2017**, 3, 45–49.

[9] I. Michielsen, Y. Uytdenhouwen, J. Pype, B. Michielsen, J. Mertens, F. Reniers, V. Meynen, and A. Bogaerts. CO_2 dissociation in a packed bed DBD reactor: First steps towards a better understanding of plasma catalysis. *Chem. Eng. J.* **2017**, 326, 477–488.

[10] M. Grofulović, T. Silva, B. L. Klarenaar, A. S. Morillo-Candas, O. Guaitella, R. Engeln, C. D. Pintassilgo, and V. Guerra. Kinetic study of CO_2 plasmas under non-equilibrium conditions. {I}. Relaxation of vibrational energy. *Plasma Sources Sci. Technol.* **2018**, 27, 15019.

[11] M. G. Sobacchi, A. V. Saveliev, A. A. Fridman, L. A. Kennedy, S. Ahmed, and T. Krause. Experimental assessment of a combined plasma/catalytic system for hydrogen production via partial oxidation of hydrocarbon fuels. *Int. J. Hydrogen Energy* **2002**, 27, 635–642.

[12] X. Tu, and J. C. Whitehead. Plasma-catalytic dry reforming of methane in an atmospheric dielectric barrier discharge: Understanding the synergistic effect at low temperature. *Appl. Catal. B Environ.* **2012**, 125, 439–448.

[13] W. C. Chung, M. B. Chang. Review of catalysis and plasma performance on dry reforming of CH_4 and possible synergistic effects. *Renew. Sustain. Energy Rev.* **2016**, 62, 13–31.

[14] B. S. Patil, Q. Wang, V. Hessel, and J. Lang. Plasma N_2-fixation: 1900–2014. *Catal. Today* **2015**, 256, 49–66.

[15] A. A. Fridman. Plasma Chemistry. *Cambridge University Press*: Cambridge, UK, **2008**.

[16] C. Tendero, C. Tixier, P. Tristant, J. Desmaison, and P. Leprince. Atmospheric pressure plasmas: A review. *Spectrochim. Acta Part B At. Spectrosc.* **2006**, 61, 2–30.

[17] H. H. Kim, Y. Teramoto, N. Negishi, and A. Ogata. A multidisciplinary approach to understand the interactions of nonthermal plasma and catalyst: A review. *Catal. Today* **2015**, 256, 13–22.

[18] R. Aerts, W. Somers, and A. Bogaerts. Carbon Dioxide Splitting in a Dielectric Barrier Discharge Plasma: A Combined Experimental and Computational Study. *ChemSusChem* **2015**, 8, 702–716.

[19] D. Mei, X. Zhu, Y. L. He, J. D. Yan, and X. Tu. Plasma-assisted conversion of CO_2 in a dielectric barrier discharge reactor: Understanding the effect of packing materials. *Plasma Sources Sci. Technol.* **2015**, 24, 015001.

[20] M. Nizio, A. Albarazi, S. Cavadias, J. Amouroux, M. E. Galvez, and P. da Costa. Hybrid plasma-catalytic methanation of CO_2 at low temperature over ceria zirconia supported Ni catalysts. *Int. J. Hydrogen Energy* **2016**, 41, 11584–11592.

[21] A. Bogaerts, T. Kozák, K. van Laer, R. Snoeckx. Plasma-based conversion of CO_2: Current status and future challenges. *Faraday Discuss.* **2015**, 183, 217–232.

[22] K. van Laer, and A. Bogaerts. Improving the Conversion and Energy Efficiency of Carbon Dioxide Splitting in a Zirconia-Packed Dielectric Barrier Discharge Reactor. *Energy Technol.* **2015**, 3, 1038–1044.

[23] F. Brehmer, S. Welzel, M. C. M. van de Sanden, and R. Engeln. CO and byproduct formation during CO_2 reduction in dielectric barrier discharges. *J. Appl. Phys.* **2014**, 116, 123303.

[24] Y. Uytdenhouwen, S. van Alphen, I. Michielsen, V. Meynen, P. Cool, and A. Bogaerts. A packed-bed DBD micro plasma reactor for CO_2 dissociation: Does size matter? *Chem. Eng. J.* **2018**, 348, 557–568.

[25] M. Ramakers, I. Michielsen, R. Aerts, V. Meynen, and A. Bogaerts. Effect of argon or helium on the CO_2 conversion in a dielectric barrier discharge. *Plasma Process. Polym.* **2015**, 12, 755–763.

[26] Y. Zeng, and X. Tu. Plasma-catalytic hydrogenation of CO_2 for the cogeneration of CO and CH_4 in a dielectric barrier discharge reactor: Effect of argon addition. *J. Phys. D Appl. Phys.* **2017**, 50, 184004.

[27] T. Butterworth, R. Elder, and R. Allen. Effects of particle size on CO_2 reduction and discharge characteristics in a packed bed plasma reactor. *Chem. Eng. J.* **2016**, 293, 55–67.

[28] S. Kameshima, K. Tamura, Y. Ishibashi, and T. Nozaki. Pulsed dry methane reforming in plasma-enhanced catalytic reaction. *Catal. Today* **2015**, 256, 67–75.

[29] S. Kameshima, K. Tamura, R. Mizukami, T. Yamazaki, and T. Nozaki. Parametric analysis of plasma-assisted pulsed dry methane reforming over Ni/Al_2O_3 catalyst. *Plasma Process. Polym.* **2017**, 14, 1600096.

[30] A. Ozkan, T. Dufour, G. Arnoult, P. de Keyzer, A. Bogaerts, and F. Reniers. CO_2-CH_4 conversion and syngas formation at atmospheric pressure using a multi-electrode dielectric barrier discharge. *J. CO_2 Util.* **2015**, 9, 78–81.

[31] X. Tu, H. J. Gallon, M. V. Twigg, P. A. Gorry, and J. C. Whitehead. Dry reforming of methane over a Ni/Al_2O_3 catalyst in a coaxial dielectric barrier discharge reactor. *J. Phys. D Appl. Phys.* **2011**, 44, 274001.

[32] H. J. Gallon, X. Tu, and J. C. Whitehead. Effects of reactor packing materials on H_2 production by CO_2 reforming of CH_4 in a dielectric barrier discharge. *Plasma Process. Polym.* **2012**, 9, 90–97.

[33] Y. Zeng, X. Zhu, D. Mei, B. Ashford, and X. Tu. Plasma-catalytic dry reforming of methane over γ-Al_2O_3 supported metal catalysts. *Catal. Today* **2015**, 256, 80–87.

[34] X. Zheng, S. Tan, L. Dong, S. Li, and H. Chen. Silica-coated $LaNiO_3$ nanoparticles for non-thermal plasma assisted dry reforming of methane: Experimental and kinetic studies. *Chem. Eng. J.* **2015**, 265, 147–156.

[35] R. Aerts, T. Martens, and A. Bogaerts. Influence of vibrational states on CO_2 splitting by dielectric barrier discharges. *J. Phys. Chem. C* **2012**, 116, 23257–23273.

[36] A. Bogaerts, W. Wang, A. Berthelot, and V. Guerra. Modeling plasma-based CO_2 conversion: Crucial role of the dissociation cross section. *Plasma Sources Sci. Technol.* **2016**, 25, 55016.

[37] L. D. Pietanza, G. Colonna, G. D’Ammando, M. Capitelli. Time-dependent coupling of electron energy distribution function, vibrational kinetics of the asymmetric mode of CO_2 and dissociation, ionization and electronic excitation kinetics under discharge and post-discharge conditions. *Plasma Phys. Control. Fusion* **2017**, 59, 14035.

[38] G. J. Van Rooij, D. C. van den Bekerom, N. Den Harder, T. Minea, G. Berden, W. A. Bongers, R. Engeln, M. F. Graswinckel, E. Zoethout, and M. C. M. van de Sanden. Taming microwave plasma to beat thermodynamics in CO_2 dissociation. *Faraday Discuss.* **2015**, 183, 233–248.

[39] W. Bongers, H. Bouwmeester, B. Wolf, F. Peeters, S. Welzel, D. van den Bekerom, N. den Harder, A. Goede, M. Graswinckel, P. W. Groen, et al. Plasma-driven dissociation of CO_2 for fuel synthesis. *Plasma Process. Polym.* **2017**, 14, 1600126.

[40] T. Minea, D. C. van den Bekerom, F. J. Peeters, E. Zoethout, M. F. Graswinckel, M. C. M. van de Sanden, T. Cents, L. Lefferts, and G. J. van Rooij. Non-oxidative methane coupling to C_2 hydrocarbons in a microwave plasma reactor. *Plasma Process. Polym.* **2018**, 15, 1800087.

[41] S. Li, W. Zheng, Z. Tang, and F. Gu. Plasma heating and temperature difference between gas pellets in packed bed with dielectric barrier discharge under natural convection condition. *Heat Transf. Eng.* **2012**, 33, 609–617.

[42] N. Jidenko, E. Bourgeois, and J. P. Borra. Temperature profiles in filamentary dielectric barrier discharges at atmospheric pressure. *J. Phys. D Appl. Phys.* **2010**, 43, 295203.

[43] B. S. Patil, N. Cherkasov, J. Lang, A. O. Ibhadon, V. Hessel, and Q. Wang. Low temperature plasma-catalytic NO_x synthesis in a packed DBD reactor: Effect of support materials and supported active metal oxides. *Appl. Catal. B Environ.* **2016**, 194, 123–133.

[44] T. Nozaki, T. Hiroyuki, and K. Okazaki. Hydrogen enrichment of low-calorific fuels using barrier discharge enhanced Ni/γ-Al_2O_3 bed reactor: Thermal and nonthermal effect of nonequilibrium plasma. *Energy Fuels* **2006**, 20, 339–345.

[45] N. Masoud, K. Martus, M. Figus, and K. Becker. Rotational and vibrational temperature measurements in a high-pressure cylindrical dielectric barrier discharge (C-DBD). *Contrib. Plasma Phys.* **2005**, 45, 32–39.

[46] P. Rajasekaran, C. Opländer, D. Hoffmeister, N. Bibinov, C. V. Suschek, D. Wandke, and P. Awakowicz. Characterization of dielectric barrier discharge (DBD) on mouse and histological evaluation of the plasma treated tissue. *Plasma Process. Polym.* **2011**, 8, 246–255.

[47] Y. Du, G. Nayak, G. Oinuma, Y. Ding, Z. Peng, and P. J. Bruggeman. Emission considering self-absorption of OH to simultaneously obtain the OH density and gas temperature: Validation, non-equilibrium effects and limitations. *Plasma Sources Sci. Technol.* **2017**, 26, 095007.

[48] J. Florian, N. Merbahi, G. Wattieaux, J. M. Plewa, and M. Yousfi. Comparative Studies of Double Dielectric Barrier Discharge and Microwave Argon Plasma Jets at Atmospheric Pressure for Biomedical Applications. *IEEE Trans. Plasma Sci.* **2015**, 43, 3332–3338.

[49] J. Blamey, E. J. Anthony, J. Wang, and P. S. Fennell. The calcium looping cycle for large-scale CO_2 capture. *Prog. Energy Combust. Sci.* **2010**, 36, 260–279.

[50] B. J. McBride, M. J. Zehe, and S. Gordon. NASA Glenn Coefficients for Calculating Thermodynamic Properties of Individual Species **2002**.

https://www.grc.nasa.gov/WWW/CEAWeb/TP-2002-21556.htm

[51] P. S. Fennell, R. Pacciani, J. S. Dennis, J. F. Davidson, and A. N. Hayhurst. The effects of repeated cycles of calcination and carbonation on a variety of different limestones, as measured in a hot fluidized bed of sand. *Energy Fuels* **2007**, 21, 2072–2081.

[52] A. I. Lysikov, A. N. Salanov, and A. G. Okunev. Change of CO_2 carrying capacity of CaO in isothermal recarbonation-decomposition cycles. *Ind. Eng. Chem. Res.* **2007**, 46, 4633–4638.

[53] R. H. Borgwardt. Sintering of nascent calcium oxide. *Chem. Eng. Sci.* **1989**, 44, 53–60.

[54] Y. R. Zhang, K. van Laer, E. C. Neyts, and A. Bogaerts. Can plasma be formed in catalyst pores? A modeling investigation. *Appl. Catal. B Environ.* **2016**, 185, 56–67.

[55] K. Hensel, S. Katsura, and A. Mizuno. DC Microdischarges inside porous ceramics. *IEEE Trans. Plasma Sci.* **2005**, 33, 574–575.

[56] Q. Z. Zhang, W. Z. Wang, and A. Bogaerts. Importance of surface charging during plasma streamer propagation in catalyst pores. *Plasma Sources Sci. Technol.* **2018**, 27, 065009.

[57] F. J. J. Peeters, and M. C. M. van de Sanden. The influence of partial surface discharging on the electrical characterization of DBDs. *Plasma Sources Sci. Technol.* **2015**, 24, 15016.

[58] M. Ghassemi, H. Mohseni, K. Niayesh, and A. A. Shayegani. Dielectric Barrier Discharge (DBD) Dynamic Modeling for High Voltage Insulation. *Proceedings of the 2011 Electrical Insulation Conference (EIC)*, Annapolis, MD, USA, **2011**.

[59] A. Jess, and P. Wasserscheid. Chemical Technology; An Integrated Textbook. *Wiley,* Hoboken, NJ, USA, **2013**.

[60] G. K. Jacobs, D. M. Kerrick, and K. M. Krupka. The High-Temperature Heat Capacity of Natural Calcite ($CaCO_3$). *Phys. Chem. Miner.* **1981**, 7, 55–59.

Chapter 4

Synergy between Dielectric Barrier Discharge Plasma and Calcium Oxide for Reverse Water Gas Shift

Summary

Chapter 4 reports on synergy between Dielectric Barrier Discharge plasma and calcium oxide as a catalyst for the Reverse Water Gas Shift (RWGS). Any effect of the presence of the catalyst on the contribution of plasma chemistry, i.e. chemical conversion in the plasma, is minimized by using a fixed bed of α-Al_2O_3 particles as a blank experiment and adding a small amount of calcium oxide, with similar dielectric constant, particle size and shape. This approach results in constant plasma power and ensures also that the residence time and specific energy input remain unchanged. Furthermore, synergy is determined based on reaction rates at fixed conditions, i.e. concentrations and temperature, based on kinetic equations derived from integral experiments, describing both thermal operation and plasma operation and both in absence and presence of calcium oxide. This approach has not been applied so far to study plasma-catalysis synergy. The experimental results in thermal and plasma operation are well described with kinetic equations based on power rate laws. Synergy is observed at the lower operational temperatures (640°C) with a rate-enhancement factor of 1.7, steadily decreasing with increasing temperature until disappearing at 750°C. The concentrations of CO_2, H_2 and H_2O have no significant influence. Synergy is attributed to a new reaction pathway involving interaction of plasma activated intermediates with the CaO surface, with a relatively low apparent activation barrier of 40 kJ mol^{-1}. Much higher activation barriers are observed for both thermal-catalytic RWGS on CaO (140 kJ mol^{-1}) as well as for plasma operation with Al_2O_3 only (90 kJ mol^{-1}). We suggest

that reaction of surface $CaCO_3$ with plasma generated H radicals is the rate determining step, in contrast to plasma chemistry where CO_2 cannot be activated with H radicals.

4.1 Introduction

Plasma catalysis is receiving more and more attention in the last few years, since the specific interactions between plasma and catalyst surface may lead to synergistic effects [1-3]. In the last decade research has been focused on conversion of CO_2 [4-8], conversion of hydrocarbons via dry reforming and coupling [9-11] as well as activation of N_2 [12, 13]. Ammonia synthesis is an example of an exothermic reaction, where plasma catalysis holds promise because of activation of N_2 at low temperature. Methane coupling and CO_2 dissociation are examples of endothermic reactions, which are more challenging, especially when aiming at conversion beyond thermodynamic equilibrium.

Dielectric Barrier Discharge (DBD) plasma reactors are frequently used for studying plasma-catalytic conversion [14-16]. The high AC voltages applied at relatively low frequency (50 to 10^5 Hz) produces a non-equilibrium plasma with very high electron temperatures (1–10 eV equal to 10^4–10^5 K), rather high vibrational temperatures (10^3 K), and rather low rotational and translational temperatures, i.e. the temperature of the gas. Therefore, any temperature increase induced by the plasma is typically smaller than 100 K [14, 16]. The concept that energy would be directed directly to bond breaking, without the need to heat up the gas mixture completely, is very attractive as heat exchangers to recover the heat would become redundant. The presence of a dielectric between the two electrodes prevents the formation of hot plasma in sparks, forming instead several microfilaments, resulting in a more uniform plasma. The low gas temperature allows application of a catalyst directly in the plasma without fast sintering and deactivation. Moreover, relatively low temperatures are required for catalysis in the first place, enabling adsorption of molecules, possibly vibrationally excited. Starting and stopping plasma reactors can be achieved much faster than usual thermal reactors, which is an advantage when fast capacity changes are required, e.g. in connection with intermittent energy supply and storage. Furthermore, DBD plasma can be generated at atmospheric pressure, which is interesting from the application point of view.

Promising results were presented for several reactions, including CO_2 decomposition and hydrogenation [4, 6, 17-27] and dry reforming of CH_4 [9, 10, 28-35], in terms of high conversion and selectivity. However, the main issue of DBD reactors remains the low energy efficiency achieved, i.e. the ratio between chemical energy stored in the produced molecules and electrical energy applied, which rarely surpasses 10%. This is caused by both energetically very expensive dissociative excitation by electron impact, consuming a significant part of the energy supplied, as well as dissipation of vibrational excitation to translation and rotation modes, i.e. heating up [36-39]. Microwave plasma reactors, using GHz frequencies, are at one hand more suitable because of less dissociative excitation, but at the other hand operate at much higher temperatures [40-42], limiting the opportunities for plasma catalysis.

Interaction between plasma and catalyst proceeds in many ways [1, 2]. The plasma will produce new chemical species including activated species, such as radicals and ions, which may adsorb on the catalyst surface, opening new reaction pathways and influencing the products distribution. Plasma can also induce photocatalytic effects by generating UV irradiation, impingement of charged particles and thermal fluctuations. The surface and subsurface of a catalyst can be modified by plasma via poisoning, implantation, sputtering, and etching. The presence of a catalyst influences the plasma by changing the electrical field distribution, but also modifying the free volume and the residence time in the plasma zone. A DBD plasma in an empty reactor is by nature filamentary, while a packed bed DBD plasma is enhanced at the contact points between particles [43-45]. For all these reasons the effects of plasma and catalyst on a specific reaction are strongly correlated and could result in synergy, i.e. when the reaction rate in presence of both catalyst and plasma is higher than the sum of the rates in presence of plasma-only and catalyst-only at identical conditions [1].

Plasma-catalytic CO_2 hydrogenation has been studied for methanation [18, 22, 26, 46-48], production of methanol [25, 49] and Reverse Water Gas Shift [22, 27]. The catalysts used in these studies have been selected based on their favourable performance in thermal catalysis, e.g. Ni on various supports for methanation [17, 21, 25, 46], Cu for methanol production [24] and Au for RWGS [26]. These studies focused on the assessment of synergy and many claim synergistic effects based on the observation that conversion during thermal operation is low, whereas combination of plasma and catalyst increased the conversion significantly [18, 22, 26, 46-49]. The effect of temperature increase induced by the plasma is explicitly considered in only one study [25]. Moreover, conversion in plasma-only and in plasma with catalyst is compared in some studies without addressing the effect of the presence of the fixed bed catalyst on the plasma properties [18, 25, 47-49]. The presence of the catalyst as a dielectric material will induce changes in the electrical field distribution, electron energy distribution and number of streamers or surface discharges [19, 24, 43-45]. Finally, changes in residence time or in Specific Energy Input (SEI, energy input per molecule feed) between empty and packed bed reactors were often not considered [18, 25, 47-49]. The approach used in Chapter 4 focuses on minimizing any differences in the plasma, residence time and SEI by keeping the properties of the packed bed almost completely constant. Any thermal effects of the plasma will be estimated and corrected for, based on the estimation of temperature in the plasma made in Chapter 3.

$CaCO_3$ decomposition is the key-step in the Calcium Looping Cycle, a promising option for CO_2 separation [50]. In this process, CO_2 is absorbed by calcium oxide forming $CaCO_3$, which can be either landfilled or recycled via decomposition, regenerating the sorbent calcium oxide. However, the decomposition reaction requires high temperatures in order to achieve high CO_2 concentrations in the outlet, i.e. at least 950°C to obtain pure CO_2 at atmospheric pressure [51]. Such temperatures result in sintering, decreasing the CO_2 capture capacity [52-54]. An approach would be to induce decomposition at lower temperatures by using a non-thermal plasma. Chapter 3 showed that a DBD argon plasma has no effect on the decomposition, except for a modest increase in temperature; the plasma only induces dissociation of part of the CO_2 in a consecutive reaction. On the other hand, the presence of hydrogen without plasma decreases the decomposition temperature [55], which has been confirmed by our experiments. Furthermore, the presence of hydrogen causes a shift in the product distribution to CO_2, CO and H_2O instead of CO_2 only. CO may be produced via RWGS (R_3) or directly via $CaCO_3$ hydrogenation (R_2), as presented in the following scheme

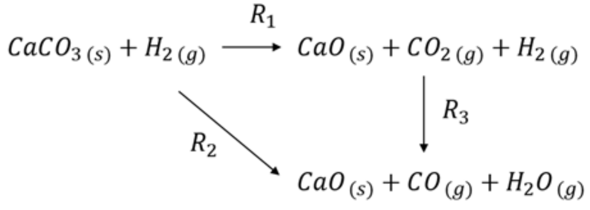

Scheme 4.1: Proposition of $CaCO_3$ decomposition in presence of H_2.

The introduction of plasma further decreases the decomposition temperature forming the same set of products, i.e. CO_2, CO and H_2O, as it will be discussed in Chapter 5. The interpretation of these results requires a description of RWGS (R_3 in scheme 4.1) both thermally and in presence of plasma. The goal of Chapter 4 is to provide a kinetic description of RWGS in presence of calcium oxide and plasma in a temperature window relevant for $CaCO_3$ decomposition, allowing determination of any synergy between plasma and calcium oxide as catalyst based on reaction rates. The synergetic effect will be discussed in terms of interactions of activated species with calcium oxide, by minimizing any influence of the catalyst on the properties of the plasma and consequently the chemical reactions proceeding in the plasma.

4.2 Materials and methods

4.2.1 Calcium oxide, calcium carbonate and alumina preparation

Calcium oxide was synthesized by calcination of $CaCO_3$ (99%, Sigma Aldrich) in 20% air in N_2 at atmospheric pressure in order to remove any organic contaminants, heating the sample until 900°C (heating rate 15°C min^{-1}) and keeping the temperature at 900°C for 3 hours. The calcined product was pelletized (pressure 160 bar), crushed and sieved in the particles size range of 250-300 um. Part of the calcium oxide particles thus prepared, was converted to $CaCO_3$ by calcination in 20% CO_2 in N_2 at 630°C for 5 hours (heating rate 15°C min^{-1}) and consecutively sintering in pure CO_2 at 900°C for 24h (heating rate 15°C min^{-1}). The material was sieved again in order to ensure the particle size range of 250-300 μm. α-alumina (99%, Alfa-Aesar) was treated, pelletized, crushed and sieved following the same procedure.

4.2.2 Characterization

The specific surface area, pore volume and pore size distribution of the samples were measured both in CaO form as well as in $CaCO_3$ form, after carbonation. The samples were first degassed at 300°C in vacuum for 3 hours. The surface area was calculated based on the BET isotherm for N_2 adsorption at -196°C in a Micrometrics Tristar 3000 analyser. The pore size distribution was measured by Hg porosimetry in a Quantachrome PoreMaster 33 analyser. The elemental composition was determined with X-Ray Fluorescence analysis (XRF, Bruker S8 Tiger).

4.2.3 Reactor Setup

Figure 4.1 shows a schematic representation of the equipment used to measure plasma enhanced RWGS. The fixed bed reactor is fed with a mix of Ar, H_2, CO_2 and H_2O. Argon is saturated with water and diluted with a pure argon stream in order to vary the water concentration. The temperature of the oven is controlled with a Eurotherm controller with an accuracy of ± 0.5°C between room temperature and 1000°C, as reported previously [50]. The isothermal zone is 8 cm long at 900°C, defined as the part of the reactor with less than ± 1°C temperature variation. A Quadrupole Mass Spectrometer (MS) measures the composition of the gas mixture leaving the reactor. The MS signal for CO_2 (44 m/e) and CO (28 m/e) are calibrated between 0.16% and 5% CO_2 and at 5% CO, resulting in a linear relationship. The reactor is a 4 mm inner- and 6 mm outer-diameter quartz tube. The inner electrode is a stainless-steel rod of 1 mm diameter placed co-axially in the centre of the reactor section by the help of a spacer, which is removed when the rod and the packed bed are positioned. The outer electrode is a 1 cm long stainless-steel tube with 6 mm inner diameter, enclosing a plasma zone of 0.035 cm^3 in volume. The plasma zone was filled completely with either 100 mg α-Al_2O_3 or with 10mg $CaCO_3$ and 95mg α-Al_2O_3 for the blank and catalytic experiments respectively, in order to minimize any change in the plasma. Note that the blank experiment includes also any possible contribution of the reactor wall and the surface of the electrode. An AC voltage of up to 5 kV peak to peak is applied to the inner electrode with a constant frequency of 23.5 kHz using a PMV 500-4000 power supply, while the outer electrode is connected to the ground via a probe capacitor of capacity 4 nF. The power of the plasma is calculated using the Lissajous method by measuring the voltage on the inner electrode with a Tektronix P6015A high voltage probe and on the outer electrode with a TT – HV 250 voltage probe as described in literature [56]. An example of Lissajous plot is shown in Figure A4.1 of the Appendix A4.

4.2.4 Steady state RWGS experiments in CaO and Al_2O_3

Either 10 mg $CaCO_3$ with 95 mg Al_2O_3 or 100 mg α-Al_2O_3 are placed in the reactor. In most experiments, the $CaCO_3$ is decomposed in-situ by heating in Ar to 680°C, resulting in a mixture of 6 mg CaO and 95 mg α-Al_2O_3. This sample is termed "CaO + Al_2O_3", as opposed to "$CaCO_3$ + Al_2O_3" when no in-situ decomposition is applied. The reactor containing alumina only is termed "Al_2O_3".

RWGS experiments were initiated by switching the gas composition from pure Ar to CO_2, H_2 and H_2O in Ar, at the selected temperature and constant flow rate of 90 ml/min. The temperature and concentration of CO_2, H_2 and H_2O are varied between 630 and 820°C, 0.1 and 0.4%, 2 and 10%, 0 and 0.25% respectively. The reactor reached steady state in typically 10 minutes after changing conditions. The plasma power is kept constant at either 0 W (plasma-off) or 1 ± 0.1 W (plasma-on) during the experiment. The CO_2 conversion is calculated based on the CO_2 and CO concentrations in the exit of the reactor according Equation 4.1; considering exclusively concentrations measured at the exit at the same time minimizes experimental error caused by drift in the sensitivity of the MS. No correction in the volumetric flow is required since RWGS is the only reaction taking place.

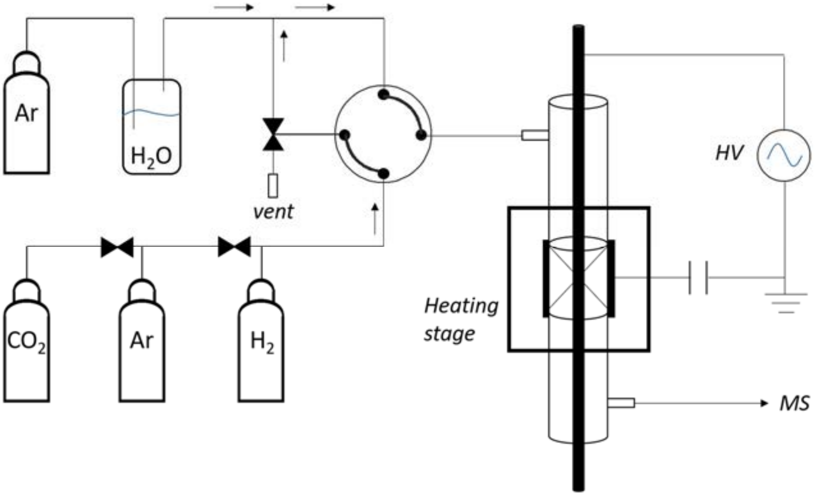

***Figure 4.1**: Plasma reactor setup used for this study.*

$$X_{CO2} = \frac{C_{CO,out}}{C_{CO,out} + C_{CO2,out}} \tag{4.1}$$

Reproducibility was tested by repeating experiments with both different samples and different reactor tubes.

4.3 Results

CaO and Al_2O_3 surface areas after short exposure to ambient condition are 5 m^2 g^{-1} and 16 m^2 g^{-1} respectively. XRF data show that the CaO is 99.12% pure with minor contamination of SiO_2 and Al_2O_3, while alumina is 99.9% pure with minor contamination of CaO.

4.3.1 RWGS over CaO and Al_2O_3

Figure 4.2 shows the CO_2 conversion during RWGS over "Al_2O_3", as well as "CaO + Al_2O_3", as function of temperature as well as the concentration of CO_2, H_2 and H_2O. The conversions are calculated based on the composition of the outlet stream at the different conditions as shown in figures A4.2 and A4.3 of the Appendix A4. No other products except CO and H_2O have been observed by MS and the mass balance closes within 5%. The sample "CaO + Al_2O_3" showed mild deactivation of 30% during the first 3 hours of operation at 820°C and no further deactivation was observed, as shown in figure A4.4 in Appendix A4. The data shown in figure 4.2 are collected after stabilization for 3h.

The results show that calcium oxide is active for RWGS, while Al_2O_3 is surprisingly also active, although significantly less. Note that no conversion was observed in an empty reactor. Figure 4.2 shows that CO_2 conversion increases with temperature and hydrogen concentration, while it decreases with CO_2 and H_2O concentration for both samples. Most of the results are obtained far from thermodynamic equilibrium, as can be seen in Figure 4.2.

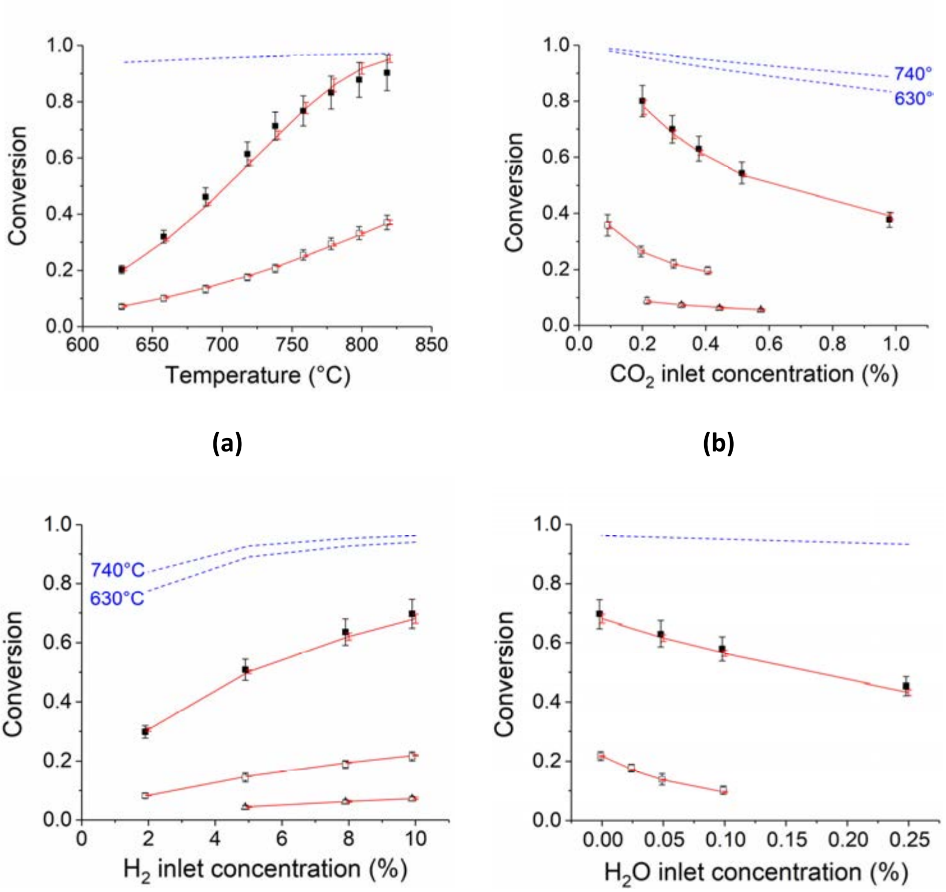

(a) **(b)**

(c) **(d)**

Figure 4.2: *CO_2 conversion as function of temperature, CO_2, H_2 and H_2O inlet concentration for experiments of RWGS in thermal operation on "CaO + Al_2O_3" (■) and on "Al_2O_3"(□,△), results from modeling (—) and conversion at thermodynamic equilibrium (⋯); flow rate is 90 ml min^{-1};* ***(b-d):*** *temperatures are 630°C (△) and 740°C (□,■);****(a):*** *feed is 0.3% CO_2, 10% H_2 and 0% H_2O in Ar****; (b):*** *feed is 10% H_2 and 0% H_2O in Ar;* ***(c)****: feed is 0.3% CO_2 and 0% H_2O in Ar;* ***(d)****: feed is 0.3% CO_2 and 10% H_2 in Ar.*

Figure 4.3 shows the CO_2 conversion during RWGS on "$CaCO_3$ + Al_2O_3" sample. The conversion levels are calculated based on data shown in figure A4.5 in Appendix A4, showing that the temperature was increased stepwise. Apparently, $CaCO_3$ is not active for RWGS because it shows the same conversion as "Al_2O_3" sample. The sharp increase in conversion between 760 to 780°C is caused by rapid decomposition of $CaCO_3$ to CaO, as at the same time the sum of CO_2 and CO concentrations in the product increase to much higher values than the CO_2 concentration in the feed, as shown in figure A6 in the window between 253 and 260 minutes. Afterwards, the mass balance closes again within 5%, indicating that the sample is mostly converted to CaO, resulting in a much higher activity. The increase in the sum of CO_2 and CO concentrations in figure A6 corresponds to 91 µmol of desorbed CO_2, indicating that the sample is at least 90% converted to CaO. Thus, calcium oxide is not converted to calcium carbonate during the experiments shown in figure 4.2, since the conversion is always significantly higher than the conversion over Al_2O_3. Furthermore, the experiments in figure A3 never showed an offset of the mass balance, which would indicate the formation of $CaCO_3$. Clearly, the CO_2 inlet concentration lower than 0.5% is too low to cause formation of carbonate even at 630°C, in agreement with the fact that the equilibrium CO_2 partial pressure for $CaCO_3$ decomposition is 0.7% at atmospheric pressure [51].

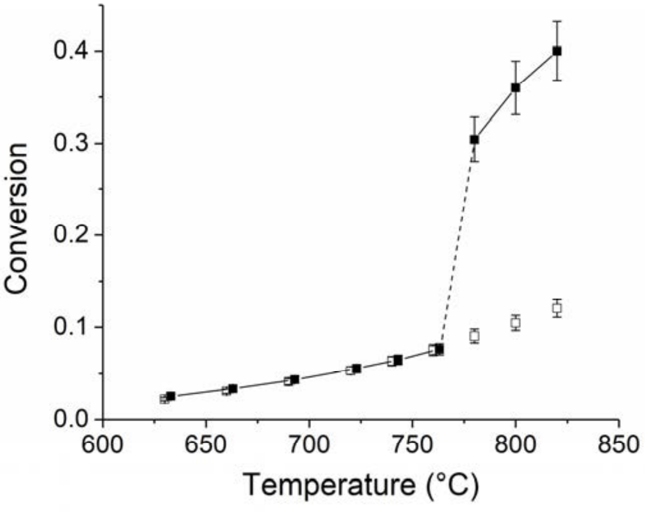

Figure 4.3: *CO_2 conversion as function of temperature during experiments of RWGS in thermal operation on "$CaCO_3$ + Al_2O_3" (■) and "Al_2O_3"(□), transition between $CaCO_3$ and CaO (···); feed is 6% CO_2, 10% H_2 and 0% H_2O in Ar, flow rate is 90 ml min^{-1}.*

4.3.2 Effect of Plasma on RWGS over CaO and Al_2O_3

Figure 4.4 shows the CO_2 conversion obtained during RWGS experiments on “Al_2O_3” and “CaO + Al_2O_3” in presence of plasma. The conversion values are obtained based on the outlet concentrations shown in figures A4.6 and A4.7 in the Appendix A4.

The plasma power is kept fixed at 1 W and the Lissajous plots measured on the two samples show no significant differences, as illustrated in figure A4.1 of the Appendix A4. Apparently, the plasma remains similar when adding 6 mg of CaO to 100 mg of Al_2O_3 with similar particle-size and -shape as well as dielectric constant, resulting in similar capacity of the plasma reactor, electrical field distribution and power dissipation.

The results shown in figure 4.4 are corrected for a temperature increase of 10°C. The estimation is based on the kinetics of $CaCO_3$ decomposition in argon plasma measured using the same “$CaCO_3$ + Al_2O_3” sample and reported Chapter 3 of this thesis.

For both samples, the conversion increases as function of temperature and decreases with CO_2 and H_2O feed concentration. Remarkably, the CO_2 conversion increases with H_2 concentration only when CaO is present, while it shows no significant changes with Al_2O_3 only. Note that the conversion approaches equilibrium for many experimental conditions in the presence of CaO. The conversion in presence of plasma is substantially higher respect to the experiments performed in absence of plasma at the same conditions as shown in figure 4.2 and it further increases in presence of CaO.

In addition to CO and H_2O, also trace amounts of CH_4 were detected, but due to the very low concentration no significant trend is observed, thus methane production is not discussed further. It was ensured that no carbon deposition occurred, based on the observation that no CO_2 is formed during oxidation of the sample in 10% air in argon plasma at 630°C and plasma power of 3 W after the experiments. The reason for the mild deactivation observed in figure A4.4 remains unknown but change of activity during initial operation is frequently observed in catalysis.

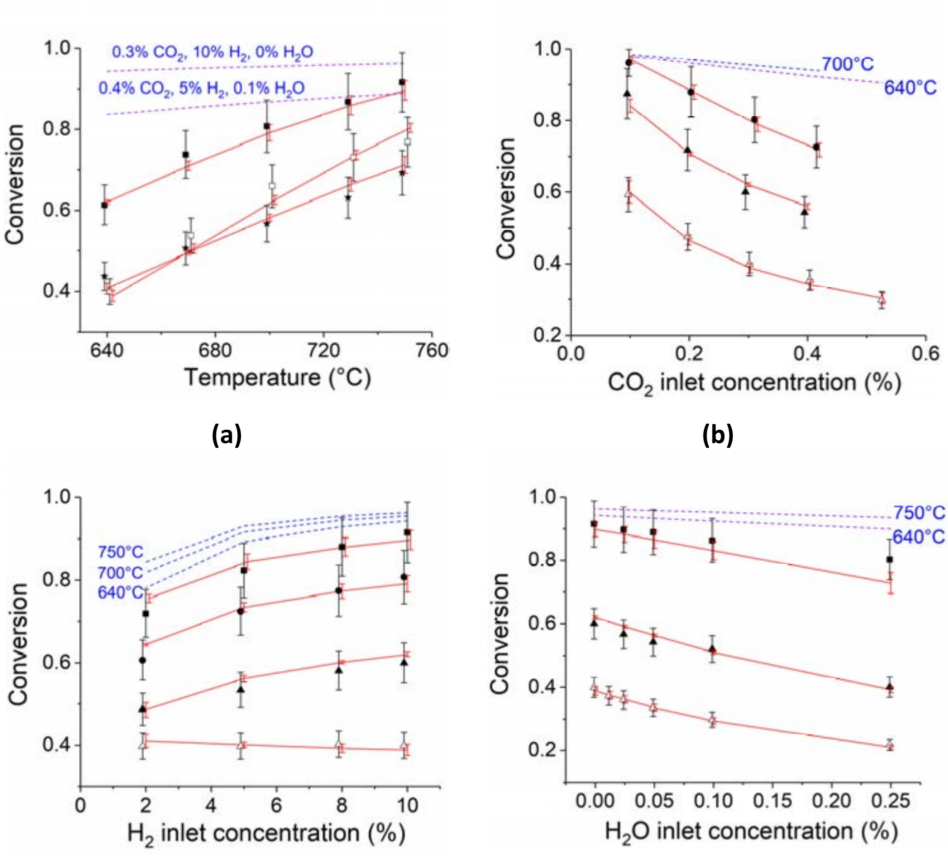

(a) **(b)**

(c) **(d)**

Figure 4a-d: *CO_2 conversion as function of temperature, CO_2, H_2 and H_2O inlet concentration for experiments of RWGS in plasma operation on "CaO + Al_2O_3" (■,▲,●,★) and on "Al_2O_3"(□,△), results from modelling (—) and conversion at thermodynamic equilibrium (···); flow rate is 90 ml min^{-1} and plasma power is 1 ± 0.1 W;* ***(b-d)****: temperatures are 640°C (△,▲), 700°C (●) or 750°C (□,■);* ***(a)****: feed is 0.3% CO_2, 10% H_2 and 0% H_2O in Ar (■,□) or 0.4% CO_2, 5% H_2 and 0.1% H_2O in Ar (★);* ***(b)****: feed is 10% H_2 and 0% H_2O in Ar;* ***(c)****: feed is 0.3% CO_2 and 0% H_2O in Ar;* ***(d)****: feed is 0.3% CO_2 and 10% H_2 in Ar.*

4.4 Discussion

4.4.1 Kinetic description

The results in Figures 4.2 and 4.4 show that CaO, as well as Al_2O_3 to lesser extent, is active for RWGS. The fact that equilibrium is never approached implies that conversion is determined by kinetics. CO_2 conversion increase with increasing temperature, indicating that RWGS on "Al_2O_3" and "CaO + Al_2O_3" is an activated process both in thermal and in plasma operation. CO_2 conversion decrease with increasing CO_2 and H_2O concentrations in all cases, both in thermal and in plasma operation. The apparent negative order in CO_2 is suggesting competitive adsorption of CO_2 and H_2. Also, the poisoning effect of H_2O points to competitive adsorption in case of catalytic operation, as experiments are performed far from thermodynamic equilibrium. The results in Figures 4.2 and 4.4 also show that the conversion increases with the hydrogen concentration in thermal operation as well as on "CaO + Al_2O_3" in plasma operation. In contrast, the conversion doesn't change significantly with hydrogen concentration on "Al_2O_3" in plasma operation.

In order to judge whether there is synergy between plasma and the CaO catalyst, the reaction rate obtained on "CaO" in thermal operation and on "Al_2O_3" in plasma operation must be compared to the rate obtained on "CaO + Al_2O_3" in plasma operation. The results in figure 4.2 and 4.3 show significant conversion and therefore do not allow direct calculation of reaction rates at one specific temperature, as would be possible in a differential experiment, i.e. conversion is less than typically 10%. In an integral experiment, concentration profiles develop along the axis of the reactor and the local reaction rates vary. Consequently, a valid mathematical description is needed of the kinetics of the reaction catalysed by alumina and CaO, with and without the presence of the plasma, in order to compare respective reaction rates at identical conditions.

A mechanism-inspired rate equation is used to model the reaction rate for the four cases, i.e. "CaO" and "Al_2O_3" in thermal operation, "CaO + Al_2O_3", "CaO" and "Al_2O_3" in plasma operation. The rate on "CaO" is calculated by subtracting the contribution of "Al_2O_3" both in thermal and in plasma operations, since alumina appeared not inert. Nevertheless, the equation serves solely as mathematical description of the system and is not related to a micro-kinetic model. Equation (4.2) is used for this purpose, allowing for an accurate description of the kinetics considering the following assumptions, based on the observations discussed above:

- reactant CO_2 and the product H_2O adsorb competitively on both Al_2O_3 and CaO, while CO is assumed to desorb quickly;
- The orders in CO_2 and H_2, i.e. a and b respectively, as well as the adsorption equilibrium constant of the water (K_{H2O}) are assumed constant with varying reaction conditions;
- The reaction occurs on Al_2O_3 and CaO independently.
- The equation also includes a term describing the reversed reaction (WGS) when the conversion approaches the thermodynamic equilibrium, according to the equilibrium constant $K_{eq,th}$ [51], which is particularly the case for "CaO + Al_2O_3" in plasma operation, as shown in figure 4.4.

$$R_{co} = \frac{k_0 \exp\left(\frac{-E_a}{RT}\right)[CO_2]^a[H_2]^b\left(1-\frac{K_{eq,obs}}{K_{eq,th}}\right)}{1+[H_2O]K_{H2O}} \tag{4.2}$$

The same equation is used for the four cases, obviously resulting in different fitting parameters.

The packed bed zone was modelled in 10000 segments, in which the concentration of the gases was calculated using equation (4.2) iteratively. Values for the fitting parameters were selected by optimizing the fit to the experimental observations. A MATLAB script was developed for that purpose, presented in Appendix A4.

The values of the fitted parameters k_0, E_{act}, a, b and K_{H2O} are presented in Table 4.1. The error margins are determined by a sensitivity analysis of each parameter. The CO_2 conversions obtained by these models show good agreement with the experimental data within the error margins, as shown in figures 4.2, 4.3 and 4.4. The thermal reaction pathways on CaO and Al_2O_3 have a similar apparent activation barrier, but the pre-exponential factor k_0 is 7 times higher on "CaO" respect to "Al_2O_3" only. The apparent reaction order in CO_2 is slightly lower on CaO respect to alumina (0.65 and 0.85 respectively), while the apparent orders for H_2 are similar and close to 1. In presence of plasma the apparent activation energy decreases from 120 to 95 kJ mol^{-1} with Al_2O_3 only and, more pronouncedly, from 140 to 75 kJ mol^{-1} when CaO is present. The order in CO_2 and the adsorption constant of H_2O do not change significantly when plasma is applied, while the orders in H_2 diminish strongly, in agreement with the experimental observation in figure 4.4 that the reactions are much less sensitive to the hydrogen concentration in the presence of plasma.

In principle, this model is just a mathematical description of the kinetics; nevertheless, we note that the fitting results in realistic values for activation barriers and reaction orders. More importantly, the model results in a good fit for both thermal as well as plasma experiments.

	Al_2O_3 0W	CaO 0W	Al_2O_3 1W	CaO + Al_2O_3 1W	CaO 1W
ln k_0 ($s^{-1}bar^{-(a+b)}$)	19.1 ± 1.2	21.0 ± 1.3	14.0 ± 1.0	13.0 ± 1.5	10.8 ± 2.1
E_a (kJ mol^{-1})	120 ± 5	140 ± 10	95 ± 5	75 ± 10	40 ± 20
a (order for CO_2)	0.85 ± 0.05	0.65 ± 0.05	0.6 ± 0.05	0.75 ± 0.05	0.9 ± 0.1
b (order for H_2)	0.95 ± 0.05	0.85 ± 0.05	-0.05 ± 0.05	0.25 ± 0.05	0.8 ± 0.2
ln K_{H2O}	8.5 ± 0.2	6.7 ± 0.3	6.5 ± 0.1	6.6 ± 0.2	6.5 ± 0.2

***Table 4.1**: Values of fitting parameters describing the RWGS rate equation for the five cases. The last column, CaO 1W represents the rate on CaO in plasma operation, obtained by subtraction of "Al_2O_3 1W" from "CaO + Al_2O_3 1W"; see text for further explanation.*

4.4.2 Synergy

The reaction rates in the three cases of "CaO" in thermal operation, "Al_2O_3" in plasma operation and "CaO + Al_2O_3" in plasma operation, are compared at fixed concentrations and temperature to assess synergy between CaO and plasma, which is the case if the enhancement factor, defined according equation 3, is larger than 1.

$$Enhancement = \frac{R_{\underset{plasma}{CaO\ and\ Al2O3}}}{R_{\underset{thermal}{CaO}} + R_{\underset{plasma}{Al2O3}}} \tag{4.3}$$

Both rates in presence of CaO and plasma ($R_{CaO\ and\ Al2O3\ plasma}$) as well as the rate in absence of CaO ($R_{Al2O3\ plasma}$) are measured directly and model equations are available (Table 4.1). The rate equation for the thermal activity of CaO is also available in Table 4.1, calculated by subtracting the rate over alumina ($R_{Al2O3\ thermal}$) from the rate measured over CaO and alumina ($R_{CaO\ and\ Al2O3\ thermal}$), as described above.

Figure 4.5 shows the reaction rates as function of temperature on “CaO” without plasma, “Al_2O_3 plasma” and “CaO + Al_2O_3 plasma” calculated at 0.2% CO_2, 10% H_2 and 0.1% H_2O, which is a condition experimentally studied. Figure 4.5 also shows that the enhancement factor decreases as function of temperature, showing synergy for temperatures up to 700°C and no synergy at 750°C.

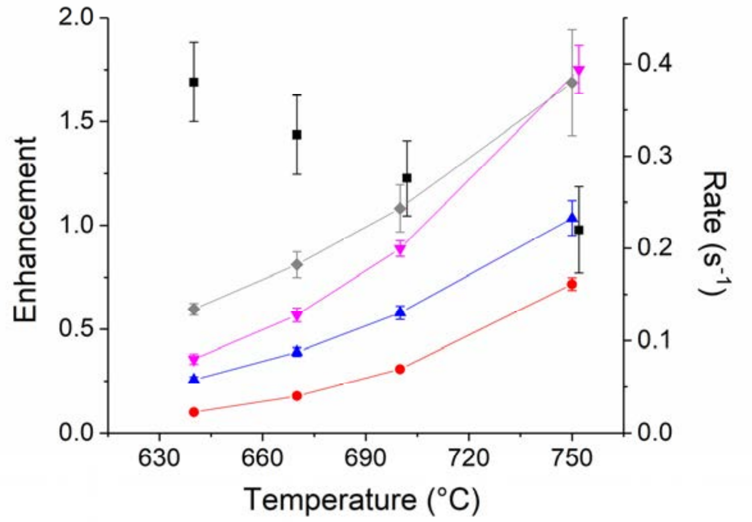

***Figure 4.5**: RWGS reaction rates as function of temperature on “CaO” in thermal operation (●), “Al_2O_3” in plasma operation (▲), sum of “CaO” in thermal and “Al_2O_3” in plasma operation (▼) and “CaO + Al_2O_3” in plasma operation (◆); enhancement factor (■); the concentrations are 10% H_2, 0.2% CO_2 and 0.1% H_2O in Ar, flow rate is 90ml min^{-1}.*

Figure 4.6 show the calculated RWGS rates according the model as function of CO_2, H_2 and H_2O concentrations at 640°C. Figure 4.6 suggests constant enhancement factor with varying concentration, as any trend is clearly smaller than the error margin. In all cases, synergy is observed at 640°C, in contrast to the similar figure at 750°C (Figure 4.7) showing synergy is absent for all concentrations considered.

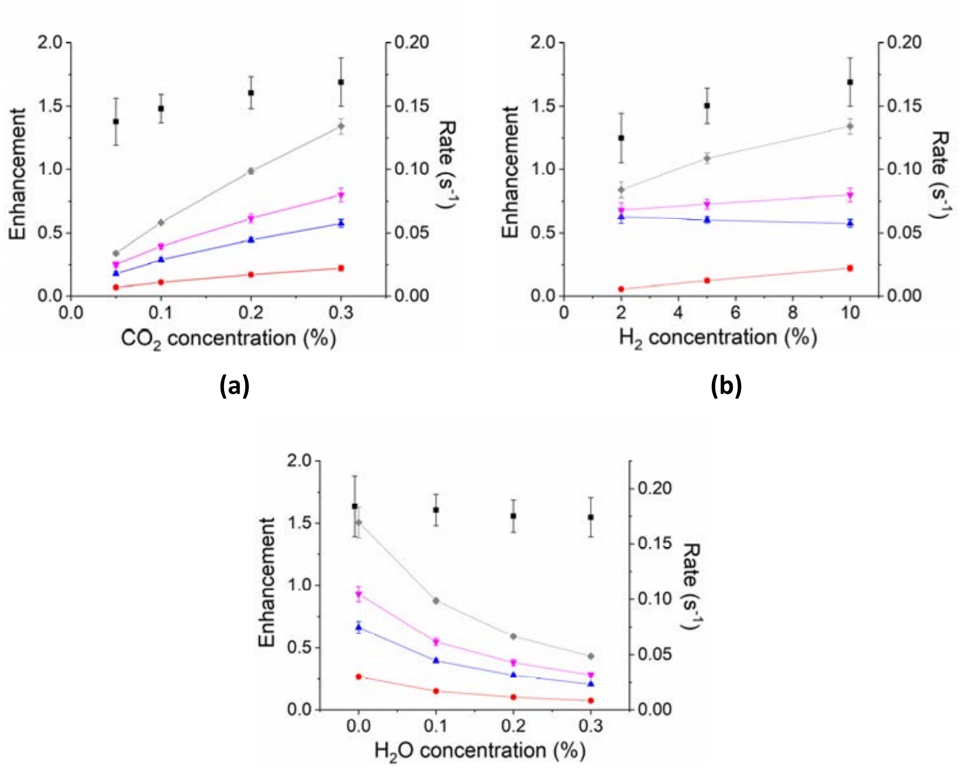

(a)

(b)

(c)

Figure 4.6: *RWGS reaction rates as function of concentration of CO_2* ***(a)****, H_2* ***(b)*** *and H_2O* ***(c)*** *on "CaO" in thermal operation (●), "Al_2O_3" in plasma operation (▲), sum of "CaO" thermal and "Al_2O_3" plasma operation (▼) and "CaO + Al_2O_3" in plasma operation (◆); enhancement factor (■); the fixed concentrations are 10% H_2, 0.2% CO_2 and 0.1% H_2O in Ar, temperature is 640°C, flow rate 90ml min^{-1}.*

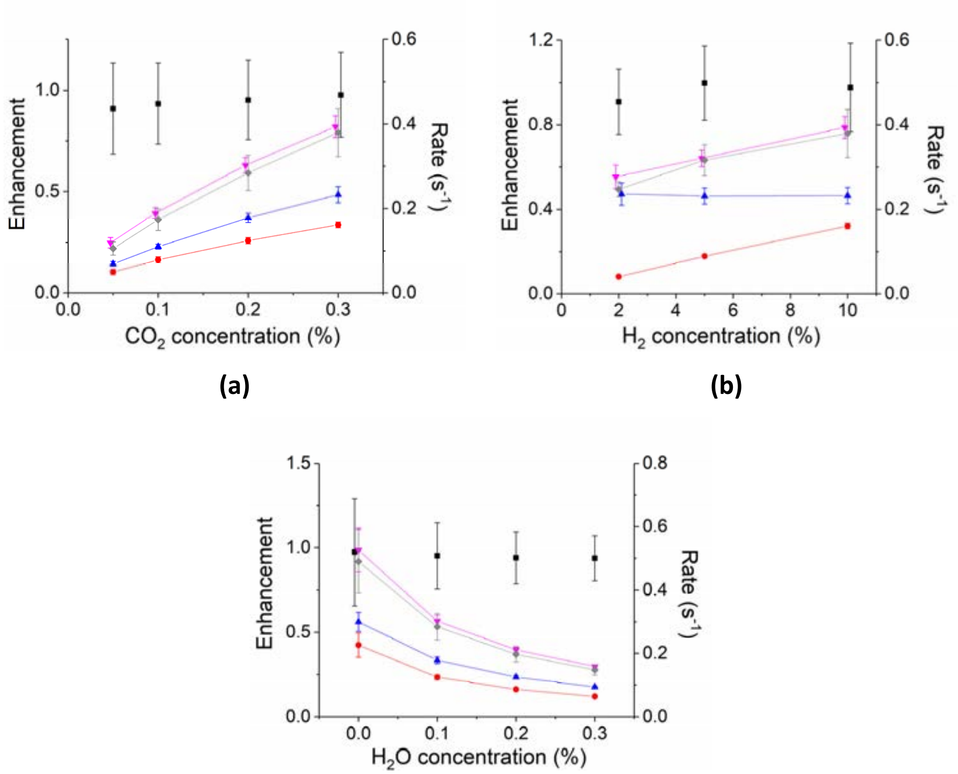

(a)

(b)

(c)

Figure 4.7*: RWGS reaction rates as function of concentration of CO_2* ***(a)****, H_2* ***(b)*** *and H_2O* ***(c)*** *on "CaO" in thermal operation (●), "Al_2O_3" in plasma operation (▲), sum of "CaO" thermal and "Al_2O_3" plasma operation (▼) and "CaO + Al_2O_3" in plasma operation (◆); enhancement factor (■); the fixed concentrations are 10% H_2, 0.2% CO_2 and 0.1% H_2O in Ar, temperature is 750°C, flow rate 90ml min^{-1}.*

4.4.3 General discussion: catalytic, plasma and plasma-catalytic effects

4.4.3.1 Catalytic effect

The catalytic activity per gram of CaO at 630°C is typically an order of magnitude lower than the activity of conventional Cu-based catalysts at the same conditions [60]. Clearly, CaO is not a preferred catalytic material, nevertheless it has significant activity, in line with the facts that MgO is also active for RWGS [58] and that CaO is active for WGS, as reported in a study on sorption enhanced WGS [61].

CaO and MgO [57] are much more active for RWGS than Al_2O_3 in thermal operation. Basic oxides adsorb CO_2 strongly [58, 59] and are more active, suggesting that the reaction proceeds via surface carbonates. The reaction order in CO_2 observed on CaO (0.65) suggests that the CaO surface is partly covered with carbonates. Apparently, surface carbonate species on CaO are active, whereas the surface of bulk $CaCO_3$ is not active at all for RWGS (Figure 4.3). Furthermore, the order in hydrogen is close to 1 on both CaO and Al_2O_3, indicating that activation of H_2 on the oxides surface is likely the rate determining step (r.d.s*.).* Alternatively, the coverage with hydrogen, presumably H atoms, is close to zero. The lack of activity of bulk $CaCO_3$, or possibly full coverage with surface carbonate, may be due to lacking ability for H_2 dissociation.

4.4.3.2 Plasma effect

Introduction of plasma on both Al_2O_3 and CaO enhances the RWGS reaction, at least partly due to plasma chemistry in the free space in the packed bed. Figure 4.8 presents a reaction scheme for plasma chemistry of CO_2 hydrogenation in DBD plasma, based on micro-kinetics at ambient conditions [62]. CO_2 dissociates to CO and O, similar to CO_2 dissociation as a consecutive reaction during $CaCO_3$ decomposition in an Ar plasma. The presence of H_2 opens a new reaction pathway for O-radicals to form water instead of O_2 or recombination with CO. The consecutive products in Figure 4.8, i.e. methane, ethane, methanol, formaldehyde, are not observed in our experiments since these reactions are thermodynamically less favored at high temperatures, above 600°C. Nevertheless, the contribution of plasma-chemistry in our experiments can be discussed based on the reaction scheme Figure 4.8, regarding activation of H_2 and CO_2.

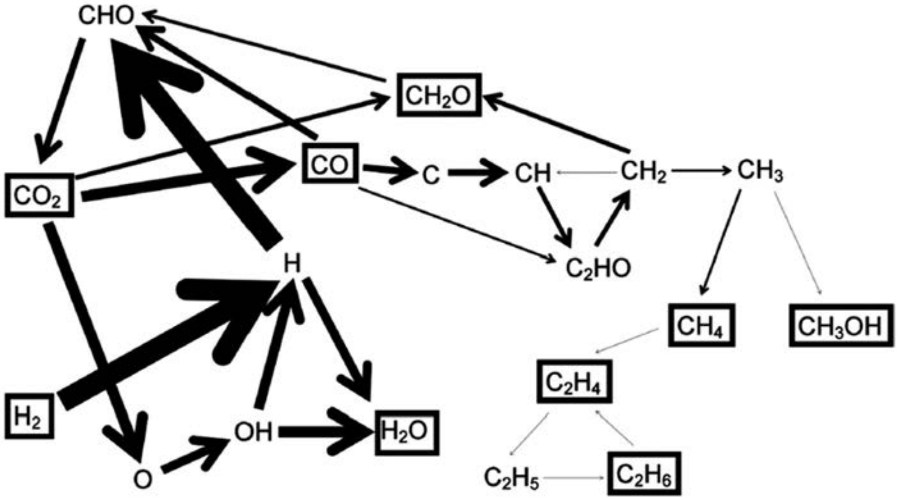

***Figure 4.8**: Dominant reaction pathways for the conversion of CO_2 and H_2 into various products, in a 50/50 CO_2/H_2 gas mixture. The thickness of the arrow lines is proportional to the rates of the net reactions. The stable molecules are indicated with black rectangles. Reproduced from [62].*

Introduction of plasma on Al_2O_3 also induces the order in hydrogen to decrease from 1 to 0, indicating that hydrogen activation is not the r.d.s. in the presence of plasma, suggesting that hydrogen is activated in the plasma rather than on the Al_2O_3 surface. Figure 4.8 also shows that RWGS is plasma initiated exclusively via CO_2 dissociation via electron impact dissociation or vibrational excitation whereas H radicals cannot activate CO_2. Instead, addition of hydrogen causes consecutive conversion of O-radicals to H_2O instead of O_2. Moreover, OH and CHO radicals generated in the presence of hydrogen rapidly react with CO and O respectively, forming back CO_2 and retarding the overall RWGS reaction. Although the conditions of the micro-kinetic study of figure 4.8 are different from our experiments, the reaction pathways in figure 4.8 agree with the observed zero order in hydrogen, suggesting that gas-phase plasma-chemistry is dominant over surface reactions on RWGS over alumina. Otherwise, the apparent order in H_2 would be higher than 0 and closer to the order 0.85 as observed on alumina (table 4.1). However, further clarification is not subject of this work as a blank experiment with plasma only, i.e. without alumina in an empty plasma reactor, is not included. This was even not attempted because the plasma is influenced by the presence of a packed bed and consequently the residence time, SEI and plasma properties cannot be kept constant, as discussed in the introduction. In fact, the plasma experiment with alumina is the blank experiment, which contains also the contribution of the reactor wall and the surface of the electrode, enabling a valid discussion on plasma-catalytic effects on CaO.

4.4.3.3 Synergy between CaO and plasma

Synergy between plasma and catalysis will be discussed quantitatively based on comparison of reaction rates at fixed conditions, using the kinetic description discussed above. Furthermore, complicating factors are addressed to the best of our ability, i.e. (i) any thermal effect of plasma, (ii) effect of the catalyst on the residence time in the reactor and (iii) the effect of the catalyst acting as a dielectric material on the plasma properties.

The term synergy is used with different meanings in papers on plasma catalytic CO_2 hydrogenation. In many cases, synergy is discussed based on changes in conversion when introducing the catalyst in the plasma [18, 22, 26, 27, 47-49], causing synergy if the combination of plasma and catalyst opens a new catalytic pathway, parallel to the plasma-chemistry pathway with plasma only and the catalytic pathway on the catalyst only. In some cases, synergy is claimed based on increasing selectivity to a specific product by introducing the catalyst in the plasma, e.g. formation of methane or methanol with Ni or Cu catalyst respectively. CO_2 conversion is not increased [25] or even decreased [46], indicating that the interaction of plasma and catalyst enhances consecutive reactions with CO as primary product. The results presented here involve one single reaction (RWGS) and quantification of synergy requires the kinetic description as discussed above. The facts that conversions are significant, and the results cannot be considered differential implies that synergy must be discussed based on reaction rates instead of conversions. Any further comparison with these studies is not useful, since the reaction conditions and catalysts are very different.

First, we will discuss possible artefacts as well as necessary assumptions considering the three complications described above.

i. Any effect of temperature changes induced by plasma is not only small but also have been corrected for as described in the result section. This has not been addressed explicitly in any work on plasma-catalytic CO_2 hydrogenation, except by Eliasson et al., estimating the temperature increase in the plasma by modelling heat transfer [25]. Other studies estimated the temperature by measuring either outside the reactor [22, 27, 46, 49] or inside the reactor downstream of the plasma zone [18, 26, 47].

ii. The residence time in all experiments was kept constant, as the total volume of the packed bed was constant. Note that the residence times in the packed bed and the plasma zone are identical. The same approach was used by others, comparing plasma catalytic- and plasma only- activities at constant residence time by including measurements with unloaded support [22, 26, 27, 46]. These studies used supported metal catalysts, introducing other complications as discussed below. In two studies [22, 46], the plasma zone was only partially filled, complicating the interpretation significantly because the plasma properties in the empty part of the reactor and inside the packed bed differ significantly.

iii. Changes in plasma properties can also be excluded based on three arguments. First, the Lissajous plots on “Al_2O_3” and “$CaO + Al_2O_3$” in plasma operation are very similar, as shown in figure A4.1, suggesting the same electron energy distribution as well as constant power [43, 56]. Second, alumina and calcium-oxide have similar dielectric constants, i.e. 9.2 and 11.8 respectively [63], and the size and shape of alumina and calcium-oxide particles are similar as well. Therefore, the number of contact points between particles in the bed, enhancing discharges in the plasma [19, 44, 45], is constant. It is well known that both dielectric constants and different particles size and shape changes the plasma properties significantly [6, 24], but with the precautions discussed above it is reasonable to assume that the plasma properties remain similar. Third, the catalyst contains oxides only and no metal particles, which are reported to intensify the plasma locally [44, 64].

Thus, the observed synergy is not caused by changing the plasma but can be attributed to a new catalytic pathway involving activated species in the plasma and the CaO surface. Apparently, the new pathway has a lower activation barrier, as the observed apparent activation energy decreases from 140 to 40 kJ mol^{-1} when plasma is introduced. The plasma-catalytic pathway is dominant at 640°C, while at 750°C the thermal catalytic pathway dominates, because of the high activation barrier, so that no synergy is observed as shown in figure 4.5. Note that the decrease in the enhancement factor with increasing temperature shown in figure 4.5 is not caused by approaching thermodynamic equilibrium, since all rates in figure 4.5 are calculated at fixed concentrations far away from thermodynamic equilibrium [51].

The apparent order for hydrogen of 0.8 on CaO in plasma operation suggests that hydrogen activation in the plasma is involved in the plasma-catalytic pathway. Presumably hydrogen radicals react with surface carbonates on calcium oxide, in contrast to carbonates on alumina since order in hydrogen is zero. Remarkably, activation of CO_2 via hydrogen radicals is not significant in the case of plasma chemistry as discussed above.

These results will be used in Chapter 5 describing decomposition of $CaCO_3$ in a H_2 containing plasma. We believe that the proposed method allows separation of, at one hand, the influence of surface catalytic reactions on the conversion, versus the influence of the fixed bed as a dielectric material on plasma chemistry in a DBD-plasma catalytic reactor. This may contribute to improved insight in plasma catalysis. Further progress could be anticipated via developing in-situ of preferably operando characterization techniques to study adsorbed species. Attempt with FT-IR failed so far mainly because of the high temperature of operation, but this would certainly the way forward to make progress, in combination with reliable kinetic information.

4.5 Conclusions

Synergy between plasma and calcium oxide for RWGS has been quantified, by minimizing any effect of the presence of the catalyst fixed bed as a dielectric material on the contribution of plasma chemistry, i.e. chemical conversion in the plasma, keeping also the specific energy input and the residence time constant. Moreover, synergy is determined by calculating reaction rates at fixed temperature and gases concentrations, by using kinetic equations describing well the integral experiments performed in presence and absence of both calcium oxide and plasma.

Synergy is observed at low operational temperature (640°C) with a rate-enhancement factor of 1.7. The rate enhancement steadily decreases with increasing temperature until synergy disappears at 750°C, independently of the composition of the gas mixture. Synergy is caused by opening a new reaction pathway involving plasma activated species on the CaO surface. The apparent activation barrier of the plasma-catalytic pathway is 40 kJ mol^{-1}, much lower than the apparent activation barriers of thermal-catalytic reaction (140 kJ mol^{-1}) and of the pathway with Al_2O_3 and plasma (90 kJ mol^{-1}). The apparent orders for CO_2 and H_2 are 0.9 and 0.8 respectively, suggesting that the rate-determining step is the reaction of surface $CaCO_3$ with a plasma-activated H_2, presumably H radicals.

References

[1] E. C. Neyts, and A. Bogaerts. Understanding Plasma Catalysis through Modelling and Simulation - A Review. *Journal of Physics D: Applied Physics* **2014**, 47, 22.

[2] E. C. Neyts, K. Ostrikov, M. K. Sunkara, and A. Bogaerts. Plasma Catalysis: Synergistic Effects at the Nanoscale. *Chemical Reviews* **2015**, 115, 24, 13408–13446.

[3] J. C. Whitehead. Plasma-Catalysis: The Known Knowns, the Known Unknowns and the Unknown Unknowns. *Journal of Physics D: Applied Physics* **2016**, 49, 24, 243001.

[4] A. Bogaerts, T. Kozák, K. van Laer, and R. Snoeckx. Plasma-Based Conversion of CO_2: Current Status and Future Challenges. *Faraday Discussions* **2015**, 183, 217–232.

[5] B. Ashford, and X. Tu. Non-Thermal Plasma Technology for the Conversion of CO_2. *Current Opinion in Green and Sustainable Chemistry* **2017**, 3, 45–49.

[6] I. Michielsen, Y. Uytdenhouwen, J. Pype, B. Michielsen, J. Mertens, F. Reniers, V. Meynen, and A. Bogaerts. CO_2 Dissociation in a Packed Bed DBD Reactor: First Steps towards a Better Understanding of Plasma Catalysis. *Chemical Engineering Journal* **2017**, 326, 477–488.

[7] T. Silva, M. Grofulović, B. L. M. Klarenaar, A. S. Morillo-Candas, O. Guaitella, R. Engeln, C. D. Pintassilgo and V. Guerra. Kinetic Study of Low-Temperature CO_2 Plasmas under Non-Equilibrium Conditions. I. Relaxation of Vibrational Energy. *Plasma Sources Science and Technology* **2018**, 27, 1.

[8] M. Liu, Y. Yi, L. Wang, H. Guo, and A. Bogaerts. Hydrogenation of Carbon Dioxide to Value-Added Chemicals by Heterogeneous Catalysis and Plasma Catalysis. *Catalysts* **2019**, 9, 3, 275.

[9] M. G. Sobacchi, A. V. Saveliev, A. A. Fridman, L. A. Kennedy, S. Ahmed, and T. Krause. Experimental Assessment of a Combined Plasma/Catalytic System for Hydrogen Production via Partial Oxidation of Hydrocarbon Fuels. *International Journal of Hydrogen Energy* **2002**, 27, 6, 635–642.

[10] X. Tu, and J. C. Whitehead. Plasma-Catalytic Dry Reforming of Methane in an Atmospheric Dielectric Barrier Discharge: Understanding the Synergistic Effect at Low Temperature. *Applied Catalysis B: Environmental* **2012**, 125, 439–448.

[11] T. Nozaki, and K. Okazaki. Non-Thermal Plasma Catalysis of Methane: Principles, Energy Efficiency, and Applications. *Catalysis Today* **2013**, 211, 29–38.

[12] J. Hong, S. Prawer, and A. B. Murphy. Plasma Catalysis as an Alternative Route for Ammonia Production: Status, Mechanisms, and Prospects for Progress. *ACS Sustainable Chemistry and Engineering* **2018**, 6, 1, 15–31.

[13] H. H. Kim, Y. Teramoto, A. Ogata, H. Takagi, and T. Nanba. Atmospheric-Pressure Nonthermal Plasma Synthesis of Ammonia over Ruthenium Catalysts. *Plasma Processes and Polymers* **2017**, 14, 6, 1–9.

[14] A. Fridman. Plasma Chemistry. *Cambridge: Cambridge University Press* 2008.

[15] C. Tendero, C. Tixier, P. Tristant, J. Desmaison, and P. Leprince. Atmospheric Pressure Plasmas: A Review. *Spectrochimica Acta - Part B Atomic Spectroscopy* **2006**, 61, 1, 2–30.

[16] H. H. Kim, Y. Teramoto, N. Negishi, and A. Ogata. A Multidisciplinary Approach to Understand the Interactions of Nonthermal Plasma and Catalyst: A Review. *Catalysis Today* **2015**, 256, 1, 13–22.

[17] D. Mei, X. Zhu, Y. L. He, J. D. Yan, and X. Tu. Plasma-Assisted Conversion of CO_2 in a Dielectric Barrier Discharge Reactor: Understanding the Effect of Packing Materials. *Plasma Sources Science and Technology* **2015**, 24, 1.

[18] M. Nizio, A. Albarazi, S. Cavadias, J. Amouroux, M. E. Galvez, and P. da Costa. Hybrid Plasma-Catalytic Methanation of CO_2 at Low Temperature over Ceria Zirconia Supported Ni Catalysts. *International Journal of Hydrogen Energy* **2016**, 41, 27, 11584–11592.

[19] K. van Laer, and A. Bogaerts. Improving the Conversion and Energy Efficiency of Carbon Dioxide Splitting in a Zirconia-Packed Dielectric Barrier Discharge Reactor. *Energy Technology* **2015**, 3, 10 1038–1044.

[20] F. Brehmer, S. Welzel, M. C. M. van de Sanden, and R. Engeln. CO and Byproduct Formation during CO_2 Reduction in Dielectric Barrier Discharges. *Journal of Applied Physics* **2014**, 116, 12.

[21] M. Ramakers, I. Michielsen, R. Aerts, V. Meynen, and A. Bogaerts. Effect of Argon or Helium on the CO_2 Conversion in a Dielectric Barrier Discharge. *Plasma Processes and Polymers* **2015**, 12, 8, 755–763.

[22] Y. Zeng, and X. Tu. Plasma-Catalytic Hydrogenation of CO_2 for the Cogeneration of CO and CH_4 in a Dielectric Barrier Discharge Reactor: Effect of Argon Addition. *Journal of Physics D: Applied Physics* **2017**, 50, 18.

[23] Y. Uytdenhouwen, S. van Alphen, I. Michielsen, V. Meynen, P. Cool, and A. Bogaerts. A Packed-Bed DBD Micro Plasma Reactor for CO_2 dissociation: Does Size Matter? *Chemical Engineering Journal* **2018**, 348, 557–568.

[24] T. Butterworth, R. Elder, and R. Allen. Effects of Particle Size on CO_2 reduction and Discharge Characteristics in a Packed Bed Plasma Reactor. *Chemical Engineering Journal* **2016**, 293, 55–67.

[25] B. Eliasson, U. Kogelschatz, B. Xue, and L. M. Zhou. Hydrogenation of Carbon Dioxide to Methanol with a Discharge-Activated Catalyst. *Industrial and Engineering Chemistry Research* **1998**, 37, 8, 3350–3357.

[26] E. Jwa, S. B. Lee, H. W. Lee, and Y. S. Mok. Plasma-Assisted Catalytic Methanation of CO and CO_2 over Ni-Zeolite Catalysts. *Fuel Processing Technology* **2013**, 108, 89–93.

[27] X. Zhu, J. H. Liu, X. S. Li, J. L. Liu, X. Qu, and A. M. Zhu. Enhanced Effect of Plasma on Catalytic Reduction of CO_2 to CO with Hydrogen over Au/CeO_2 at Low Temperature. *Journal of Energy Chemistry* **2017**, 26, 3, 488–493.

[28] W. C. Chung, and M. B. Chang. Review of Catalysis and Plasma Performance on Dry Reforming of CH_4 and Possible Synergistic Effects. *Renewable and Sustainable Energy Reviews* **2016**, 62, 13–31.

[29] S. Kameshima, K. Tamura, Y. Ishibashi, and T. Nozaki. Pulsed Dry Methane Reforming in Plasma-Enhanced Catalytic Reaction. *Catalysis Today* **2015**, 256, 1, 67–75.

[30] S. Kameshima, K. Tamura, R. Mizukami, T. Yamazaki, and T. Nozaki. Parametric Analysis of Plasma-Assisted Pulsed Dry Methane Reforming over Ni/Al_2O_3 catalyst. *Plasma Processes and Polymers* **2017**, 14, 6, 1–7.

[31] A. Ozkan, T. Dufour, G. Arnoult, P. De Keyzer, A. Bogaerts, and F. Reniers. CO_2-CH_4 conversion and Syngas Formation at Atmospheric Pressure Using a Multi-Electrode Dielectric Barrier Discharge. *Journal of CO_2 Utilization* **2015**, 9, 78–81.

[32] X. Tu, H. J. Gallon, M. V. Twigg, P. A. Gorry, and J. C. Whitehead. Dry Reforming of Methane over a Ni/Al_2O_3 catalyst in a Coaxial Dielectric Barrier Discharge Reactor. *Journal of Physics D: Applied Physics* **2011**, 44, 27.

[33] H. J. Gallon, X. Tu, and J. C. Whitehead. Effects of Reactor Packing Materials on H_2 production by CO_2 reforming of CH_4 in a Dielectric Barrier Discharge. *Plasma Processes and Polymers* **2012**, 9, 1, 90–97.

[34] Y. Zeng, X. Zhu, D. Mei, B. Ashford, and X. Tu. Plasma-Catalytic Dry Reforming of Methane over γ-Al_2O_3 supported Metal Catalysts. *Catalysis Today* **2015**, 256, 1, 80–87.

[35] X. Zheng, S. Tan, L. Dong, S. Li, and H. Chen. Silica-Coated $LaNiO_3$ Nanoparticles for Non-Thermal Plasma Assisted Dry Reforming of Methane: Experimental and Kinetic Studies. *Chemical Engineering Journal* **2015**, 265, 1, 147–156.

[36] T. Kozàk, and A. Bogaerts. Splitting of CO_2 by Vibrational Excitation in Non-Equilibrium Plasmas: A Reaction Kinetics Model. *Plasma Sources Science and Technology* **2014**, 23, 4.

[37] R. Aerts, T. Martens, and A. Bogaerts. “Influence of Vibrational States on CO_2 Splitting by Dielectric Barrier Discharges.” *Journal of Physical Chemistry C* **2012**, 116, 44, 23257–23273.

[38] A. Bogaerts, W. Wang, A. Berthelot, and V. Guerra. Modeling Plasma-Based CO_2 Conversion: Crucial Role of the Dissociation Cross Section. *Plasma Sources Science and Technology* **2016**, 25, 5.

[39] L. D. Pietanza, G. Colonna, G. D’Ammando, and M. Capitelli. Time-Dependent Coupling of Electron Energy Distribution Function, Vibrational Kinetics of the Asymmetric Mode of CO_2 and Dissociation, Ionization and Electronic Excitation Kinetics under Discharge and Post-Discharge Conditions. *Plasma Physics and Controlled Fusion* **2017**, 59, 1.

[40] G. J. van Rooij, D. C. M. van den Bekerom, N. den Harder, T. Minea, G. Berden, W. A. Bongers, R. Engeln, M. F. Graswinckel, E. Zoethout, and M. C. M. van de

Sanden. Taming Microwave Plasma to Beat Thermodynamics in CO_2 Dissociation. *Faraday Discussions* **2015**, 183, 233–248.

[41] W. Bongers, H. Bouwmeester, B. Wolf, F. Peeters, S. Welzel, D. van den Bekerom, N. den Harder, A. Goede, M. Graswinckel, P. W. Groen, J. Kopecki, M. Leins, G. J. van Rooij, A. Schulz, M. Walker, M. C. M. van de Sanden Plasma-Driven Dissociation of CO_2 for Fuel Synthesis. *Plasma Processes and Polymers* **2017**, 14, 6, 1–8.

[42] T. Minea, D. C. M. van den Bekerom, F. J. J. Peeters, E. Zoethout, M. F. Graswinckel, M. C. M. van de Sanden, T. Cents, L. Lefferts, and G. J. van Rooij. Non-Oxidative Methane Coupling to C_2 hydrocarbons in a Microwave Plasma Reactor. *Plasma Processes and Polymers* **2018**, 1–16.

[43] T. Butterworth, and R. W. K. Allen. Plasma-Catalyst Interaction Studied in a Single Pellet DBD Reactor: Dielectric Constant Effect on Plasma Dynamics. *Plasma Sources Science and Technology* **2017**, 26, 6.

[44] J. Kruszelnicki, K. W. Engeling, J. E. Foster, Z. Xiong, and M. J. Kushner. Propagation of Negative Electrical Discharges through 2-Dimensional Packed Bed Reactors. *Journal of Physics D: Applied Physics* **2017**, 50, 2.

[45] Z. Mujahid, and A. Hala. Plasma Dynamics in a Packed Bed Dielectric Barrier Discharge (DBD) Operated in Helium. *Journal of Physics D: Applied Physics* **2018**, 51, 11, 11LT02.

[46] F. Azzolina-Jury. Novel Boehmite Transformation into γ-Alumina and Preparation of Efficient Nickel Base Alumina Porous Extrudates for Plasma-Assisted CO_2 Methanation. *Journal of Industrial and Engineering Chemistry* **2019**, 71, 410–424.

[47] M. C. Bacariza, M. Biset-Peiró, I. Graça, J. Guilera, J. Morante, J. M. Lopes, T. Andreu, and C. Henriques. DBD Plasma-Assisted CO_2 Methanation Using Zeolite-Based Catalysts: Structure Composition-Reactivity Approach and Effect of Ce as Promoter. *Journal of CO_2 Utilization* **2018**, 26, 202–211.

[48] C. J. Lee, D. H. Lee, and T. Kim. Enhancement of Methanation of Carbon Dioxide Using Dielectric Barrier Discharge on a Ruthenium Catalyst at Atmospheric Conditions. *Catalysis Today* **2017**, 293–294, 97–104.

[49] L. Wang, Y. Yi, H. Guo, and X. Tu. Atmospheric Pressure and Room Temperature Synthesis of Methanol through Plasma-Catalytic Hydrogenation of CO_2. *ACS Catalysis* **2018**, 8, 1, 90–100.

[50] J. Blamey, E. J. Anthony, J. Wang, and P. S. Fennell. The Calcium Looping Cycle for Large-Scale CO_2 capture. *Progress in Energy and Combustion Science* **2010**, 36, 2, 260–279.

[51] B. J. McBride, M. J. Zehe, and S. Gordon. NASA Glenn Coefficients for Calculating Thermodynamic Properties of Individual Species **2002**.

https://www.grc.nasa.gov/WWW/CEAWeb/TP-2002-21556.htm

[52] P. S. Fennell, R. Pacciani, J. S. Dennis, J. F. Davidson, and A. N. Hayhurst. The Effects of Repeated Cycles of Calcination and Carbonation on a Variety of Different Limestones, as Measured in a Hot Fluidized Bed of Sand. *Energy and Fuels* **2007**, 21, 4, 2072–2081.

[53] A. I. Lysikov, A. N. Salanov, and A. G. Okunev. Change of CO_2 Carrying Capacity of CaO in Isothermal Recarbonation-Decomposition Cycles. *Industrial and Engineering Chemistry Research* **2007**, 46, 13, 4633–4638.

[54] R. H. Borgwardt. Sintering of Nascent Calcium Oxide. *Chemical Engineering Science* **1989**, 44, 1, 53–60.

[55] A. Reller, C. Padeste, and P. Hug. Formation of organic compounds from metal carbonates. *Nature* **1987**, 329, 8, 527-529.

[56] F. J. J. Peeters, and M. C. M. van de Sanden. The Influence of Partial Surface Discharging on the Electrical Characterization of DBDs. *Plasma Sources Science and Technology* **2015**, 24, 1, 15016.

[57] G. Baldauf-Sommerbauer, S. Lux, W. Aniser, and M. Siebenhofer. Reductive Calcination of Mineral Magnesite: Hydrogenation of Carbon Dioxide without Catalysts. *Chemical Engineering and Technology* **2016**, 39, 11, 2035–2041.

[58] B. H. Solis, Y. Cui, X. Weng, J. Seifert, S. Schauermann, J. Sauer, S. Shaikhutdinov, and H. J. Freund. Initial Stages of CO_2 Adsorption on CaO: A Combined Experimental and Computational Study. *Physical Chemistry Chemical Physics* **2017**, 19, 6, 4231–4242.

[59] M. Casarin, D. Falcomer, A. Glisenti, and A. Vittadini. Experimental and Theoretical Study of the Interaction of CO_2 with α-Al_2O_3. *Inorganic Chemistry* **2003**, 42, 2, 436–445.

[60] M. Lortie, R. Isaifan, Y. Liu, and S. Mommers. Synthesis of CuNi/C and CuNi/γ-Al catalysts for the Reverse Water Gas Shift Reaction. *International Journal of Chemical Engineering* **2015**.

[61] Z. Li, Y. Liu, and N. Cai. Effect of CaO Hydration and Carbonation on the Hydrogen Production from Sorption Enhanced Water Gas Shift Reaction. *International Journal of Hydrogen Energy* **2012**, 37, 15, 11227–11236.

[62] C. de Bie, J. van Dijk, and A. Bogaerts. CO_2 Hydrogenation in a Dielectric Barrier Discharge Plasma Revealed. *Journal of Physical Chemistry C* **2016**, 120, 44, 25210–25224.

[63] Landolt-Börnstein - Group III Condensed Matter. *Springer* **2012**.

[64] H. H. Kim, J. H. Kim, and A. Ogata. Microscopic Observation of Discharge Plasma on the Surface of Zeolites Supported Metal Nanoparticles. *Journal of Physics D: Applied Physics* **2009**, 42, 13.

Chapter 5

Calcium Carbonate Decomposition in a Dielectric Barrier Discharge Hydrogen Plasma

Summary

In Chapter 5 we investigate the effects of hydrogen on the decomposition of the carbonate in thermal operation and in Dielectric Barrier Discharge (DBD) plasma, by means of a comparative method developed to distinguish between thermal and chemical effects of plasma based on reaction rates. 10% hydrogen induces 1) an increase in the reaction rate up to 3 times during isothermal reactions at 590°C and 2) formation of CO via Reverse Water Gas Shift (RWGS), catalysed by the presence of the product calcium oxide. The increase in the reaction rate is caused by catalytic effect of H_2O, produced via RWGS alongside CO. The presence of plasma enhances both the decomposition rate and CO formation, the former via a purely thermal effect, the latter via the synergetic effect for RWGS between plasma and calcium oxide.

5.1 Introduction

Global warming caused by emission of greenhouse gases (GHGs) is a major issue both environmentally and economically. Carbon-dioxide, the most important among GHGs, reached an average concentration of more than 0.04%, increasing the global temperature of ca. 1°C above the pre-industrial level [1]. In order to prevent an increase of more than 2°C in the next decades as stated by the Paris Agreement [2], a large implementation of Carbon Capture and Storage (CCS) or Utilization (CCU) as well as low-carbon emission technologies is needed [3].

CCS refers to a group of technologies developed to capture and store CO_2 from combustion in flue gasses of power plants. The most developed option to capture CO_2 is flue gas scrubbing using amine-based sorbents, e.g. monoethanolamide [4, 5]. However, the interaction of these sorbents with sulphur dioxide and oxygen, always present in flue gas, as well as its corrosive nature represent major issues for practical operation. A possible alternative is mineral carbonation of rocks as serpentine $Mg_3Si_2O_5(OH)_4$ or calcium oxide, requiring rather high temperatures [6]. The carbonation (for capture) and calcination (for recycling) of calcium oxide, referred as Calcium Looping Cycle, is widely discussed in literature [7].

However, the calcination reaction requires high temperatures in order to achieve high CO_2 concentrations in the outlet, i.e. at least 950°C to obtain pure CO_2 at atmospheric pressure [8]. Such temperatures result in sintering, decreasing the CO_2 capture capacity when calcium oxide is recycled [9-12]. The impact of cycling on the calcium oxide microstructure has been widely studied and substantial decrease of the surface area as well as closure of meso- and micro- pores were reported [11, 12]. Different synthesis methods and precursors as well as addition of oxides as support material, mixing with other elements, doping, core-shell materials and nano-structured composites were explored in order to improve thermal stability of calcium oxide [13].

Catalysis has been also explored in order to reduce the decomposition temperature. The catalytic effect of low concentrations of water on $CaCO_3$ decomposition has been demonstrated and quantified in Chapter 2 of this thesis. Water catalyses the decomposition by increasing the reaction rate 3 to 5 times, allowing to reduce the decomposition temperature of ca. 60-70°C. Reller et al. observed that also hydrogen enhances decomposition [14], resulting in a decrease of 100°C in the decomposition temperature and a substantial production of CO and H_2O along with CO_2.

Another approach would be to induce decomposition at lower temperatures by using a non-thermal plasma [15]. DBD plasma is frequently used for studying plasma catalytic conversion at low temperatures [16, 17]. The high AC voltages applied at relatively low frequency (50 to 10^5 Hz) produces a non-equilibrium plasma with very high electron temperatures (1–10 eV equal to 10^4–10^5 K), high vibrational temperatures (10^3 K), and rather low rotational and translational temperatures in the plasma zone, typically in the order of 100 K [18, 19]. The low gas temperature allows the application of a solid directly in the plasma generation zone without fast sintering, maximizing the interaction between active species and the solid phase. Furthermore, DBD plasma can be generated at atmospheric pressure, which is interesting from the application point of view. Very promising results were presented in the last years on plasma catalysis, e.g. for CO_2 conversion [20-22], CH_4 reforming [23-25] and coupling [26], and N_2 fixation [27] in terms of high conversion and selectivity.

The effects of DBD plasma on the decomposition of a solid, e.g. $CaCO_3$, are still unknown. Plasma generated from an inert gas won't likely convert $CaCO_3$, while a more reactive plasma, e.g. hydrogen plasma, might interact with $CaCO_3$ enabling its conversion.

In Chapter 3 of this thesis we demonstrated that argon plasma has only a thermal effect on $CaCO_3$ decomposition, i.e. increase in the gas temperature, beside a consecutive CO_2 dissociation to CO and O_2. We used a comparative method which allows to distinguish between thermal effect and chemical effects of plasma on the decomposition kinetics. Assuming plasma cannot penetrate the pores with diameter of less than 3 µm, based on the Paschen's Law [28, 29], the thermal surface processes proceed on both internal and external surface, while plasma processes proceed only on the external surface. Varying both the internal and external surface area, i.e. via particles size in a packed bed plasma reactor, allows to discern what the dominant interaction is, thermal or plasma chemistry.

In the current Chapter, we investigate the effect of hydrogen and hydrogen plasma on $CaCO_3$ decomposition. The production of CO and H_2O during thermal $CaCO_3$ decomposition observed by Reller suggests a substantial contribution of RWGS on the overall reaction. The Reverse Water Gas Shift reaction (RWGS) is catalysed by calcium oxide in both thermal and plasma operations, with a significant synergy between plasma and calcium oxide at 630°C, as resulted from the kinetic study on RWGS performed in Chapter 4. On the other hand, $CaCO_3$ is not active at all for RWGS.

Therefore, calcium carbonate decomposition in presence of hydrogen likely proceeds as shown in scheme 5.1, where the RWGS (R_3 in scheme 5.1) is enhanced when calcium oxide and plasma are present. On the other hand, we question whether CO can be produced directly from the decomposition of bulk calcium carbonate without involving the formation of CO_2 (R_2 in scheme 1). Alumina and gas phase plasma chemistry contributes for RWGS to lesser extent but still significantly, thus R_3 cannot be neglected in both operations.

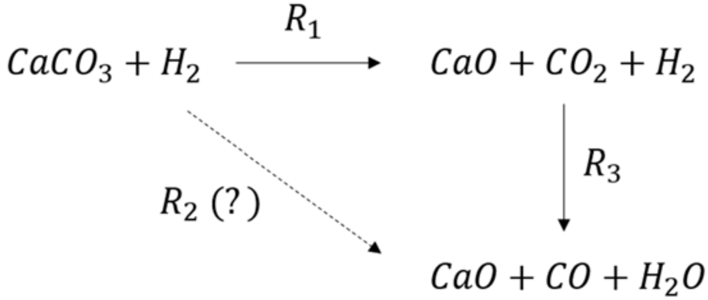

Scheme 5.1*: Reaction scheme of $CaCO_3$ decomposition in presence of H_2.*

The goal of Chapter 5 is to assess the effect of hydrogen on $CaCO_3$ decomposition in both thermal and plasma operation. We will analyse the effects of hydrogen and hydrogen plasma on the kinetics of $CaCO_3$ decomposition and CO production, distinguishing between thermal and chemical effects of plasma by using the method developed in Chapter 3, as described above.

5.2 Materials and methods

5.2.1 Reactor setup

Figure 5.1 shows a schematic representation of the equipment used to measure $CaCO_3$ decomposition in presence of hydrogen plasma. The fixed bed reactor is fed with a mix of Ar, CO_2 and H_2. The temperature of the oven is controlled with a Eurotherm controller with an accuracy of ±0.5°C between room temperature and 1000°C. The isothermal zone is 8 cm long at 900°C, defined as the part of the reactor with less than ± 1°C temperature variation. A Quadrupole Mass Spectrometer (MS) measures the composition of the gas mixture leaving the reactor. The MS signal for CO_2 (44 m/e) and CO (28 m/e) are calibrated between 0.16% and 5% CO_2 and at 5% CO, resulting in a linear relationship. The reactor is a 4 mm inner- and 6 mm outer- diameter quartz tube. The inner electrode is a stainless-steel rod of 1 mm diameter placed co-axially in the center of the reactor section by the help of a spacer, which is removed when the rod and the packed bed are positioned. The outer electrode is a 1 cm long stainless-steel tube with 6 mm inner diameter, enclosing a plasma zone of 0.035 cm^3 in volume. The plasma zone was filled completely with 10 mg $CaCO_3$ and 95 mg α-Al_2O_3. An AC voltage of up to 5 kV peak to peak is applied to the inner electrode with a frequency of 23.5 kHz using a PMV 500-4000 power supply, while the outer electrode is connected to the ground via a probe capacitor of capacity 4 nF. The power of the plasma is calculated using the Lissajous method by measuring the voltage on the inner electrode with a Tektronix P6015A high voltage probe and on the outer electrode with a TT – HV 250 voltage probe as described in literature [30].

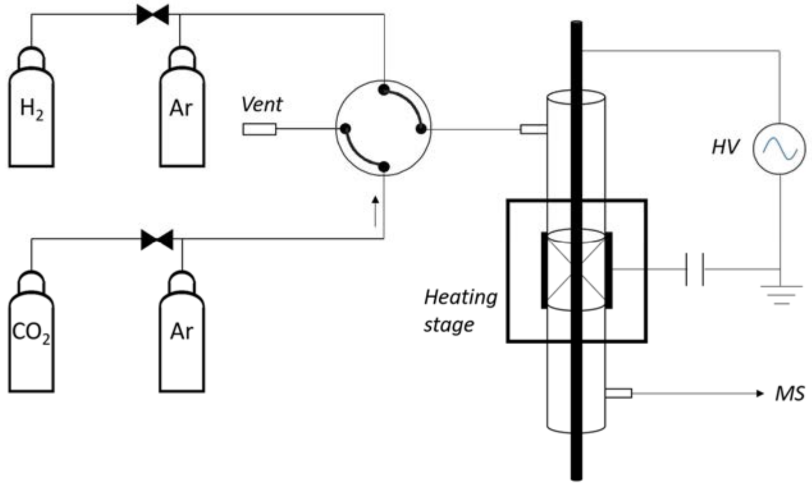

Figure 5.1: *Plasma reactor setup used for this study.*

5.2.2 $CaCO_3$ decomposition in presence of H_2 in thermal and plasma operations

Four $CaCO_3$ samples with different surface area and particles size, named “Sample A-D”, were synthesized for the decomposition experiments from three different precursors: calcium D-gluconate-monohydrate (99%, Alfa Aesar, Haverhill, MA, USA) for Sample A, calcium L-ascorbate-di-hydrate (99%, Sigma-Aldrich, St. Louis, MO, USA) for sample B, and calcium carbonate (99%, Sigma-Aldrich, St. Louis, MO, USA) for samples C and D. The synthesis and characterization are explained in detail in Chapter 3, while table 5.1 summarizes the samples properties. Samples composed of 10 mg of $CaCO_3$ and 95 mg Al_2O_3 are placed in the reactor. The procedure and the conditions differ between experiments and will be explained in the results section.

Code	**$CaCO_3$ S. S. A. ($m^2\ g^{-1}$)**	**Particles diameter (µm)**
A	1.7 ± 0.1	250-300
B	0.8 ± 0.1	250-300
C	< 0.5	250-300
D	< 0.5	100-125

Table 5.1. *Characteristics of the four $CaCO_3$ samples used.*

5.3 Results

5.3.1 Decomposition in thermal operation

Figure 5.2 shows the result of the decomposition of sample C without plasma, in terms of concentration of the gases at the reactor outlet as function of time. The experiment is initiated at 590°C by switching the feed composition from 5% CO_2 to 10% H_2 in Ar, which is maintained until the end of the experiment. Every 4 minutes the temperature is increased by 20°C with a heating rate of 20°C min^{-1}. The rate of the decomposition reaction is linear with the sum of CO_2 and CO concentrations, since no other carbonaceous products are observed. The reaction is in a quasi-steady state for the first 18 minutes, after that exhaustion of $CaCO_3$ takes place. After 14 minutes of reaction, although the overall rate is still steady, the CO_2 concentration steadily decreases while CO increases, causing a change in the ratio between CO_2 and CO production rates.

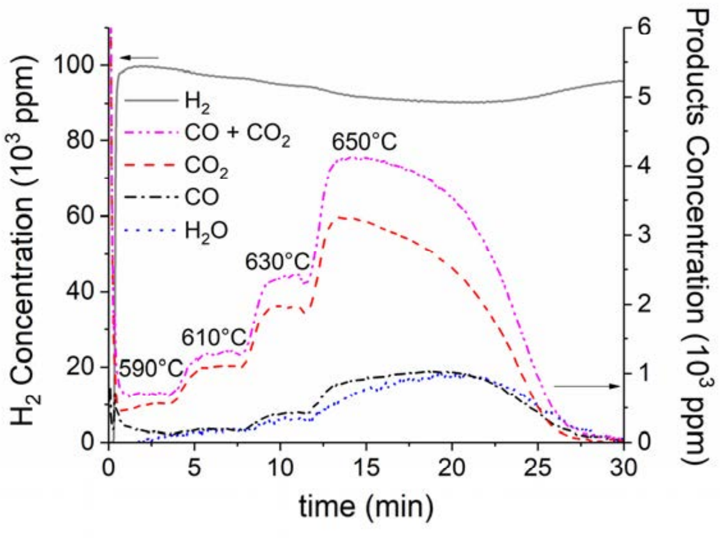

***Figure 5.2**: Concentrations of the gases at the outlet during 10mg $CaCO_3$ (sample C) decomposition as function of time. Flow rate is 30 ml min^{-1}, feed composition is 10% H_2 in Ar, temperature changes every few minutes.*

5.3.2 Decomposition in plasma operation

Figure 5.3 shows the effect of hydrogen and plasma on the decomposition of Sample C. The experiment is initiated in thermal operation (without plasma) at 630°C by shifting the feed composition from 5% CO_2 in Ar to pure Ar. The applied temperature is kept constant throughout the experiment. After 1 minute of decomposition, 10% H_2 is introduced still in thermal operation. After 2 minutes from the beginning of the experiment, plasma is turned on and kept at a power of 1.5 W until the end of experiment.

The introduction of 10% hydrogen in argon during $CaCO_3$ decomposition at 630°C causes an increase in the CO_2 emission rate and formation of CO and H_2O. The decomposition rate increases by a factor of ca. 2 when hydrogen is introduced. The reaction observed between minutes 1 and 2 is qualitatively the same of what observed in figure 5.2 between minutes 8 and 12, although a quantitative comparison is not possible since the flow rates are different. The introduction of plasma causes further increase of the products concentration. A significant increase in the ratio between CO and CO_2 is observed from minute 4, when exhaustion starts to take place, like in thermal operation.

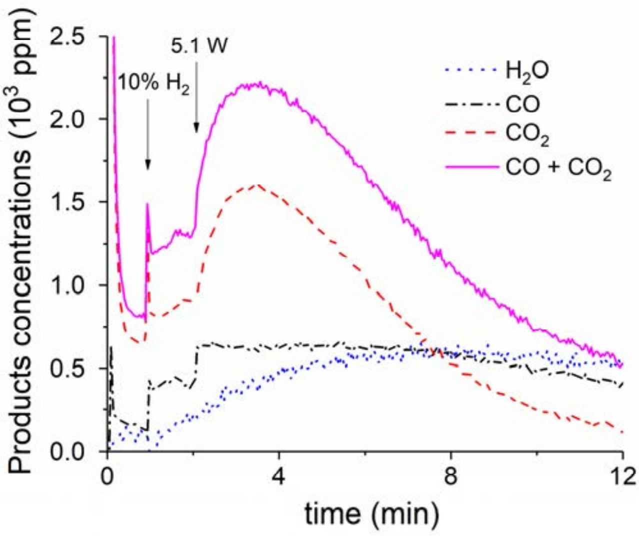

Figure 5.3: *Concentrations of the gases at the outlet during 10mg $CaCO_3$ (Sample C) decomposition as function of time. Temperature is 630°C, flow rate is 90 ml min^{-1}, feed composition is changes from pure Ar to 10% H_2 in Ar after 1 minute of decomposition, plasma power changes from 0 to 1.5 W after 2 minutes of decomposition.*

Several decomposition experiments are performed on samples from A to D. The experiments are improved by lowering temperature and flow rate to 590°C and 30 ml min^{-1} in order to extend the decomposition time, allowing to probe up to three power values before exhaustion. A typical experiment is shown in figure 5.4 for sample C, while the rest of the results are collected in Appendix A5 and shown in figures A5.1-A5.4.

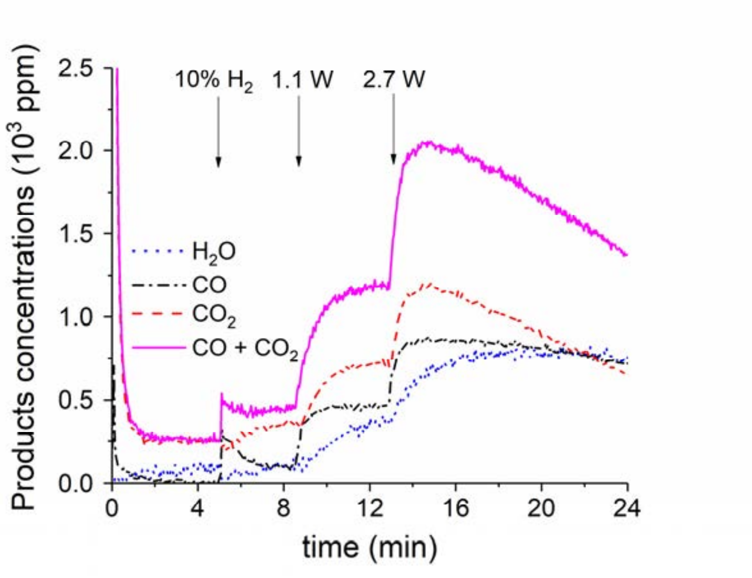

Figure 5.4: *Concentrations of the gases at the outlet during 10mg* $CaCO_3$ *(Sample C) decomposition as function of time. Temperature is 590°C, flow rate is 30 ml* min^{-1}*, feed composition changes from pure Ar to 10%* H_2 *in Ar after 5 minutes of decomposition; plasma is turned on after 9 min and plasma power changes from 0 W to 1.1 W and 2.7 W every 4 to 5 min.*

5.4 Discussion

5.4.1 Effect of hydrogen on the decomposition rate in thermal operation

In thermal operation, the decomposition rate increases by introducing hydrogen. The rate enhancement is defined by the ratio between the reaction rates in presence of hydrogen and in pure Ar at the same temperature, i.e. between the sum of CO_2 and CO concentrations obtained in presence of hydrogen and the CO_2 concentration obtained in pure Ar, as shown in equation 5.1.

$$Enhancement = \frac{([CO] + [CO_2])_{10\%H2}}{[CO_2]_{Ar}} \tag{5.1}$$

Figure 5.5 shows the enhancement of the decomposition rate observed during decomposition of samples A-C as function of $CaCO_3$ surface area, based on the results in figures from A5.1 to A5.3, and of samples C-D as function of the particles size, based on the results in figures A5.3 and A5.4. Apparently, the rate enhancement increases with increasing surface area, whereas there is no significant change as function of the particles size. The error margin is evaluated to be ± 7% due to possible drift in the MS signals.

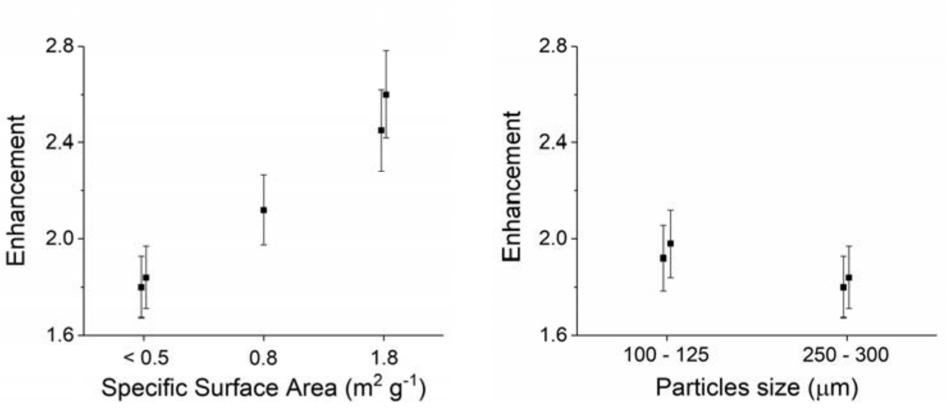

(a) **(b)**

***Figure 5.5**: Rate enhancement between decomposition in 10% H_2 in Ar and decomposition in pure Ar of samples A, B, C **(a)** and samples C, D **(b)**; temperature is 590°C; flow rate is 30 ml min^{-1}; no plasma is applied.*

The enhancement of the rate may be caused by the presence of water on the sample produced by RWGS, since water has a catalytic effect on calcium carbonate decomposition via formation of surface calcium bicarbonate, as reported in Chapter 2.

Figure 5.6 shows the rate enhancement during decomposition of all the four samples as function of the average water partial pressure in the packed bed. The H_2O partial pressure is evaluated assuming linear concentration profiles between no water at the inlet and the water concentration at the outlet, and the whole concentration windows are shown by the horizontal bars, which are not error margins. Noteworthy, both rate enhancement and water concentration produced during decomposition in H_2 increase with the $CaCO_3$ surface area, resulting in a clear correlation within the experimental error.

These observations are compared in figure 5.6 with the results of Chapter 2, obtained by decomposing $CaCO_3$ in presence of different H_2O concentrations in Ar. All samples show a very similar trend, confirming that the rate enhancement is indeed caused by water. All the other variables do not influence.

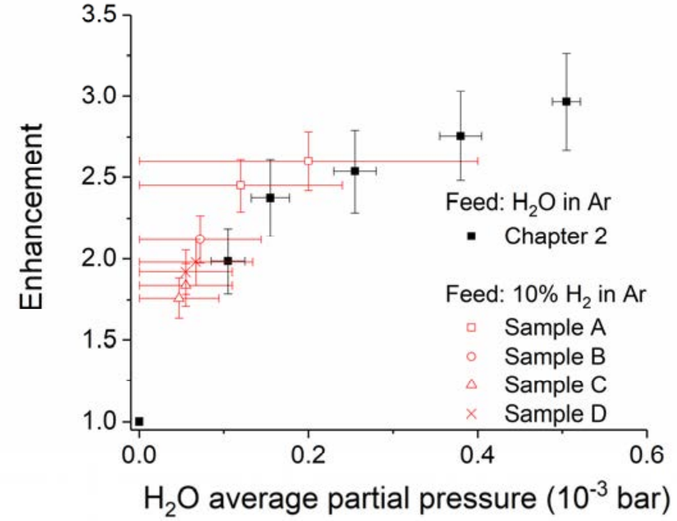

Figure 5.6: *empty symbols: rate enhancement as function of H_2O average partial pressure during decomposition of samples A, B, C and D performed in this study, feed is 10% H_2 in Ar, flow rate is 30 ml min^{-1}, applied temperature is 590°C, no plasma is applied; full symbols: rate enhancement during $CaCO_3$ decomposition performed in Chapter 2, feed is H_2O in Ar, flow rate is 90 ml min^{-1}, applied temperature is 590°C.*

5.4.2 Effect of plasma on the decomposition rate

The decomposition rate increases with plasma power, as shown in figure 5.3 and figures A5.1-A5.4. Figures 5.7a and 5.7b show the sum of CO and CO_2 concentrations as function of plasma power during decomposition of samples with different surface area (A, B and C) and different particles size (C and D) respectively. Apparently, the decomposition rate increases with increasing surface area and decreasing particles size at the same plasma power, which suggests that plasma has both a thermal effect and a chemical effect on the decomposition rate. Nevertheless, also the catalytic effect of water could explain the effect of particles size. In fact, figure 5.8 shows that the water concentration also increases with decreasing particles size at the same power, as results from the same experiments on samples C and D of figure 5.7b. The effect of particles size on water concentration will be addressed in the next paragraph.

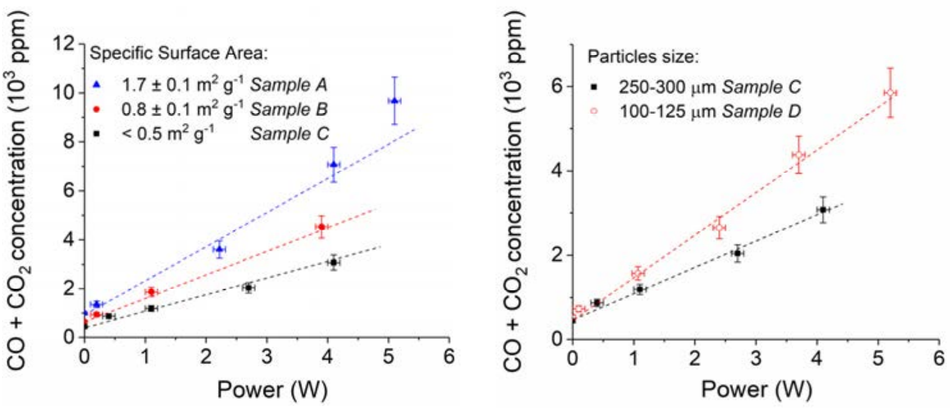

(a) **(b)**

Figure 5.7: *Sum of CO and CO_2 concentrations during decomposition of samples A, B and C* ***(a)*** *and samples C and D* ***(b)*** *as function of plasma power. Applied temperature is 590°C, flow is 30 ml min^{-1}.*

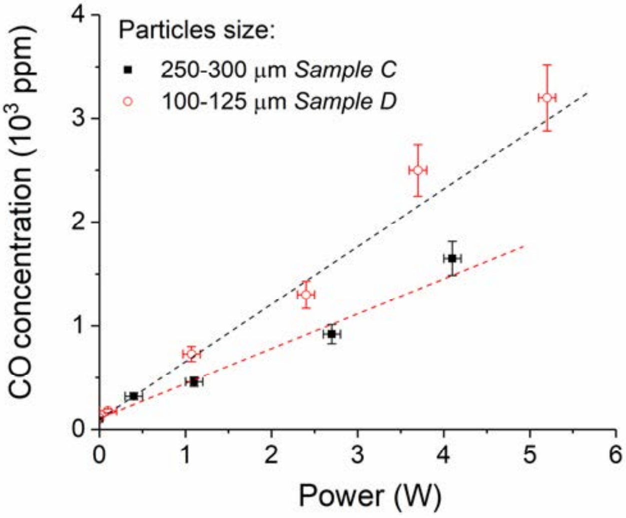

Figure 5.8: *CO concentration during decomposition of samples C and D as function of plasma power. Applied temperature is 590°C, flow rate is 30 ml min^{-1}.*

Figure 5.9 shows the rate enhancements obtained by decomposing different $CaCO_3$ samples in 10% H_2 in Ar respect to a pure Ar plasma as function of the average water concentration at different plasma power: 1.1 W in figure 5.9a, between 2.2 and 2.7 W in figure 5.9b, between 3.7 and 4.1 W in figure 5.9c. The enhancements are based on the experiments on figures A5.2, A5.3a and A5.4a (figure 5.9a), A5.1a, A5.3a and A5.4b (figure 5.9b), A5.1b, A5.2, A5.3b and A5.4a (figure 5.9c). Like in figure 5.5, the rate enhancements in 10% H_2 plasma are compared with the enhancements obtained by decomposing $CaCO_3$ at various H_2O concentrations in Ar in Chapter 2. The comparison has been made by correcting for the increase of temperature caused by plasma, approximatively 20°C (figure 5.9a), 40°C (figure 5.9b) and 60°C (figure 5.9c). The temperature increase as function of plasma power is estimated in figure 3.12 of Chapter 3, based on kinetics of $CaCO_3$ decomposition in argon plasma measured at 630°C on the same samples used for this study. Figure 5.8 shows that the rate enhancements correlate similarly with H_2O concentration within experimental error, for both H_2 plasma and thermal experiments with H_2O in Ar. Therefore, increasing $CaCO_3$ decomposition rate induced by hydrogen plasma can be accounted for by increasing temperature and increasing water concentration; in other words, there is no proof for any chemical plasma effect

5.4.3 Effect of decomposition level on CO formation in thermal operation

The result shown in figure 5.2 indicates that ratio between CO and CO_2 increases significantly when $CaCO_3$ decomposition reaches an advanced level, suggesting a change in the mechanism of CO formation. This could be explained by the catalytic effect of CaO on RWGS presented in Chapter 4. The exposed CaO surface in expected to increase with the decomposition level, enhancing the CO formation via RWGS.

Figure 5.10 shows (black squares) the CO concentration observed during the experiment in figure 5.2 as function of the decomposition level, i.e. the fraction of $CaCO_3$ decomposed. The CO concentration shown in figure 5.2 is sampled at different decomposition times between 4 and 20 minutes, while the decomposition level relative to the each time is obtained with the mass balance, calculated via integration of the CO + CO_2 concentration curve, resulting in the data points in figure 5.10. The first three data points are collected at temperatures of 590°C, 610°C and 630°C, while the last three data points are all collected at 650°C.

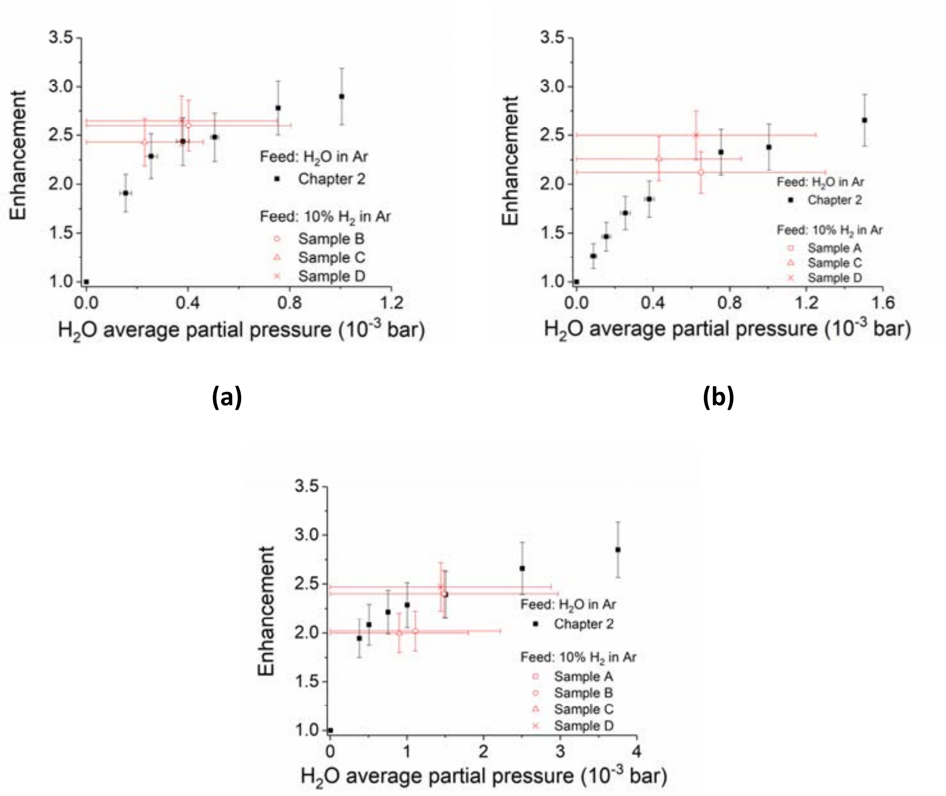

(a)

(b)

(c)

***Figure 5.9**: empty symbols: rate enhancement as function of H_2O average partial pressure during decomposition of samples A, B, C and D performed in this study, feed is 10% H_2 in Ar, flow rate is 30 ml min^{-1}, applied temperature is 590°C, corrected temperatures are 610°C **(a)**, 630°C **(b)** and 650°C **(c)**; plasma power is between 1 and 1.2 W **(a)**, 2.2 and 2.7 W **(b)**, 3.7 and 4.1 W **(c)**; full symbols: rate enhancement during thermal $CaCO_3$ decomposition (no plasma) performed in Chapter 2, feed is H_2O in Ar, flow rate is 90 ml min^{-1}, applied temperatures are 610°C **(a)**, 630°C **(b)** and 650°C **(c)**.*

Figure 5.10 shows also the CO concentrations obtained via RWGS, calculated by applying the model equations developed in Chapter 4 on “Al_2O_3” (blue circles) and “CaO + Al_2O_3” samples (red triangles) in thermal operation. “Al_2O_3” corresponds to sample C without $CaCO_3$ and “CaO + Al_2O_3” corresponds to sample C completely decomposed.

The kinetics of RWGS were evaluated in Chapter 4 on alumina and calcium oxide, which are both active, whereas $CaCO_3$ is not active for RWGS. The comparison between experimental and calculated CO concentration is meant to assess whether the CO formation can be accounted by the $CaCO_3$ decomposition reaction and consecutive RWGS (R_1 and R_3 in scheme 1). The CO concentration produced in small segments of the reactor is calculated by applying the rate equations based on a Power Law for "Al_2O_3" and "CaO + Al_2O_3", which are evaluated in Chapter 4 and shown in table 4.1. The CO concentration profile within the reactor is obtained by accumulating the concentrations for each segment and is calculated via mathematical integration using the script in MATLAB shown in the appendix A4 in the previous Chapter. The models are applied by mimicking the same CO_2 and H_2 concentration profiles present during the decomposition experiment in figure 5.2 for each decomposition level. The CO_2 profile is assumed linear along the packed bed in the reactor: in the inlet there is obviously zero CO_2, while at the outlet there is the sum of CO and CO_2 measured during the experiment at the selected decomposition level. H_2 concentration is assumed constant at 10%.

Apparently, the CO concentration in figure 5.2 agrees with RWGS on "Al_2O_3" only at the beginning of the reaction, when the sample is mostly $CaCO_3$, in line with the observation that bulk $CaCO_3$ is not active for RWGS. After 10% of decomposition, the CO concentration is enhanced presumably via catalysis on the increasing CaO surface. At 80% of the decomposition, the CO concentration approaches the RWGS on "CaO + Al_2O_3", as expected since the $CaCO_3$ is almost totally converted to CaO. In short, the kinetics model reported in Chapter 4 is well able to explain the result of the thermal decomposition experiment semi-quantitatively, confirming that CaO is catalytically active for RWGS whereas $CaCO_3$ is not.

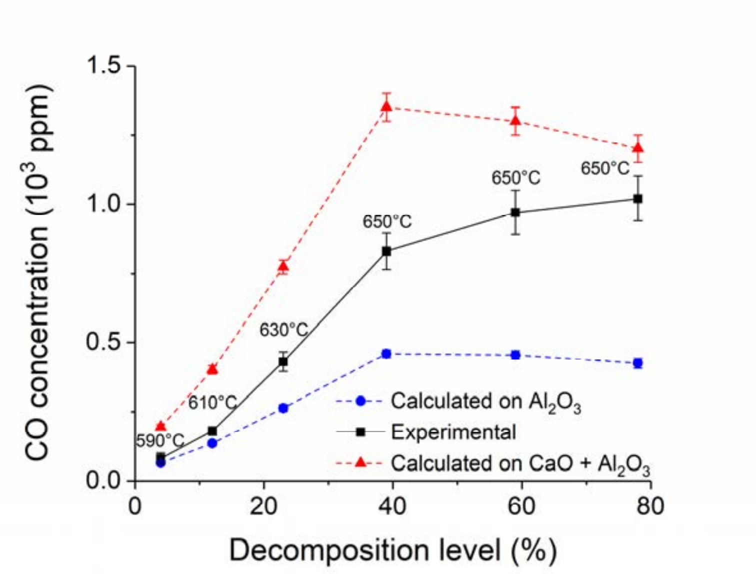

***Figure 5.10**: CO concentration at the outlet during 10mg $CaCO_3$ decomposition as function of the decomposition level (squares); CO concentration calculated via RWGS on "Al_2O_3" (circles) and on "CaO + Al_2O_3" (triangles) with the same CO_2 concentration observed during the decomposition of 10 mg $CaCO_3$ and assuming a linear CO_2 concentration profile, as calculated by modelling the RWGS reaction rate with power law equation defined in Chapter 4.*

5.4.4 Effect of decomposition level on CO formation in plasma operation

As for thermal operation, the ratio between CO and CO_2 increases when $CaCO_3$ decomposition reaches an advanced level also in presence of plasma. Analogously, this could be explained by the synergetic effect between plasma and CaO on RWGS, also studied in Chapter 4. A comparison between experimental CO concentration and RWGS models in plasma operation is presented as follows.

Figure 5.11 shows (black squares) the CO concentration obtained during the experiment of figure 5.3 in presence of plasma as function of decomposition level. The CO concentration is sampled at different decomposition times and the decomposition level is calculated by the mass balance, as described above. In order to correct for the difference in plasma power between the experiment at 1.5 W and the models at 1 W, the CO measured both at 0 W and 1.5 W allowed linear interpolation at 1 W. All the data points shown are measured at the same applied temperature of 630°C.

Figure 5.11 shows also the CO concentration obtained via RWGS, calculated by applying the model equations developed in Chapter 4 on “Al_2O_3” (blue circles) and “$CaO + Al_2O_3$” (red triangles) in plasma operation at 1 W power, also shown in table 4.1. The CO concentration profile along the packed bed is obtained with the same method described above applying the rate equations evaluated in plasma operation, also shown in Chapter 4. The CO_2 and H_2 profiles are evaluated in the same way as for thermal operation.

Before 40% of decomposition, the CO concentration agrees with the RWGS on “Al_2O_3”, sign that $CaCO_3$ is not active for RWGS both in thermal and in plasma operations, whereas the CO formation proceeds mainly through gas phase plasma chemistry. The CO concentration approaches the concentration obtained during RWGS on “$CaO + Al_2O_3$” in presence of plasma, when the sample is significantly decomposed and CaO is present, implying that CO formation proceeds mainly via RWGS.

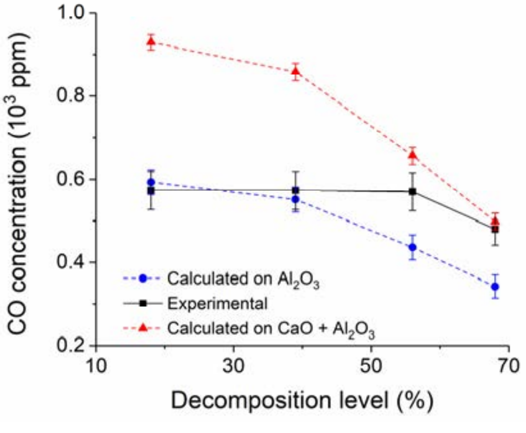

***Figure 5.11**: CO concentration at the outlet during 10mg $CaCO_3$ decomposition in presence of plasma as function of the decomposition level (squares); CO concentration calculated via RWGS on “Al_2O_3” (circles) and on “$CaO + Al_2O_3$” (triangles) with the same CO_2 concentration observed during the decomposition of 10mg $CaCO_3$ and assuming a linear CO_2 concentration profile, as calculated by modelling the RWGS reaction rate with power law equation defined in Chapter 4.*

Summarizing, the results in figures 5.10 and 5.11 indicate that the CO production in driven mainly by RWGS in both thermal and plasma operation, which is enhanced by the developing calcium oxide surface. Calcium carbonate is not active for CO formation in any operation.

In addition, the results in figure 5.8 show that the CO concentration increases by decreasing the particles size at the same plasma power, implying that CO formation is sensitive to the external surface area of the bed particles. According to the method developed in Chapter 3, CO formation is driven by plasma chemistry. It is not trivial to assess where the plasma chemistry occurs, because of the following considerations:

- $CaCO_3$ surface is certainly not active for CO formation as resulted from figure 5.11;
- CaO surface is certainly active for plasma catalytic RWGS, however the CO concentrations shown in figure 5.8 are measured at a decomposition level between 10% and 40%, i.e. when calcium oxide shows no significant activity according to figure 5.11. It must be noted that the accuracy of the evaluation in figure 5.11 is not enough to conclude whether CaO is active when less of 40% of $CaCO_3$ is decomposed, since the CO concentration measured during $CaCO_3$ decomposition was corrected for a difference in plasma power. Unfortunately, only the experiment shown in figure 5.3 could be compared with the RWGS kinetics in plasma operation, since a constant plasma power through the decomposition was necessary. To perform other experiments was not possible, since no time was left in the research plan;
- Al_2O_3 surface might also be active for plasma-catalytic RWGS. We have no evidence to confirm or negate this, since "Al_2O_3" was the blank experiment in Chapter 4;
- Changing particles size might affect the plasma and influence the CO formation via gas phase plasma chemistry.

In short, CO_2 hydrogenation in DBD plasma is still not completely clear, whereas $CaCO_3$ decomposition is apparently not affected by any plasma chemistry in presence of hydrogen.

5.5 Conclusions

The effects of DBD hydrogen plasma on $CaCO_3$ decomposition have been assessed, by means of a comparative method which allowed us to distinguish between thermal effects and plasma chemistry, based on reaction rates.

In thermal operation, hydrogen causes an increase in the rate of $CaCO_3$ decomposition by an indirect effect of the water produced along with CO via consecutive RWGS. The RWGS reaction is enabled by the presence of calcium oxide and alumina.

In plasma operation, both decomposition rate and CO formation increase. The decomposition rate is enhanced by a purely thermal effect. The CO formation occurs exclusively via RWGS and is catalysed by the synergetic effect of calcium oxide and plasma.

References

[1] NASA. Global Climate Change Vital Signs of the Planet **2018**.

https://climate.nasa.gov/

[2] United Nations Climate Change. The Paris Agreement **2015**.

https://unfccc.int/process-and-meetings/the-paris-agreement/the-paris-agreement

[3] International Energy Agency. *World Energy Outlook* **2017**.

https://www.iea.org/weo2017/

[4] E. J. Anthony. Carbon Capture and Storage and Carbon Capture, Utilization and Storage 2017. *Coal in the 21st century: energy needs, chemicals and environmental controls* **2017**, 198-215.

[5] M. Bui, C. S. Adjiman, A. Bardow, E. J. Anthony, A. Boston, S. Brown, P. S. Fennell, S. Fuss, A. Galindo, L. A. Hackett, J. P. Hallett, H. J. Herzog, G. Jackson, J. Kemper, S. Krevor, G. C. Maitland, M. Matuszewski, I. S. Metcalfe, C. Petit, G. Puxty, J. Reimer, D. M. Reiner, E. S. Rubin, S. A. Scott, N. Shah, B. Smit, J. P. M. Trusler, P. Webley, J. Wilcox, and N. Mac Dowell. Carbon capture and storage (CCS): the way forward. *Energy Environm. Sci.* **2018**, 11, 1062-1176.

[6] D. Y. C. Leung, G. Caramanna, and M. M. Maroto-Valer. An overview of current status of carbon dioxide capture and storage technologies. *Renewable and Sustainable Energy Reviews* **2014**, 39, 426-443.

[7] J. Blamey, E. J. Anthony, J. Wang, and P. S. Fennell. The calcium looping cycle for large-scale CO_2 capture. *Progress in Energy and Combustion Science* **2010**, 36, 260-279.

[8] B. J. McBride, M. J. Zehe, and S. Gordon. NASA Glenn Coefficients for Calculating Thermodynamic Properties of Individual Species **2002**.

https://www.grc.nasa.gov/WWW/CEAWeb/TP-2002-21556.htm

[9] R. Barker. The reversibility of the reaction $CaCO_3 \rightleftharpoons CaO + CO_2$. *Journal of Chemical technology and Biotechnology* **1973**, 23, 733-742.

[10] R. H. Borgwardt. Sintering of nascent calcium oxide. *Chemical Engineering Science* **1989**, 44, 53-60.

[11] P.S. Fennell, R. Pacciani, J. S. Dennis, J. F. Davidson, and A. N. Hayhurst. The effects of repeated cycles of calcination and carbonation on a variety of different limestones, as measured in a hot fluidized bed of sand. *Energy & Fuels* **2007**, 21, 2072-2081.

[12] A. I. Lysikov, A. N. Salanov, and A. G. Okunev. Change of CO_2 carrying capacity of CaO in isothermal recarbonation-decomposition cycles. *Ind. Eng. Chem. Res.* **2007**, 46, 4633-4638.

[13] W. Liu, N. W. Low, B. Feng, G. Wang, and J.C. Diniz da Costa. Calcium precursors for the production of CaO sorbents for multicycle CO_2 capture. *Environ. Sci. Technol.* **2010**, 44, 841-847.

[14] A. Reller, C. Padeste, and P. Hug. Formation of organic compounds from metal carbonates. *Nature* **1987**, 329, 8, 527-529.

[15] T. T. Belete. Evaluation of (Plasma-assisted) Decomposition of Transition Metals Doped $CaCO_3$ for CO_2 Capture and Conversion. *Ph.D. Thesis* **2019**.

[16] E. C. Neyts, K. Ostrikov, M. K. Sunkara, and A. Bogaerts. Plasma Catalysis: Synergistic Effects at the Nanoscale. *Chem. Rev.* **2015**, 115, 13408–13446.

[17] J. C. Whitehead. Plasma-catalysis: The known knowns, the known unknowns and the unknown unknowns. *J. Phys. D Appl. Phys.* **2016**, 49, 243001.

[18] A. Fridman. Plasma Chemistry. *Cambridge University Press,* Cambridge, UK, **2008**.

[19] H. H. Kim, Y. Teramoto, N. Negishi, and A. Ogata. A multidisciplinary approach to understand the interactions of nonthermal plasma and catalyst: A review. *Catal. Today* **2015**, 256, 13–22.

[20] A. Bogaerts, T. Kozák, K. van Laer, and R. Snoeckx. Plasma-based conversion of CO_2: Current status and future challenges. *Faraday Discuss.* **2015**, 183, 217–232.

[21] F. Brehmer, S. Welzel, M. C. M. van de Sanden, and R. Engeln. CO and byproduct formation during CO_2 reduction in dielectric barrier discharges. *J. Appl. Phys.* **2014**, 116, 123303.

[22] M. Scapinello, L. M. Martini, and P. Tosi. CO_2 Hydrogenation by CH_4 in a Dielectric Barrier Discharge: Catalytic Effects of Nickel and Copper. *Plasma Processes and Polimers* **2014**, 11, 7, 624-628.

[23] S. Kameshima, K. Tamura, R. Mizukami, T. Yamazaki, and T. Nozaki. Parametric analysis of plasma-assisted pulsed dry methane reforming over Ni/Al_2O_3 catalyst. *Plasma Process. Polym.* **2017**, 14, 1600096.

[24] A. Ozkan, T. Dufour, G. Arnoult, P. de Keyzer, A. Bogaerts, and F. Reniers. CO_2-CH_4 conversion and syngas formation at atmospheric pressure using a multi-electrode dielectric barrier discharge. *J. CO_2 Util.* **2015**, 9, 78–81.

[25] Y. Zeng, X. Zhu, D. Mei, B. Ashford, and X. Tu. Plasma-catalytic dry reforming of methane over γ-Al_2O_3 supported metal catalysts. *Catal. Today* **2015**, 256, 80–87.

[26] N. G. Moncada. Synergy of Thin Catalytic Layers and DBD Plasma for Coupling of Methane. *12th Natural Gas Conversion Symposium* **2019**.

[27] K. H. R. Rouwenhorst, H. H. Kim, and L. Lefferts. Vibrationally Excited Activation of N_2 in Plasma-Enhanced Catalytic Ammonia Synthesis: A Kinetic Analysis. *ACS Sustainable Chem. Eng.* **2019**, 7, 20, 17515-17522

[28] Y. R. Zhang, K. van Laer, E. C. Neyts, and A. Bogaerts. Can plasma be formed in catalyst pores? A modeling investigation. *Appl. Catal. B Environ.* **2016**, 185, 56–67.

[29] K. Hensel, S. Katsura, and A. Mizuno. DC Microdischarges inside porous ceramics. *IEEE Trans. Plasma Sci.* **2005**, 33, 574–575.

[30] F. J. J. Peeters, and M. C. M. van de Sanden. The influence of partial surface discharging on the electrical characterization of DBDs. *Plasma Sources Sci. Technol.* **2015**, 24, 15016.

Chapter 6

General assessment on the use of DBD for $CaCO_3$ decomposition

6.1 Introduction

The research discussed in this thesis and the parallel work of Tesfaye Belete in DIFFER [1] evaluated the possibilities of combining Dielectric Barrier Discharge (DBD, in Twente) and Inductively Coupled Plasma (ICP, in DIFFER) with calcium carbonate decomposition. The effects of DBD and ICP plasmas on the decomposition and the addition of transition metals impurities in $CaCO_3$ were investigated and are described in the two PhD theses. The main conclusions of the work in Twente are summarized in this chapter, leading to ideas for further research and future plasma-catalytic combinations for $CaCO_3$ decomposition and CO_2 conversion.

Figure 6.1 summarizes the reactions taking place in the process, consisting in two main phases which are 1) decomposition of calcium carbonate to calcium oxide and CO_2, and 2) subsequent conversion of CO_2. The specific gas components are mentioned alongside the different reaction processes, as well as the energy input or catalytic effect effectively driving the specific reaction. Only the forward reactions are shown in figure 6.1, because the experiments were performed mostly far away from equilibrium.

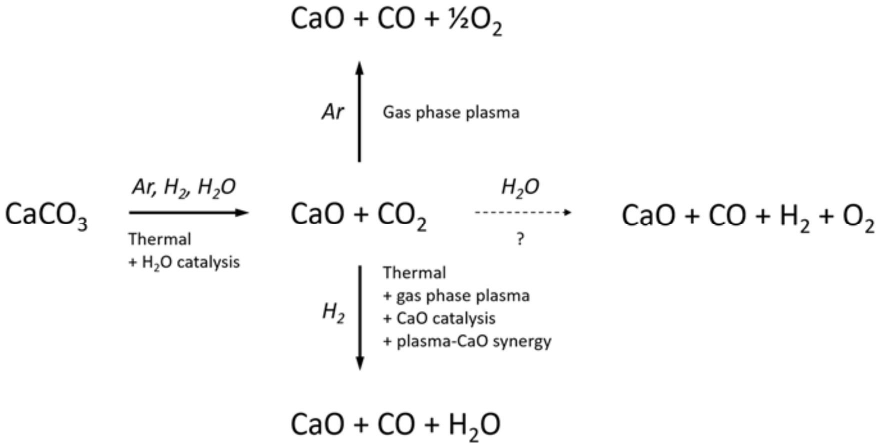

***Figure 6.1**: Reaction scheme of $CaCO_3$ decomposition in presence of DBD plasma*

The main and negative conclusions are that 1) calcium carbonate decomposes solely into calcium oxide and carbon dioxide for all the conditions studied and 2) the reaction is driven by temperature only in both thermal operation and plasma operation, i.e. plasma does not have any physical or chemical effect on the calcium carbonate decomposition (Chapters 3 and 5). Also, the reaction is enhanced by presence of water vapour via a catalytic effect involving the formation of surface calcium bicarbonate as intermediate (chapter 2).

CO_2 furtherly decomposes in several conditions. For instance, CO_2 dissociates into CO and O, eventually recombining in O_2, in gas phase argon plasma (Chapter 3). In presence of H_2, CO_2 takes part in the Reverse Water Gas Shift (RWGS) both in thermal operation and in plasma operation, with calcium oxide having a catalytic role (chapter 4). In presence of H_2O plasma, CO_2 decomposes to CO, H_2 and O_2, which are present in very low concentrations. Because of it, this pathway has not been addressed furtherly.

The two scientific challenges of this study were 1) to distinguish between thermal, physical and chemical effects of plasma on the specific reactions and 2) to address the complexity of a reactor stage with $CaCO_3$ decomposing in the DBD plasma generation zone, trying to discriminate between the effects of $CaCO_3$/CaO on plasma and vice versa.

The main topics covered in this project were:

- Kinetics of thermal $CaCO_3$ decomposition in argon and water vapor;
- Effect of Argon DBD plasma on $CaCO_3$ decomposition;
- Synergy between plasma and Calcium oxide on Reverse Water Gas Shift;
- $CaCO_3$ decomposition in presence of hydrogen and hydrogen plasma.

Other topics were explored:

- Effect of plasma on the decomposition in a post-plasma configuration;
- $CaCO_3$ decomposition in presence of H_2O plasma;
- Transition metals doped $CaCO_3$ decomposition in presence of hydrogen.

6.2 Kinetics of thermal $CaCO_3$ decomposition in argon and water vapour

The kinetics of thermal $CaCO_3$ decomposition in argon and in presence of steam were measured in a plug flow reactor using small amounts of carbonate, i.e. less than 10 mg. Flowing gas through a fixed bed improved significantly the reliability of the kinetic data respect to studies where TGA and XRD cups were conventionally used [2, 3], since the CO_2 desorbed from the sample is rapidly flushed away, preventing backward reaction.

Calcium carbonate decomposition in argon is an activated process, with an activation barrier of 201 kJ mol^{-1} slightly higher than the difference in enthalpy of 171 kJ mol^{-1} [4]. Since the reaction is endothermic, the temperature to obtain a reasonable CO_2 concentration in the product stream is significantly high, i.e. at least 950°C to obtain pure CO_2 at atmospheric pressure [4], as stated in the introductory chapter. This temperature is not suitable for $CaCO_3$ long-term recycling, since the lack in stability of the material resulting in sintering [5], thus the need to explore conditions such as H_2O and H_2 co-reactants and plasma in order to lower the decomposition temperature.

The addition of low concentrations of steam, i.e. less than 1.25%, has a catalytic effect on the decomposition via formation of surface calcium bicarbonate. In presence of steam the activation barrier is lowered to 140 kJ mol^{-1}, the reaction rate is increased up to 5 times and therefore the decomposition temperature can be reduced by ca. 70°C, according to the kinetics of the reaction.

The study of the steam effect on $CaCO_3$ decomposition is relevant since ca. 20% of the flue gases of power plants is composed by steam [6]. Nevertheless, in order to test any significant benefit, further studies must be performed. Firstly, the catalytic effect must be tested at more relevant temperatures, i.e. between 800 and 900°C, respect to the conditions applied in our experiments, between 590 and 650°C. Secondly, steam in such high concentrations has other effects such as decrease of the CO_2 gas phase diffusivity and increase of the heat transfer coefficient, which have a significant impact on the decomposition rate according to Kraisha et al. [7] and Yin et al. [8].

Steam has also a regenerative effect on spent CaO samples via formation of calcium hydroxide, according to Anthony et al. [9], which could lead to the addition of a regeneration step in a practical application. This effect has also been observed during our work on the catalytic effect of steam as follows.

Figure 6.2 shows the variations in CO_2 capture on a CaO sample during alternated CO_2 absorption- CaO regeneration processes, as function of the H_2O concentration applied during the regeneration step. The absorption and regeneration steps were alternated by shifting the gas composition from Ar + H_2O to Ar + 5% CO_2 and vice versa. The absorption and full regeneration have been performed 40 times in absence of steam before- and 50 more times in presence of steam during- the data acquisition. Figure 6.2 shows that the CO_2 captured increases between two consecutive cycles only when the steam concentration during regeneration is at least 0.5%. Stronger increases in CO_2 are obtained by storing the regenerated CaO in ambient for several weeks.

In conclusion, steam applied during $CaCO_3$ decomposition improves both the decomposition reaction and the sample morphology. The effect on the decomposition rate is not so strong and probably won’t lead to ground-breaking improvements, nevertheless much more study is needed to assess the extent of such effects and potential benefits for a practical application.

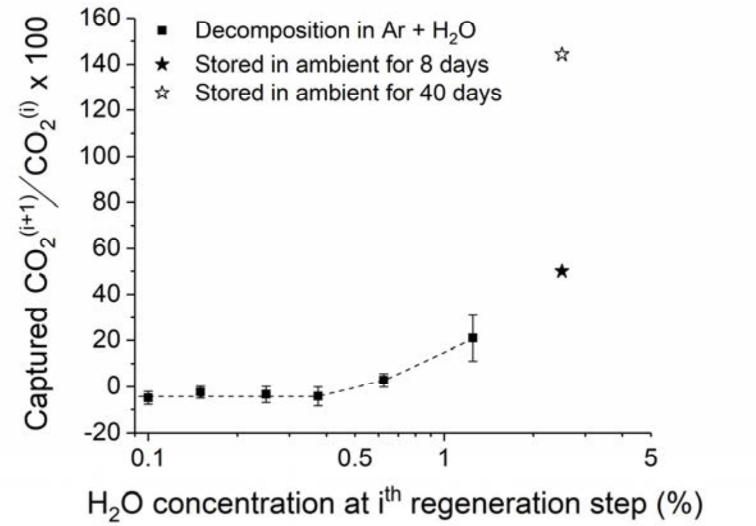

Figure 6.2*: Variation of CO_2 captured during the cyclic CO_2 capture and release performed in Chapter 2 on a spent CaO sample as function of the percentage of steam present during the CaO regeneration step. Capture steps: 15 min at 630°C in 5% CO_2 in Ar. Regeneration steps: ca. 30 min at temperatures between 590 and 650°C in Ar and H_2O. The sample is 3mg CaO in 70 mg SiO_2, flow rate is 90 ml min^{-1}.*

6.3 $CaCO_3$ decomposition in Argon plasma

The result that DBD argon plasma could have just a thermal effect on the decomposition was expected, since argon is a noble gas which could hardly react with $CaCO_3$ and a physical effect is unlikely due to the low power used. Nevertheless, this study was performed to test, successfully, a new-developed method to distinguish between thermal and non-thermal effects of plasma.

The method relies on the assumption that plasma cannot penetrate inside pores smaller than 3 µm [10], i.e. plasma has access only to the external surface of our sample’s particles, whereas the heat produced by plasma diffuses in ca. 1 minute from the external surface to the centre of the particles. Thermal effect and non-thermal effects can be deconvoluted by measuring independently the effects of external and total surface areas on the decomposition rate.

As a result, this method allowed to estimate the average temperature increase in the plasma zone as function of plasma power, with low uncertainty of ±10°C if compared with the current temperature estimations in plasmas (infrared cameras, Optical Emission Spectroscopy, heat transfer modelling, thermocouples outside the plasma zone) [11-14]. Correct temperature evaluation is a key point in understanding the effect of plasma in chemical reactions, especially when synergy is observed between plasma and catalysis [15] (as in chapter 4). We suggest that using our method could improve kinetic studies on plasma and plasma-catalytic systems significantly.

Plasma also induces consecutive CO_2 decomposition into CO and O_2, although it occurs mainly in gas phase plasma since the presence of calcium carbonate / oxide doesn't have any effect. Remarkably, this result disagrees with the study performed by Duan et al. [16] which reports a substantial increase in CO_2 conversion by fully packing the plasma zone with CaO respect to Al_2O_3. Presumably, replacing Al_2O_3 with CaO entirely could influence the plasma significantly, while adding a small amount of CaO in abundant Al_2O_3 did not, also because have similar dielectric constant, 9 and 11.8 for Al_2O_3 and CaO respectively. In conclusion, CO_2 dissociation wasn't studied any further.

6.4 $CaCO_3$ decomposition in presence of steam plasma

Although steam has a catalytic effect on the thermal calcium carbonate decomposition, the application of steam plasma has a negative effect on the CO formation. Figure 6.3 shows that the application of 2.5% of H_2O in Ar results in a similar increase in decomposition rate, while the CO_2 conversion to CO drops dramatically from ca. 50% to less than 2%. Traces of H_2 and O_2 are also found. Snoeckx et al. simulated a CO_2 and H_2O mixture in DBD plasma at ambient conditions [17], concluding that the OH radicals in the plasma cause very rapid CO recombination to CO_2, inhibiting the CO_2 decomposition.

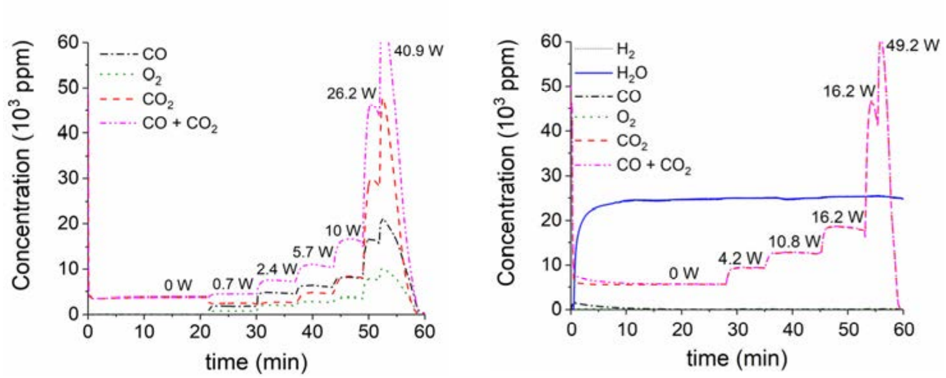

(a) **(b)**

Figure 6.3*: Concentration of the products during decomposition of 120 mg $CaCO_3$ as function of time at 630°C in pure argon* ***(a)*** *and 2.5% water vapor in argon* ***(b)****, flow rate of 30 ml min^{-1}, plasma power is changed every 8 minutes. The packed bed of 2 cm is placed in the middle of the plasma zone, which is long 7 cm*.

The presence of low water concentrations inhibits the CO_2 conversion also in other types of plasmas, e.g. microwave and gliding arc, probably because of faster decay of CO_2 vibrational modes induced by water [18]. Nevertheless, in both DBD and MW plasma the presence of nickel or nickel oxide catalysts seems to bypass the negative effect of H_2O active species [19, 20], but the mechanisms have still to be better understood.

Since no interesting effect of H_2O plasma was found on calcium carbonate decomposition, we rather focused on hydrogen plasma.

6.5 Synergy in presence of calcium oxide and plasma on Reverse Water Gas Shift

RWGS contributes significantly during calcium carbonate decomposition in presence of hydrogen, since it is enabled by both calcium oxide, via formation of surface carbonates, and DBD plasma, via CO_2 decomposition in the gas phase. Furthermore, synergy is observed at the lower operational temperatures when both CaO and plasma are present. The activation energy of this process is rather high in presence of only CaO

(140 kJ mol^{-1}), is lower in presence of plasma and Al_2O_3 (90 kJ mol^{-1}) and even lower in presence of both (40 kJ mol^{-1}), indicating that synergy is caused by a new reaction pathway involving the calcium oxide surface and the active species in the plasma.

The result of synergy and further speculations on the mechanism are supported by a systematic kinetic study of the RWGS reaction in a steady state, on the catalytic only-, plasma only-, and plasma-catalytic systems performed in Chapter 4. The reaction rates were compared at fixed conditions of temperature and gas composition, by minimizing any change in the plasma properties, in residence time and by accounting for the increase of temperature as calculated in Chapter 3.

We believe that this approach is the real added value of this study, since it has never been applied in catalytic studies as far as we know, although we believe it is crucial in order to understand plasma-chemistry in presence of a catalyst without introducing any artefact. Nevertheless, following this approach presents several challenges.

Firstly, the dielectric configurations in the plasma-only and plasma-catalytic experiments should be kept identical in order to minimize changes in the plasma. This is not the case when metal particles are introduced as a catalyst, since metal particles enhances plasma generation significantly in proximity to their surface [21]. In order to avoid any dielectric change, metal particles should be reduced in size or, ideally, replaced by single atoms incorporated in the support structure as impurities.

Secondly, by using a packed bed catalytic phase, it is impossible to study the effect of plasma in the gas phase without varying the residence time and/or the Specific Energy Input of plasma, e.g. by emptying the reactor. In Chapter 4 this issue was avoided by using Al_2O_3 as blank experiment, which contains both gas phase plasma and plasma-alumina contributions. A better solution could be introducing the catalytic phase as a coating on the reactor wall [22]. If the coating is sufficiently thin compared to the reactor diameter, it can be compared with an empty reactor without any effect on the residence time or Specific Energy Input.

6.6 $CaCO_3$ decomposition in presence of hydrogen plasma

Hydrogen has no effect on the decomposition of calcium carbonate, except for a rate enhancement induced indirectly by the presence of water (as in Chapter 2), as a product of the consecutive Reverse Water Gas Shift reaction. Reller et al. claimed that the decomposition temperature is decreased by ca. 100°C by introducing pure hydrogen respect to an inert gas [23]. We believe that the indirect effect of water, present in high concentrations in their set of products, could explain this result.

The contribution of Reverse Water Gas Shift during both thermal and plasma assisted $CaCO_3$ decomposition has been evaluated according to the kinetic study on the RWGS reaction in steady state discussed in the previous paragraph. When the decomposition is at early stage, no RWGS occurs since $CaCO_3$ is not active. At a later decomposition stage, the sample becomes active for RWGS due to the developing CaO and it will reach the maximum at the end of the decomposition, when $CaCO_3$ is completely converted to CaO. In conclusion, hydrogen doesn’t have any effect on the decomposition reaction, but it can be converted to CO to some extent.

6.7 General considerations on the use of hydrogen for $CaCO_3$ decomposition

The idea of this project involved use of DBD plasma on $CaCO_3$ decomposition was to convert CO_2 into fuels, i.e. higher hydrocarbons. Reverse Water Gas Shift on calcium oxide induced by hydrogen plasma, which produces mixtures of CO and H_2 in the outlet stream, could represent a first step towards hydrocarbons production via Fischer-Tropsch synthesis [24]. Although hydrogen is maybe a too expensive co-reactant to convert CO_2, we must consider that hydrogen must be converted to molecules with higher energy density, e.g. hydrocarbons or ammonia, to be economically viable [25]. Thus, it makes sense to use hydrogen for CO_2 conversion.

A pro of using hydrogen on $CaCO_3$ decomposition is that the $CO:H_2$ ratio can be optimized for Fisher-Tropsch by tuning decomposition temperature, hydrogen feed concentration and $CaCO_3$/CaO amount. An issue is the H_2O obtained via RWGS which must be minimized in order to improve hydrocarbon formation. The optimal temperature to synthesize long hydrocarbons with Fischer-Tropsch is typically 150-300°C, while higher temperatures lead to high conversions but producing only methane, which is unwanted since the low energy density respect to long hydrocarbons [24]. It is desirable to add a Fischer-Tropsch step downstream rather than combining it with $CaCO_3$ decomposition in a single step due to the substantial difference in the two processes.

Another way to improve the decomposition in presence of hydrogen is to add low amounts of transition metals like Fe, Ni or Co to the calcium carbonate. Figures 6.4 shows the sample weight as function of temperature during TGA experiments of $CaCO_3$ samples doped with different transition metals. The presence of 10% of Ni and Co (typical catalysts for Fischer Tropsch synthesis) in the $CaCO_3$ structure caused a decrease of decomposition temperature up to 130°C. Noteworthy, the doping don't have the same effect during decomposition in pure helium, implying that hydrogen has an active role in decreasing the decomposition temperature, presumably via activation on TM, rather than the instability of the material. The decomposition of doped $CaCO_3$ also produced a significant amount of CH_4, up to ca. 80% of the products distribution, as shown in figure 6.5. Methane can also be considered as an intermediate for higher hydrocarbons via plasma-assisted methane coupling. Recent studies demonstrated that DBD plasma could significantly improve both Fischer-Tropsch synthesis [26] and methane coupling [22] at relatively low temperatures, which opens new ways to explore.

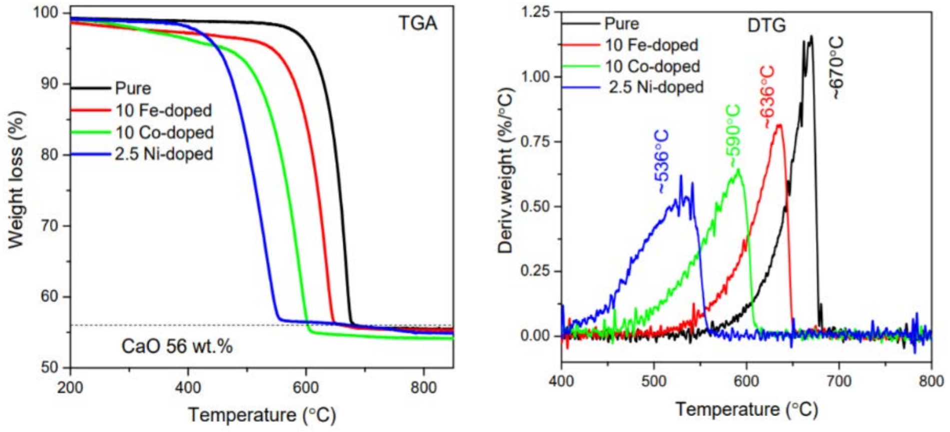

(a) **(b)**

***Figure 6.4**: TGA analysis of samples calcined in 0.6 bar H_2 and 0.4 bar Ar atmosphere. **(a)** Weight loss versus temperature and **(b)** Differentiated profile of samples obtained from first derivative of TGA curves, adapted from [1].*

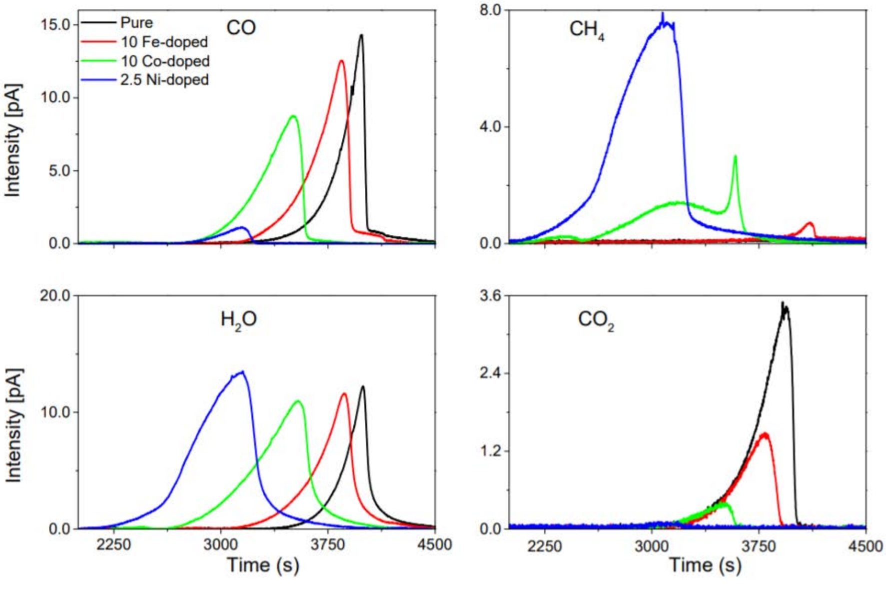

***Figure 6.5**: TGA-MS profile of gases evolved (CO, CH_4, H_2, and CO_2) during calcination of Pure and TM-doped $CaCO_3$ in 0.6 bar H_2 and 0.4 bar Ar atmosphere. (Legend and colours are the same for all panels), adapted from [1].*

6.8 Energy balance

Energy balance has never been considered in the previous chapters of this thesis, since the focus of this thesis was on understanding the effects of plasma instead of reactions optimization. Nevertheless, some considerations about energy balance are given in this paragraph.

The energy efficiency of DBD plasma on $CaCO_3$ decomposition is defined as the ratio between energy stored in the gaseous products and the energy input of the plasma. In all the experiments of $CaCO_3$ decomposition performed, plasma 1) converted CO_2 to CO via chemical effects and 2) increased the rate of CO_2 emission via thermal effect. Both effects induce conversion of electrical energy into chemical energy, both CO and the CO_2 in excess respect to the thermal decomposition are included in the energy balance. The energy efficiency is composed by two terms, the first related to the plasma chemical processes producing CO, the second related to the heat recovery process, producing more CO_2 as shown in equations (6.1-6.3). Note that the difference in enthalpy in equation (6.2) is defined for the specific reaction: it is equal to 285 kJ mol^{-1} for CO_2 dissociation to CO and half oxygen molecule, while it is only 35 kJ mol^{-1} for RWGS. The difference in enthalpy in equation (6.3) is related to $CaCO_3$ decomposition and is equal to 171 kJ mol^{-1}. The gaseous concentrations are measured at the outlet of the reactor, the flow rate is calculated in mol s^{-1} and the plasma power is calculated in Watts.

$$\eta = \eta_{CO} + \eta_{CO2} \tag{6.1}$$

$$\eta_{CO} = \frac{flow\ rate \cdot ([CO] \cdot \Delta H_{CO2\rightarrow CO})}{Plasma\ Power} \tag{6.2}$$

$$\eta_{CO2} = \frac{flow\ rate \cdot ([CO + CO_2] - [CO_2]_{thermal}) \cdot \Delta H_{CaCO3\rightarrow CO2}}{Plasma\ Power} \tag{6.3}$$

Energy efficiency was always very low in all the experiments performed in Chapters 3 and 5, since both the terms shown in equations (6.2) and (6.3) never surpassed 1% each. Such bad efficiency was caused by the fact that explained by the fact that the oven compensated the extra heat in the plasma by providing less energy, since the thermocouple controlling the temperature a few millimetres outside the reactor was programmed to keep the temperature constant, generating an artefact.

Figure 6.6 shows the power provided by the oven as function of the power provided by a pure argon plasma in at a constant temperature of 630°C outside the reactor. The decrease in the oven power is higher than the plasma power, implying that plasma heats up more efficiently than the oven. This is because 1) our oven is 1000 times larger than the plasma zone, which is less than 1 cm^3, and 2) the plasma reactor directs the energy only within the plasma zone and not in the surroundings, as it is in case of a coil heating by the Joule Effect.

This is a good example on how electricity is a very efficient mean to convey energy, since it is more selective and anisotropic than heat. Chemical processes, e.g. $CaCO_3$ decomposition in DBD plasma, could have virtually no energy loss if electrical heating would be applied in chemical industry. In this perspective, renewable electricity is required, which is likely to happen in the next decades, according to the decreasing cost of renewable electricity discussed in the Introduction and shown in figure 1.2.

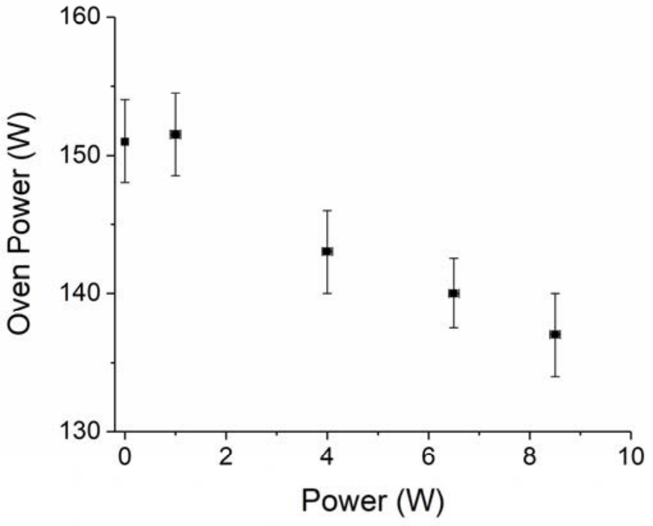

Figure 6.6*: Oven power as function of plasma power. Temperature is 630°C, flow rate is 30 ml/min, the feed gas is pure argon, the sample is 6 mg CaO and 95 mg Al_2O_3.*

6.9 Future research

Since DBD plasma is not capable to activate calcium carbonate, other energy carriers should be explored for $CaCO_3$ decomposition. Electromagnetic radiations might activate crystalline phases better than plasma, because they diffuse within solid phases without diffusion limitations, rather than being confined in open spaces outside the solid.

The fact that radiations can activate $CaCO_3$ selectively has been demonstrated in [27], by applying a combination of microwave radiations and heat to decompose $CaCO_3$ single crystals. As a result, they improved the rate extent of decomposition and reduced reaction time and applied energy. Microwaves are much more efficient than heat, since they convey energy selectively to the $CaCO_3$ rather than the surrounding gas and heated the sample more uniformly respect to thermal energy. Microwaves could also activate chemical processes “non-thermally”, i.e. by directly coupling with the modes of a molecule or lattice and thus reducing the reaction temperature, although the existence of such effects in relation to solid materials is still under debate [28]. Microwaves could also enhance solid diffusion, resulting in sintering [29], which would not be very appealing for $CaCO_3$. In short, activation by microwaves is a promising idea for further research on $CaCO_3$ decomposition since more efficient than heat, although risky from the side of the material stability.

Along the line of electromagnetic radiations, it would be interesting to increase the frequency and explore $CaCO_3$ behaviour under infrared radiations. Although no evidence is found so far in literature, the fact that $CaCO_3$ adsorb specifically on the infrared spectrum (876 and 1425 cm^{-1}) leads to the question whether a very coherent IR radiation could activate directly the $CaCO_3$ vibrational modes rather than increasing the temperature. Ultrashort IR laser pulses in the pico- to femto- seconds range have been used in literature to investigate, among others, the decomposition of CO_2 on ionic surfaces [30] and sub-surface modification of crystalline structures, e.g. sapphire [31].

On the other hand, DBD plasma is a very promising tool for gas phase conversion. Dry reforming of methane is a very attractive reaction to investigate [32]. Calcium oxide would be a very good support for metallic catalysts like Ni, Co or Fe in order to convert CO_2 to higher hydrocarbons via dry reforming and Fischer Tropsch, since it catalyses the first step of the reaction (CO_2 to CO) in presence of hydrogen plasma (provided by the activation of methane) at relatively low temperatures. However, it is not stable at temperatures lower than 600°C in presence of reasonable CO_2 concentrations. Temperatures below 400°C are needed in order to favour the production of higher hydrocarbons respect to methane, thus a more stable oxide with similar catalytic activity for RWGS is needed, e.g. MgO.

References

[1] T. T. Belete. Evaluation of (Plasma-assisted) Decomposition of Transition Metals Doped $CaCO_3$ for CO_2 Capture and Conversion. *Ph.D. Thesis* **2019**.

[2] D. Beruto, and A. Searcy. Use of the Langmuir Method for Kinetic Studies of Decomposition Reactions: Calcite ($CaCO_3$). *J. Chem. Soc., Faraday Trans.* **1974**, 1, 70, 2145-2153.

[3] Y. Wang, and W. J. Thomson. The effects of steam and carbon dioxide on calcite decomposition using Dynamic X-Ray Diffraction. *Chemical Engineering Science* **1995**, 50, 9, 1373-1382.

[4] B. J. McBride, M. J. Zehe, and S. Gordon. NASA Glenn Coefficients for Calculating Thermodynamic Properties of Individual Species **2002**.

https://www.grc.nasa.gov/WWW/CEAWeb/TP-2002-21556.htm

[5] R. H. Borgwardt. Sintering of nascent calcium oxide. *Chemical Engineering Science* **1989**, 44, 53-60.

[6] Y. Artanto, J. Jansen, P. Pearson, T. Do, A. Cottrell, E. Meuleman, and P. Feron. Performance of MEA and amine-blends in the CSIRO PCC pilot plant at Loy Yang Power in Australia. *Fuel* **2012**, 101, 264-275.

[7] Y.H. Khraisha, and D.R. Dugwell. Effect of water-vapor on the calcination of limestone and raw meal in a suspension reactor. *Chemical Engineering Research and Design* **1991**, 69, 76–78.

[8] J. Yin, X. Kang, C. Qin, B. Feng, A. Veeraragavan, and D. Saulov. Modeling of $CaCO_3$ decomposition under CO_2/H_2O atmosphere in calcium looping processes. *Fuel Processing Technology* **2014**, 125, 125-138.

[9] F. Donat, N. H. Florin, E. J. Anthony, and P. S. Fennell. Influence of high-temperature steam on the reactivity of CaO sorbent for CO_2 capture. *Environ. Sci. Technol.* **2012**, 46, 1262-1269.

[10] Y. R. Zhang, K. van Laer, E. C. Neyts, and A. Bogaerts. Can plasma be formed in catalyst pores? A modeling investigation. *Appl. Catal. B Environ.* **2016**, 185, 56–67.

[11] F. Brehmer, S. Welzel, M. C. M. van de Sanden, and R. Engeln. CO and byproduct formation during CO_2 reduction in dielectric barrier discharges. *J. Appl. Phys.* **2014**, 116, 123303.

[12] N. Masoud, K. Martus, M. Figus, and K. Becker. Rotational and vibrational temperature measurements in a high-pressure cylindrical dielectric barrier discharge (C-DBD). *Contrib. Plasma Phys.* **2005**, 45, 32–39.

[13] B. Eliasson, U. Kogelschatz, B. Xue, and L. M. Zhou. Hydrogenation of Carbon Dioxide to Methanol with a Discharge-Activated Catalyst. *Industrial and Engineering Chemistry Research* **1998**, 37, 8, 3350–3357.

[14] B. S. Patil, N. Cherkasov, J. Lang, A. O. Ibhadon, V. Hessel, and Q. Wang. Low temperature plasma-catalytic NO_x synthesis in a packed DBD reactor: Effect of support materials and supported active metal oxides. *Appl. Catal. B Environ.* **2016**, 194, 123–133.

[15] H. H. Kim, Y. Teramoto, N. Negishi, and A. Ogata. A multidisciplinary approach to understand the interactions of nonthermal plasma and catalyst: A review. *Catal. Today* **2015**, 256, 13–22.

[16] X. Duan, Z. Hu, Y. Li, and B. Wang. Effect of dielectric packing materials on the decomposition of carbon dioxide using DBD microplasma reactor. *AlChE Journal* **2014**, 61, 898-903.

[17] R. Snoeckx. Plasma technology. A novel solution for CO_2 conversion? *Ph.D. Thesis* **2017**.

[18] T. Nunnally, K. Gutsol, A. Rabinovich, A. Fridman, A. Gutsol, and A. Kemoun. Dissociation of CO_2 in a low current gliding arc plasmatron. *J. Phys. D: Appl. Phys.* **2011**, 44, 274009.

[19] X. Ma, S. Li, M. Ronda-Lloret, R. Chaudhary, L. Lin, G. van Rooij, F. Gallucci, G. Rothenberg, N. R. Shiju, and V. Hessel. Plasma Assisted Catalytic Conversion of CO_2 and H_2O Over Ni/Al_2O_3 in a DBD Reactor. *Plasma Chemistry and Plasma Processing* **2019**, 39, 109–124.

[20] G. Chen, T. Godfroid, N. Britun, V. Georgieva, M. P. Delplancke-Ogletree, and T. Snyders. Plasma-catalytic conversion of CO_2 and CO_2/H_2O in a surface-wave sustained microwave discharge. *Applied Catalysis B: Environmental* **2017**, 214, 114–125.

[21] H. H. Kim, J. H. Kim, and A. Ogata. Microscopic Observation of Discharge Plasma on the Surface of Zeolites Supported Metal Nanoparticles. *Journal of Physics D: Applied Physics* **2009**, 42, 13.

[22] N. Garcia Moncada, and L. Lefferts. Coupling of Methane in DBD plasma. In progress.

[23] A. Reller, C. Padeste, and P. Hug. Formation of organic compounds from metal carbonates. *Nature* **1987**, 329, 8, 527-529.

[24] J. van de Loosdrecht, F. G. Botes, I. M. Ciobîcă, A. Ferreira, P. Gibson, D. Moodley, A. Saib, J. Visagie, C. Weststrate, and H. Niemantsverdriet. Fischer–Tropsch Synthesis: Catalysts and Chemistry. *Elsevier*, **2013**.

[25] P. Breeze. Hydrogen Energy Storage. Power System Energy Storage Technologies, *Academic Press* **2018**, 69-77.

[26] W. Al-Harrasi, K. Zhang, and G. Akay. Process intensification in gas-to-liquid reactions: plasma promoted Fischer-Tropsch synthesis for hydrocarbons at low temperatures and ambient pressure. *Green Process. Synth.* **2013**, 2, 479-490.

[27] M. Fall, G. Esquenazi, S. Allan, and H. Shulman. Rapid Limestone Calcination Using Microwave Assist Technology. *ACEEE Summer Study on Energy Efficiency in Industry* **2011**.

[28] B. García-Baños, J. J. Reinosa, F. L. Peñaranda-Foix, J. F. Fernández, and J. M. Catalá-civera. Temperature Assessment of Microwave-Enhanced Heating Processes. *Nature Scientific Reports* **2019**, 9, 10809.

[29] A. G. Whittaker. Diffusion in Microwave-Heated Ceramics. *Chem. Mater.* **2005**, 17, 13, 3426-3432.

[30] V. O. Kompanets, V. B. Laptev, S. V. Pigul'skii, E. A. Ryabov, S. V. Chekalin, V. D. Blank, V. N. Denisov, K. S. Kravchuk, B. A. Kulnitskiy and I. A. Perezhogin. The formation of carbonic and silicon dioxide structured films through the decomposition of molecules on the surface of ionic crystals under the action of IR femtosecond laser radiation. *Laser Physics* **2016**, 26, 6.

[31] L. Capuano, R. Pohl, R. M. Tiggelaar, J. W. Berenschot, J. G. E. Gardeniers, G. R. B. E. Römer. Morphology of single picosecond pulse subsurface laser-induced

modifications of sapphire and subsequent selective etching. *Optic Express* **2018**, 26, 22, 29283-29295.

[32] X. Tu, J. C. Whitehead. Plasma-catalytic dry reforming of methane in an atmospheric dielectric barrier discharge: Understanding the synergistic effect at low temperature. *Applied Catalysis B: Environmental* **2012**, 125, 439-448.

Appendix A

A2 Catalytic Effect of Water on Calcium Carbonate Decomposition

MS calibration

Figure A2.1 shows the CO_2 signal elaborated by MS (m/e = 44) for CO_2 concentrations up to 5% in Ar and in the inset CO_2 concentrations up to 1000 ppm are expanded. In this range the signal is linear with the CO_2 concentration, with a R^2 coefficient of 0.9996. The CO signal (m/e = 28) for the CO concentration of 5% in Ar is 1.15 ± 0.05 times larger than the CO_2 signal (m/e = 44) at the same CO_2 concentration

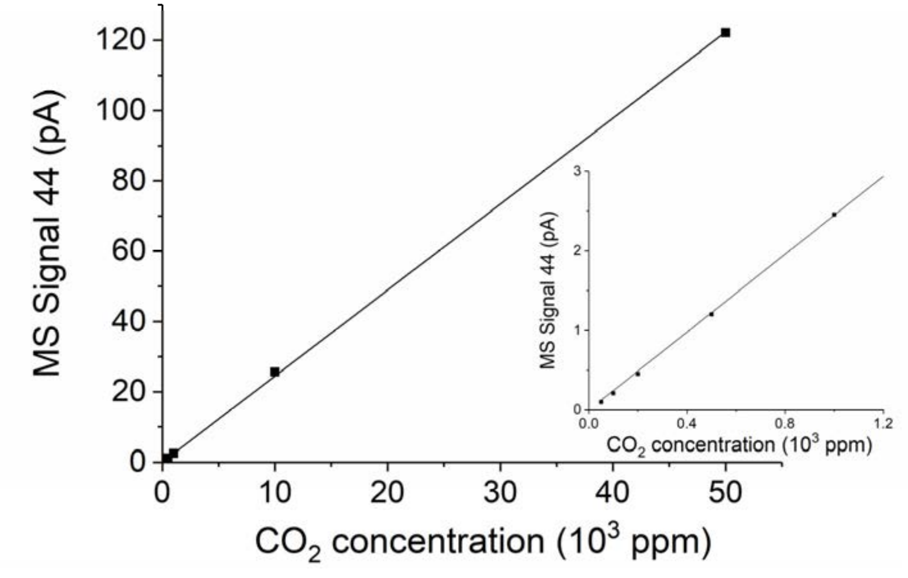

Figure A2.1*: Mass Spectrometer signal m/e = 44 for different CO_2 concentrations in Ar, from 0 to 5%; inset: enhancement of the CO_2 concentration range 0-0.1%.*

MATLAB script for data fitting

The MATLAB script shown in the following pages uses the equation (2.1) with variables K_1 and k_3 to fit the experimental values by minimizing the Root Mean Square (RMS). The experimental error in K_1 and k_3 is estimated by varying the values of K1 and k3, while accepting all combinations that fit all data points within their respective error margins, as illustrated in Figure A2.2.

```
%Input of data points, constants and definition of arrays

Data = ...
[2.50E-06  1.099E-08
1.025E-04  2.183E-08
1.525E-04  2.608E-08
2.524E-04  2.788E-08
3.774E-04  3.029E-08
5.024E-04  3.258E-08
7.523E-04  3.469E-08
1.002E-03  3.638E-08
1.502E-03  3.920E-08
2.502E-03  4.236E-08
3.752E-03  4.434E-08
6.251E-03  4.855E-08
1.250E-02  5.084E-08
];

Errmrg = ...
[2.50E-06  1.099E-09
2.248E-05  2.183E-09
2.497E-05  2.608E-09
2.745E-05  2.788E-09
2.717E-05  3.029E-09
1.890E-05  3.258E-09
6.100E-06  3.469E-09
7.300E-06  3.638E-09
```

```
9.700E-06  3.920E-09
1.450E-05  4.236E-09
2.050E-05  4.434E-09
3.250E-05  4.855E-09
6.250E-05  5.084E-09
];

k2 = Data(1,2);
t = Data(:,1);
y = Data(:,2);
Errx = Errmrg(:,1);
Erry = Errmrg(:,2);

errorbar(t,y,Erry,Erry,Errx,Errx,'ro')

title('Data points')

%Definition of the fitting equation (1.1) as formulated in the
discussion section as function F: the array x (1x2) represents the
couple of floating parameters $K_1$ and $k_3$.

F = @(x,xdata)k2./(1+x(1)*xdata) + x(2)*x(1)*xdata./(1+x(1)*xdata);

x0all = [];
xall = [];
rn = [];

%Fitting process via the built-in function lsqcurvefit

for i = 20:20:5000
        for w = 1:0.5:10
            x0 = [i w];
            [x,resnorm,~,exitflag,output] = lsqcurvefit(F,x0,t,y);
```

```
%Fitting validation: the calculated curve shall by within the error margins of each datapoint

            if x ~= x0
                if resnorm < 1.680E-16
                    n = 0;
                    for m = 1:13
                        An = abs(F(x,t(m)-Errx(m))-y(m));
                        Ap = abs(F(x,t(m)+Errx(m))-y(m));
                        E = Erry(m);
                        if An < E | Ap < E
                            n = n+1;
                        end
                    end
                    if n == 13
                        x0all = [x0all; x0];
                        xall = [xall; x];
                        rn = [rn; resnorm];
                    end
                end
            end
        end
end

%figure A2.2 shows data points and fitting curves for T = 590°C

hold on
for l = 1:length(rn)
    plot(t,F(xall(l,:),t))
end
hold off
```

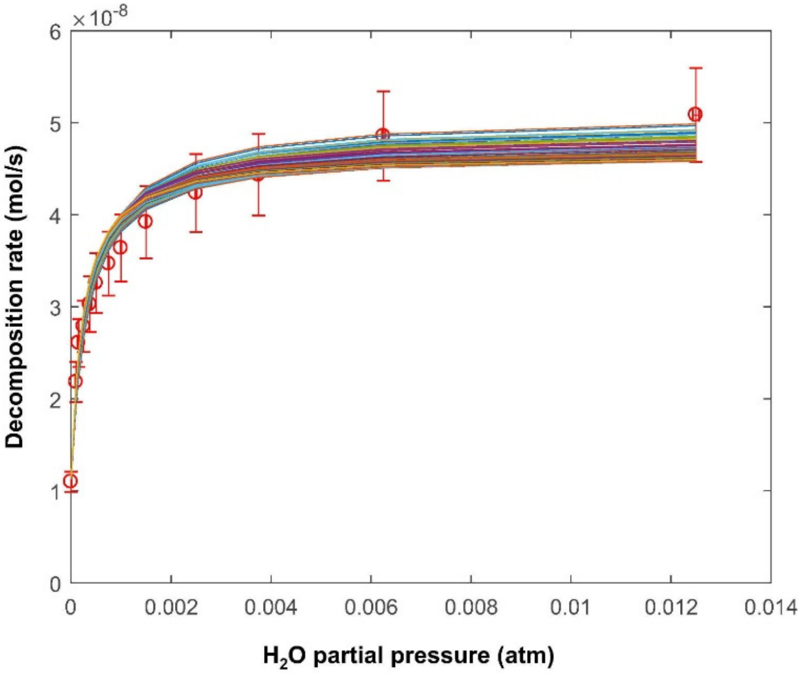

Figure A2.2: *Red data points: the reaction rates in mol* s^{-1} *for different* H_2O *partial pressures up to 0.0025 bar at 590°C; full lines: fitting equations calculated by the script.*

A3 Plasma Catalysis: Distinguishing between Thermal and Chemical Effects

Method

The assumptions made in order to evaluate the argon plasma effect on calcium carbonate decomposition are the following:

- According to the Paschen's Law the electron filaments and active species cannot exist inside the pores of the carbonate particles, this is explained in the following paragraph.
- Temperature gradients between particles outer surface and inner core are minimized within much smaller times than the duration of the experiment, i.e. within 2 min, according to the Fourier time calculated in the specific case.

Figure A3.1 shows the voltage needed to generate a plasma as function of the distance between the charges at an argon pressure of 1 bar, where the parameters A, B, and γ are determined experimentally [59]. The physical mechanism can be explained for the 2 branches of the curve:

- d_{gap} > 6µm: In order to generate a discharge (that is produced by an avalanche of ionizations of Argon atoms by high energy electrons), we need a minimum electric field that is able to accelerate electrons above the ionization energy of Ar atoms in the mean free path of electrons at that pressure (ca. 0.5 µm). Since the electric field is inversely proportional to d_{gap} at constant voltage, V_b increases linearly with d_{gap}.
- d_{gap} < 6µm: the gap distance is comparable with the mean free path, so the probability of collisions that produce ionizations decreases. In order to have enough collisions to produce a discharge, the voltage must be increased.

It follows that plasma cannot form in the pores of $CaCO_3$ particles within the plasma zone, since their diameter is below 2 µm.

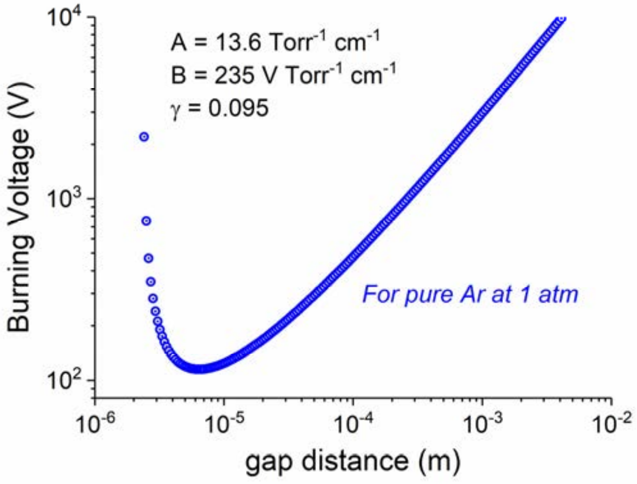

Figure A3.1. *Burning voltage in function of the gap distance for argon at 1 bar, adapted by [58].*

In order to discriminate whether the gas temperature increment or the active species drives the $CaCO_3$ decomposition in presence of plasma, we compared the effect of plasma on the reaction rate on samples with different specific surface area and perform a similar comparison for samples with different particles size. By choosing different particles sizes or different specific surface areas, we can vary selectively the external surface, exposed to the active species and temperature increase, and the internal surface, exposed only to a temperature increase.

Determination of Plasma Power

The Lissajous plot measured during decomposition of sample C in Ar with 3200 ppm extra CO_2 and plasma power 1.5 W, indicating plasma charge as function of voltage for one cycle, is shown in Figure A3.2. The hysteresis has a shape of parallelogram, indicating that a plasma is generated inside the reactor. The slopes of the two sides indicate respectively a cell capacity of 2.8 pF with plasma off and an effective capacity of 8 pF corresponding to the dielectric capacity and indicating that the plasma occupies the whole empty volume within the electrodes. The power of the plasma is calculated based on the area of the parallelogram:

$$P = \frac{1}{T} \cdot \int_0^T V dQ \qquad (3.1)$$

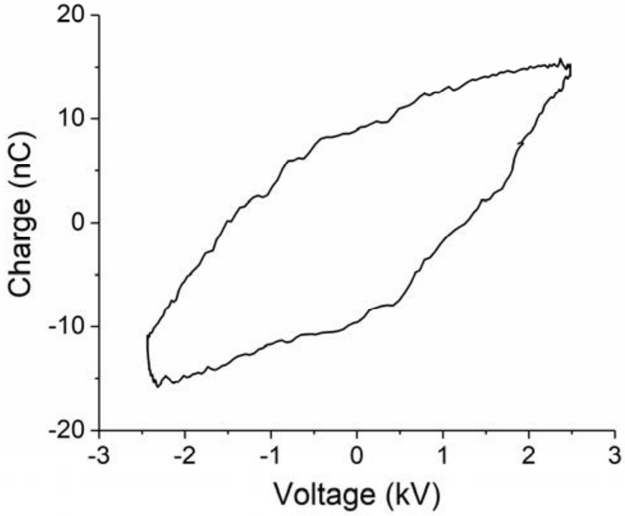

Figure A3.2: *Lissajous plot of 1.5 W plasma applied on the $CaCO_3$ and Al_2O_3 mixture with 3200 ppm of CO_2 in Ar.*

Heat Transfer in the Packed Bed

Plasma is considered as a uniform heat source at temperature T_∞ around the particles which are assumed spherical and have an initial temperature T_0. We calculated the time needed to increase the temperature of the centre of the particles of the 90% of the initial temperature difference $T_\infty – T_0$ as follows [59]

$$t = \frac{\rho C_p V}{hA} \ln\left(\frac{T_0 - T_\infty}{T - T_\infty}\right) \qquad (3.2)$$

The physical constants in the equation are the following: ρ is the density of $CaCO_3$ (2710 kg/m^3); C_p is the heat capacity of $CaCO_3$ at 630 °C (1.26 $J\ g^{-1}\ K^{-1}$) [60]; V and A are the volume and section of the $CaCO_3$ particles, respectively, and h is the convective heat transfer coefficient of a dry gas in a packed bed reactor, approximated to 15 W m^{-2} K^{-1} [59]. As a result, the times needed to heat up the particles are respectively 4, 11, and 24 seconds for the smallest (38–45 μm), medium (100–125 μm), and largest (250–300 μm) particles, respectively. Equation (3.3) is an approximation for spherical particles without porosity, so we assume that more accurate calculation will give slightly longer times.

Decomposition in argon plasma of all the samples

Figures A3.3–A3.7 show the results of all the $CaCO_3$ decomposition experiments on samples A–E, respectively, in presence of plasma and without recycling. The results with power higher than 6 W and further than the second step of power have been rejected due to exhaustion.

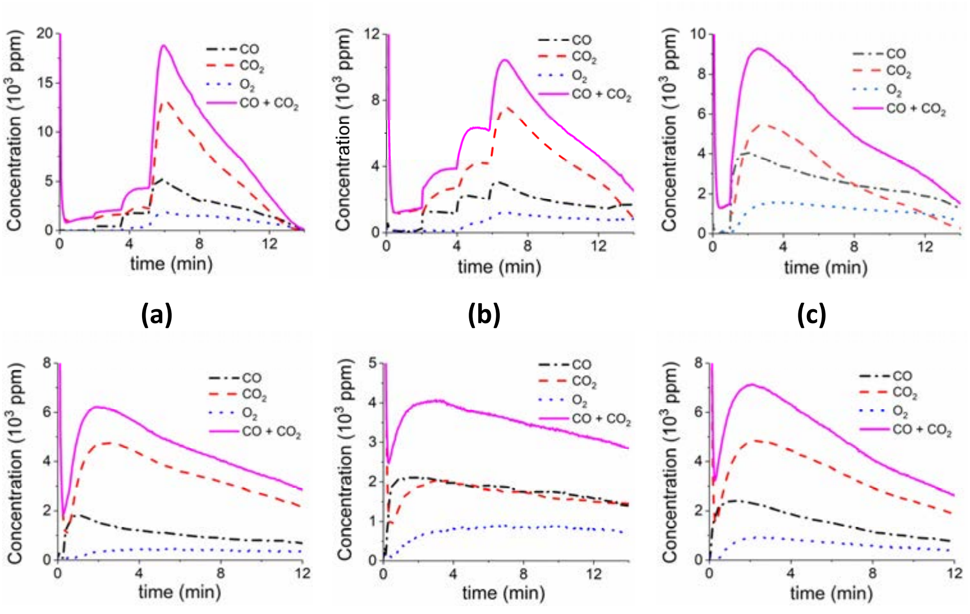

(a) (b) (c)

(d) (e) (f)

Figure A3.3. *Concentration of the products of $CaCO_3$ decomposition (sample A) as function of time at 630 °C in pure argon and flow rate of 30 mL min^{-1}. Plasma power is 0.3, 1.4, and 8.4 W* ***(a)****; 1.4, 3.5, and 6.4 W* ***(b)****; 5.1 W* ***(c)****; 3.9 W* ***(d)****; 2.2 W* ***(e)****; and 3.7 W* ***(f)****. Plasma is turned on after 2 min and changed every 2 min* ***(a,b)****, after 1.5 min* ***(c)****, or at the beginning of the decomposition* ***(d–f)****.*

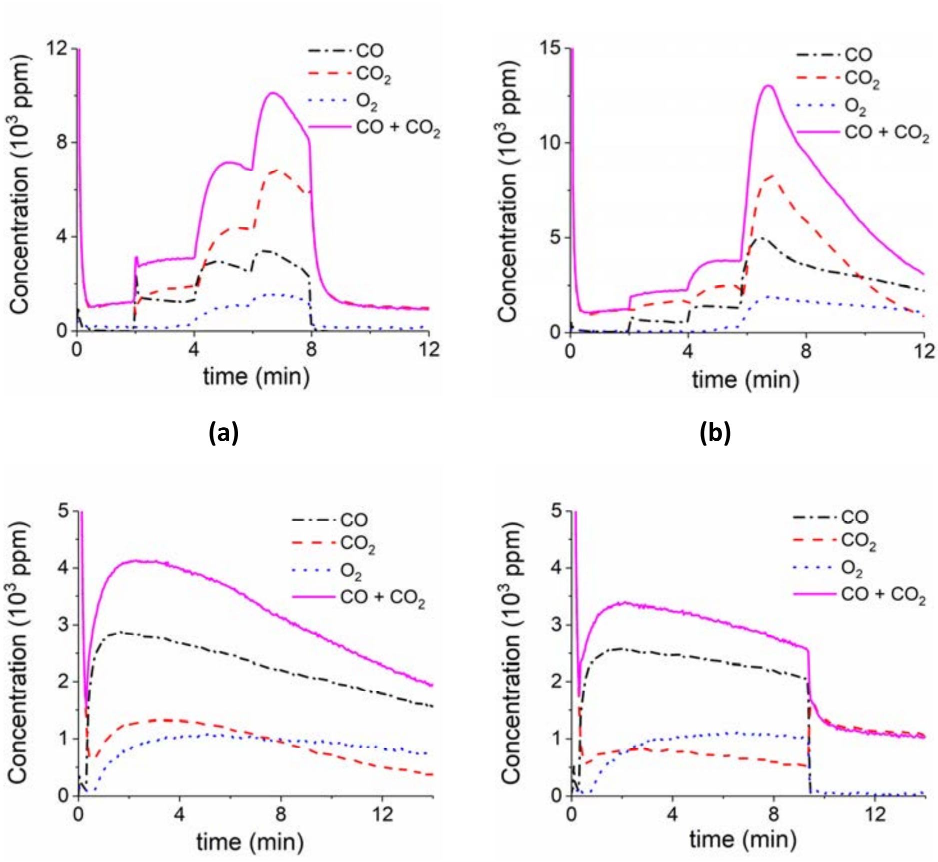

(a) **(b)**

(c) **(d)**

Figure A3.4. *Concentration of the products of* $CaCO_3$ *decomposition (sample B) as function of time at 630°C in pure argon and flow rate of 30 mL* min^{-1}*. Plasma power is 1, 4.1, and 5.8 W* ***(a)****; 0.5, 2.1, and 8.5 W* ***(b)****; and 2.1 W* ***(c,d)****. Plasma is turned on after 2 min and changed every 2 min* ***(a,b)*** *or at the beginning of the decomposition* ***(c,d)***

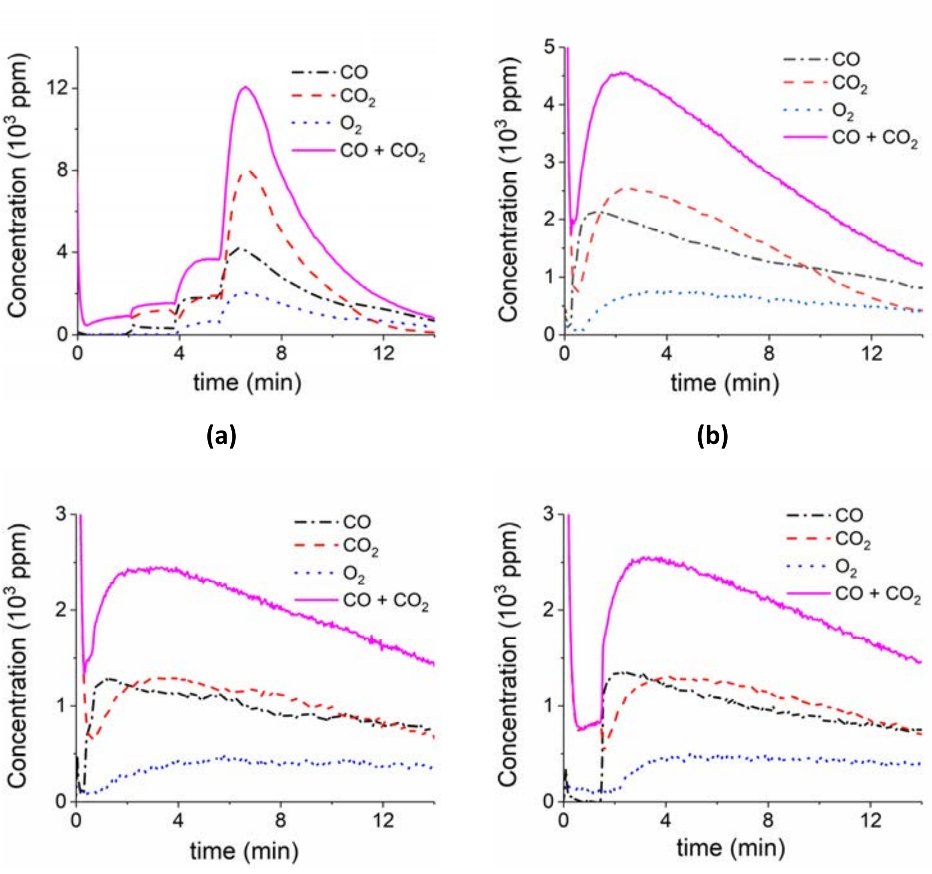

(a) **(b)**

(c) **(d)**

Figure A3.5. *Concentration of the products of $CaCO_3$ decomposition (sample C) as function of time at 630 °C in pure argon and flow rate of 30 mL min^{-1}. Plasma power is 0.4, 3.2, and 9.6 W* ***(a)****; 4.4 W* ***(b)****; and 2.1 W* ***(c,d)****. Plasma is turned on after 2 min and changed every 2 min* ***(a)*** *or at the beginning of the decomposition* ***(b,c)*** *or after 1.5 min* ***(d)****.*

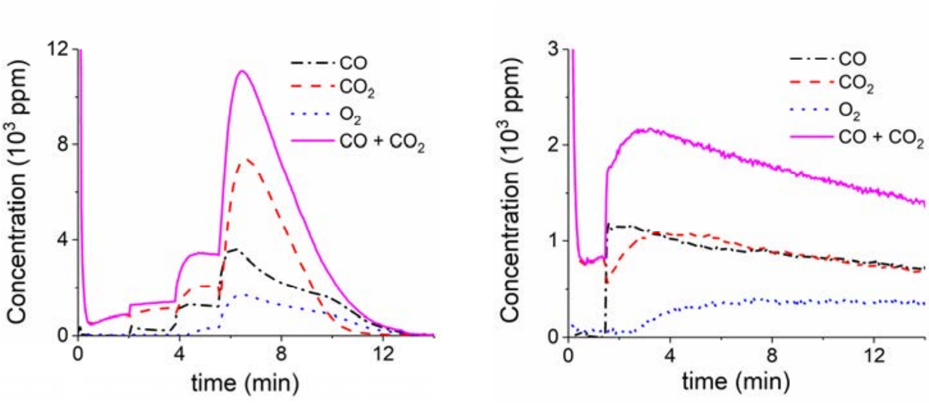

(a) (b)

Figure A3.6. *Concentration of the products of $CaCO_3$ decomposition (sample D) as function of time at 630 °C in pure argon and flow rate of 30 mL min^{-1}. Plasma power is 0.2, 2.3, and 8.1 W* ***(a)*** *and 1.3 W* ***(b)****. Plasma is turned on after 2 min and changed every 2 min* ***(a)*** *or after 1.5 min* ***(b)****.*

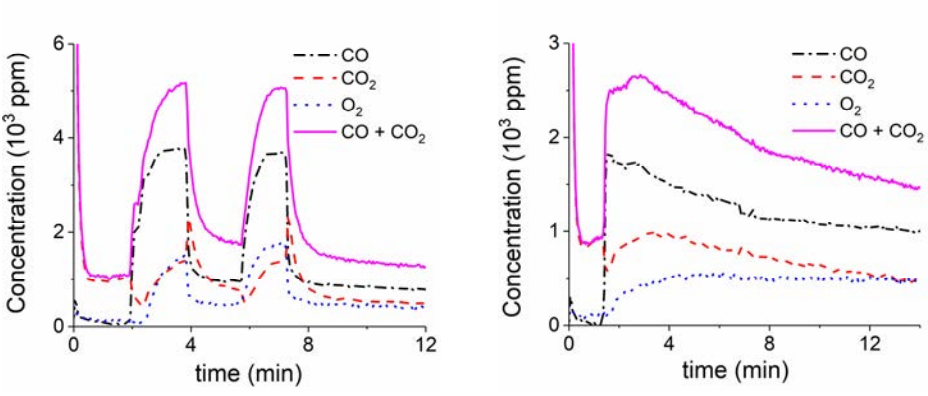

(a) (b)

Figure A3.7. *Concentration of the products of $CaCO_3$ decomposition (sample E) as function of time at 630 °C in pure argon and flow rate of 30 mL min^{-1}. Plasma power is 4.4, 1, 4.9, and 1 W* ***(a)*** *and 1.7 W* ***(b)****. Plasma is turned on after 2 min and changed every 2 min* ***(a)*** *or after 1.5 min* ***(b)****.*

Figures A3.8–A3.11 show the results of all the $CaCO_3$ decomposition experiments on sample C in presence of plasma when the sample is recycled 20 times, including experiments with extra CO_2 added.

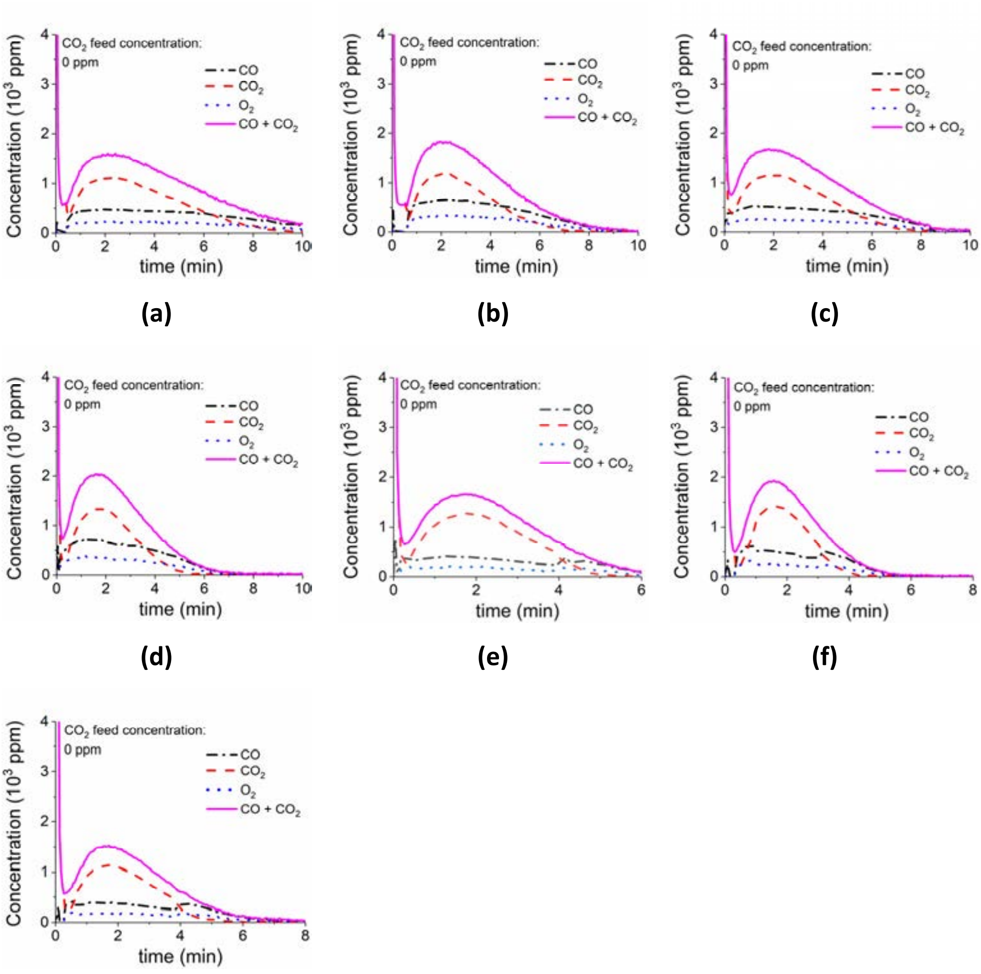

(a) (b) (c)

(d) (e) (f)

(g)

Figure A3.8. *Concentration of the products of CaCO$_3$ decomposition (sample C) as function of time at 630 °C, flow rate of 90 mL min^{-1}. The fed CO$_2$ concentration is 0 ppm and the plasma power is 1.5 W* ***(a)****, 2.1 W* ***(b)****, 1.7 W* ***(c)****, 2.2 W* ***(d)****, 1.5 W* ***(e)****, 2 W* ***(f)****, and 1.1 W* ***(g)****. The plasma is applied at the beginning of the reaction.*

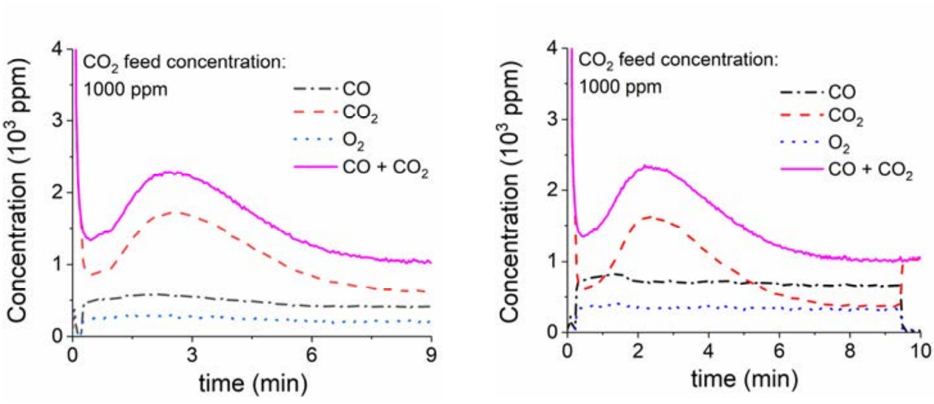

(a) **(b)**

Figure A3.9. *Concentration of the products of $CaCO_3$ decomposition (sample C) as function of time at 630 °C, flow rate of 90 mL min^{-1}. The fed CO_2 concentration is 1000 ppm and the plasma power is 1.3 W* ***(a)*** *and 1.5 W* ***(b)****. The plasma is applied at the beginning of the reaction.*

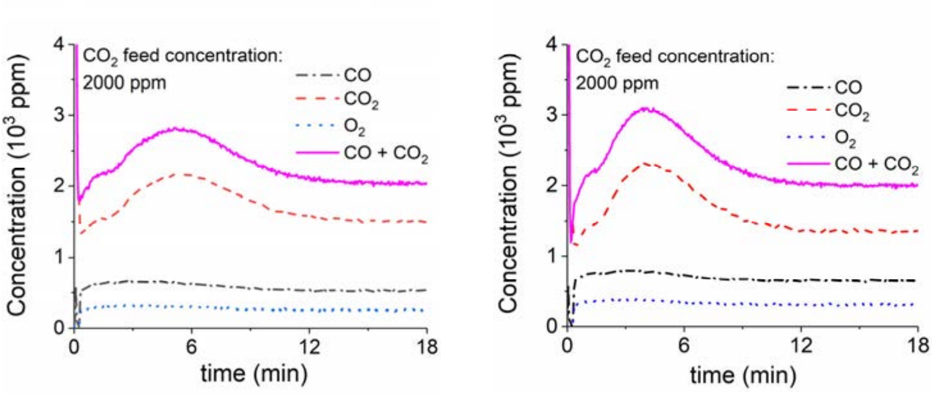

(a) **(b)**

Figure A3.10. *Concentration of the products of $CaCO_3$ decomposition (sample C) as function of time at 630 °C, flow rate of 90 mL min^{-1}. The fed CO_2 concentration is 2000 ppm and the plasma power is 1.4 W* ***(a)*** *and 1.9 W* ***(b)****. The plasma is applied at the beginning of the reaction.*

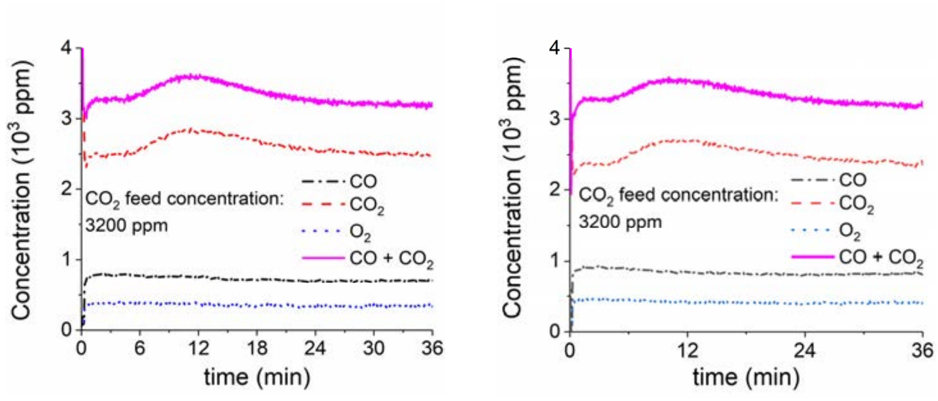

(a) **(b)**

Figure A3.11. *Concentration of the products of $CaCO_3$ decomposition (sample C) as function of time at 630 °C, flow rate of 90 mL min^{-1}. The fed CO_2 concentration is 3200 ppm and the plasma power is 1.4 W **(a)** and 1.5 W **(b)**. The plasma is applied at the beginning of the reaction.*

CO_2 Dissociation with Only α-Al_2O_3

Figure A3.12 shows the result of CO_2 dissociation experiments on a sample consisting of 100 mg α-Al_2O_3 with particle size of 250–300 µm. The applied gas composition is respectively 1000 ppm **(a)**, 2000 ppm **(b)**, and 3200 ppm **(c)** in Argon. The CO concentrations at 1.5 W plasma power are obtained by interpolation and are shown in Figure 3.11.

Figure A3.13 shows the result of a $CaCO_3$ decomposition experiment at 680 °C without plasma on sample C. It is observed that the CO_2 concentration at the steady state corresponds within the error margins to the sum of CO and CO_2 concentrations during decomposition at 630 °C with 3.2 W plasma power, shown in Figure A3.5a. The comparison supports the estimation of a 50 °C increase for 3.2 W, as shown in Figure 3.12.

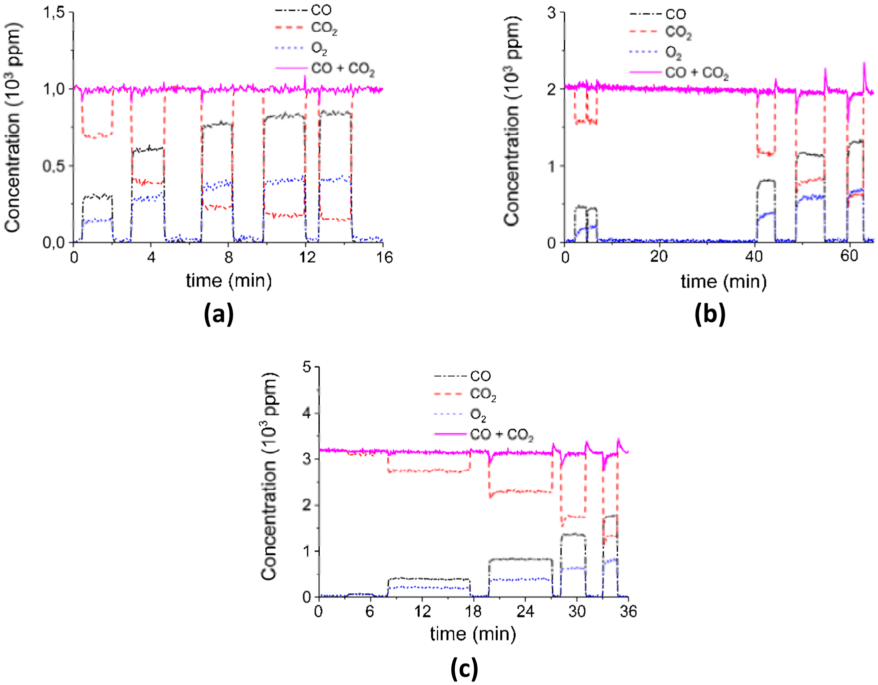

Figure A3.12. *Concentration of the products of CO_2 dissociation on 100mg α-Al_2O_3, particle size of 250-300 µm, as function of time at 630 °C, flow rate of 90 mL min^{-1}. The fed CO_2 concentration is 1000 ppm **(a)**, 2000 ppm **(b)**, and 3200 ppm **(c)**; the plasma powers are 0.6, 1.6, 3.1, 4.8, and 7.2 W **(a)**; 0.7, 1.8, 4.1, and 5.6 W **(b)**; and 0.5, 1.5, 3.1, and 4.9 W **(c)**. The plasma is applied for a few minutes and then turned off.*

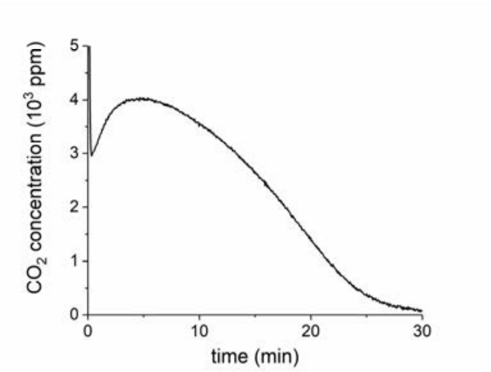

***Figure A3.13**. Concentration of CO_2 during $CaCO_3$ decomposition (sample C) as function of time at 680 °C and a flow rate of 30 mL min^{-1}.*

A4 Synergy between Dielectric Barrier Discharge Plasma and Calcium Oxide for Reverse Water Gas Shift

Lissajous plots

Figure A4.1 shows the Lissajous plots calculated during RWGS experiment on “Al_2O_3” and “CaO + Al_2O_3” at the same conditions. The plots indicate no significant change in the plasma when CaO is added.

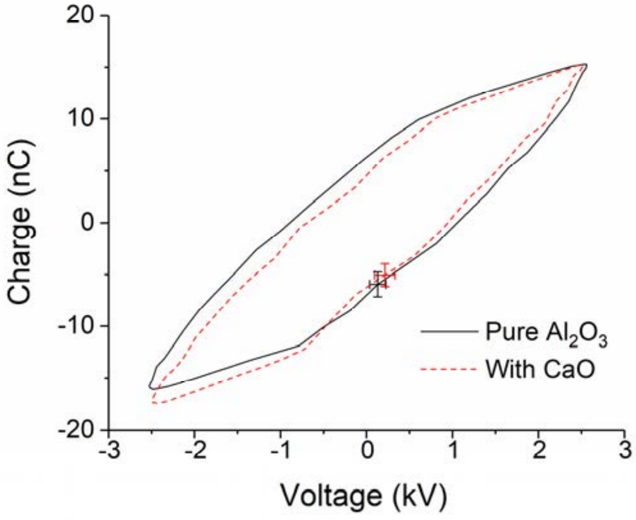

Figure A4.1*: Lissajous plots measured in presence of plasma on Al_2O_3 only (solid line) and in addition of CaO (dashed line); plasma power is 1W, flow rate is 90ml min^{-1}, temperature is 640°C, feed is 0.3% CO_2, 10% H_2 and 0% H_2O in Ar.*

Experiments

Figures A4.2 and A4.3 show the concentration of the outlet gases during RWGS on “Al_2O_3”, “CaO + Al_2O_3” respectively in thermal operation.

Figure A4.4 shows deactivation of “CaO + Al_2O_3” occurring during the first 3 hours of experiment.

Figure A4.5 shows the concentration of the outlet gases during RWGS on “$CaCO_3$ + Al_2O_3” in thermal operation.

Figures A4.6 and A4.7 shows the concentration of the outlet gases during RWGS on “Al_2O_3” and “CaO + Al_2O_3” respectively in plasma operation.

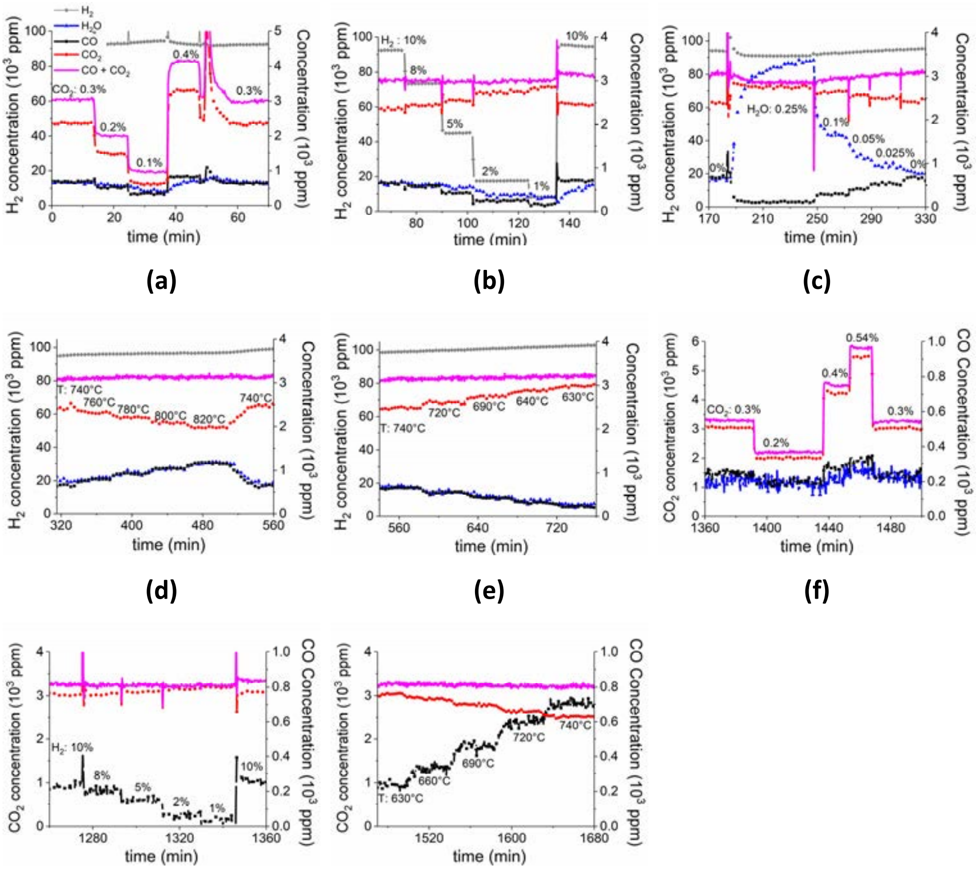

(a) **(b)** **(c)**

(d) **(e)** **(f)**

(g) **(h)**

***Figure A4.2a-h**: Outlet concentration of CO (■), CO_2 (●), H_2 (◆), H_2O (▲) and CO + CO_2 (—) as function of time during experiments of RWGS on 100mg of Al2O3; **(a)**: feed is 10% H_2 and 0% H2O, temperature is 740°C; **(b)**: feed is 0.3% CO_2 and 0% H_2O, temperature is 740°C; **(c)**: feed is 0.3% CO_2, 10% H_2, temperature is 740°C; **(d,e)**: feed is 0.3% CO_2, 10% H_2, 0% H_2O; **(f)**: feed is 10% H_2 and 0% H_2O, temperature is 630°C; **(g)**: feed is 0.3% CO_2 and 0% H_2O, temperature is 630°C; **(h)**: feed is feed is 0.3% CO_2, 10% H_2, 0% H_2O; flow rate is 90 ml min^{-1} and no plasma is applied.*

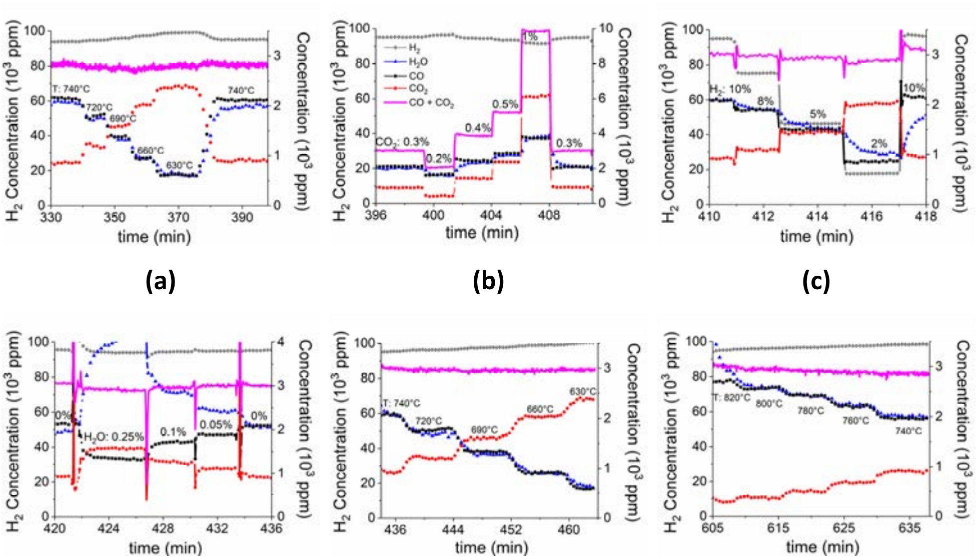

(a) **(b)** **(c)**

(d) **(e)** **(f)**

Figure A4.3a-f*: Outlet concentration of CO (■), CO_2 (●), H_2 (◆), H_2O (▲) and CO + CO_2 (—) as function of time during experiments of RWGS on 7mg CaO and 95mg of Al2O3;* ***(a)****: feed is 0.3% CO2, 10% H_2 and 0% H_2O;* ***(b)****: feed is 10% H_2 and 0% H_2O, temperature is 740°C;* ***(c):*** *feed is 0.3% CO_2, 0% H_2O, temperature is 740°C;* ***(d)****: feed is 0.3% CO_2, 10% H_2, temperature is 740°C;* ***(e,f)****: feed is 0.3% CO_2, 10% H_2, 0% H_2O; flow rate is 90 ml min^{-1} and no plasma is applied.*

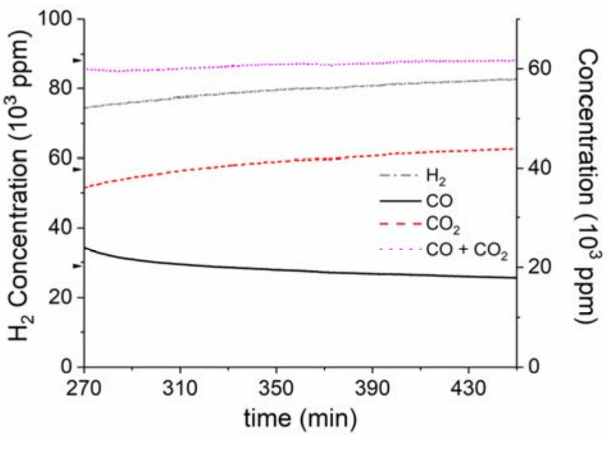

Figure A4.4*: Outlet concentration of CO (—), CO_2 (- -), CO + CO_2 (┈┈) and H_2 (-. -) during RWGS on "CaO + Al_2O_3" at 820°C; feed is 6% CO_2, 10% H_2, 0% H_2O; flow rate is 90 ml min^{-1}.*

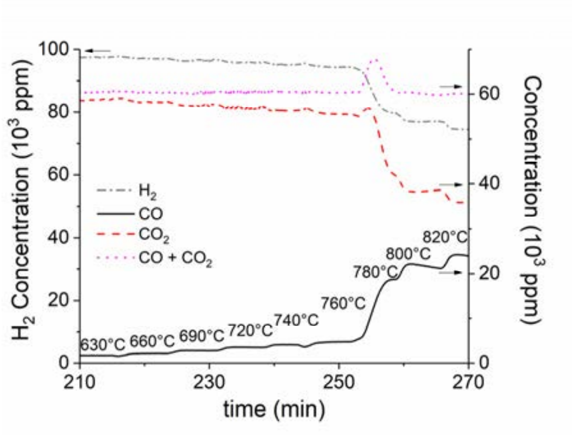

***Figure A4.5**: Outlet concentration of CO (—), CO_2 (- -), CO + CO_2 (······) and H_2 (-·-) during RWGS on "$CaCO_3$ + Al_2O_3" as function of temperature; feed is 6% CO_2, 10% H_2, 0% H_2O; the flow rate is 90 ml min^{-1}.*

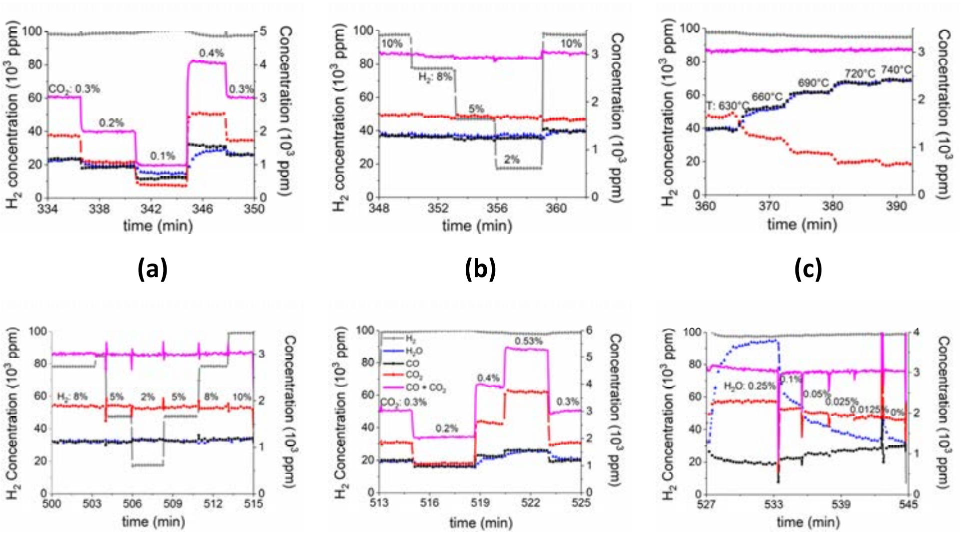

(a) **(b)** **(c)**

(d) **(e)** **(f)**

***Figure A4.6a-f**: Outlet concentration of CO (■), CO_2 (●), H_2 (◆), H_2O (▲) and CO + CO_2 (—) as function of time during experiments of RWGS on 100mg of Al_2O_3; **(a)**: feed is 10% H_2 and 0% H_2O, temperature is 640°C; **(b)**: feed is 0.3% CO_2 and 0% H_2O, temperature is 640°C; **(c)**: feed is 0.3% CO_2, 10% H_2, 0% H_2O; **(d)**: feed is 0.3% CO_2, 0% H_2O, temperature is 640°C; **(e)**: feed is 10% H_2, 0% H_2O, temperature is 640°C; **(f)**: feed is 0.3% CO_2, 10% H_2, temperature is 640°C; flow rate is 90 ml min^{-1} and plasma power is 1W.*

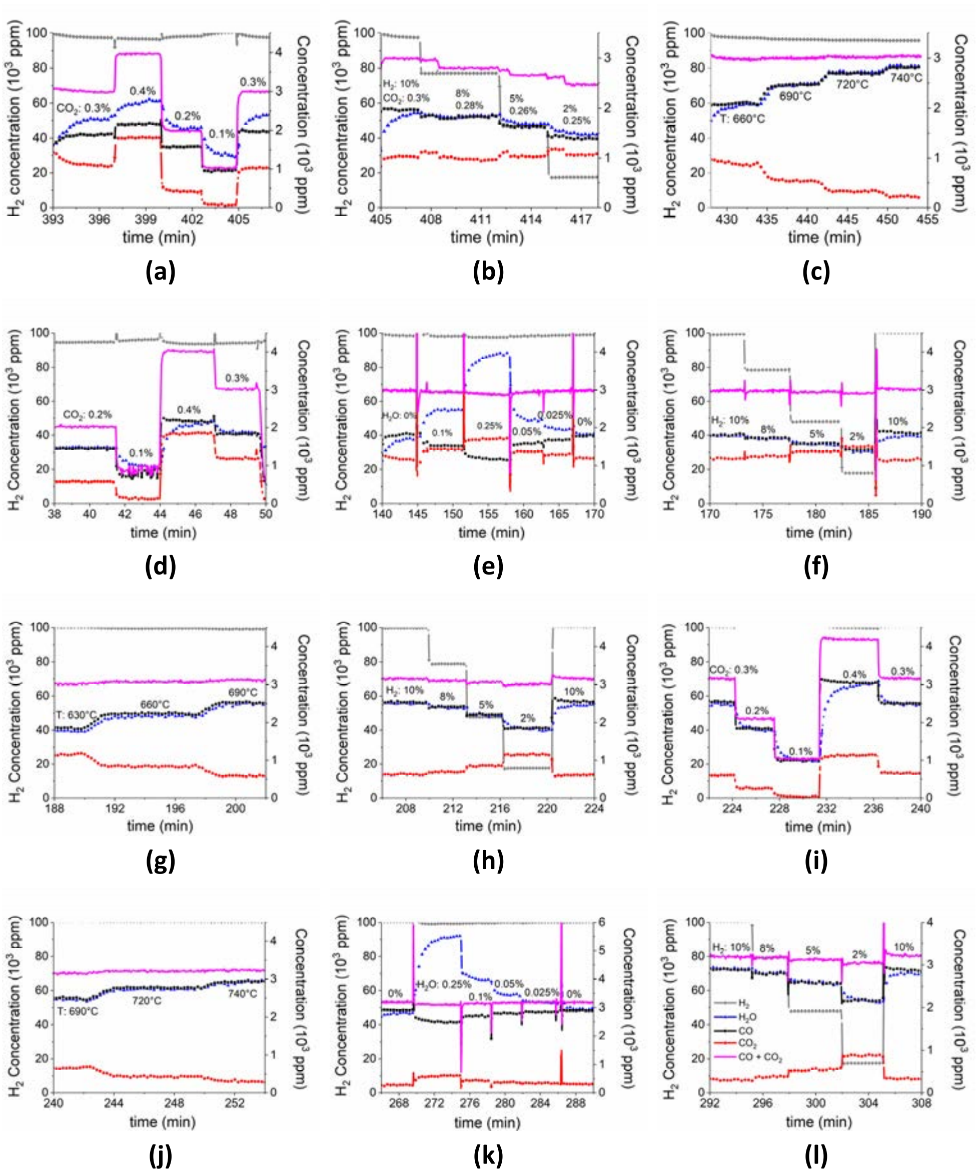

(a) (b) (c)

(d) (e) (f)

(g) (h) (i)

(j) (k) (l)

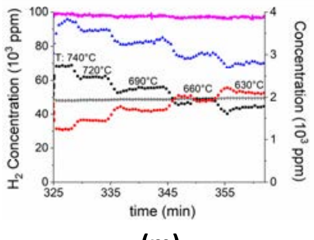

(m)

Figure A4.7a-m: *Outlet concentration of CO (■), CO_2 (●), H_2 (◆), H_2O (▲) and CO + CO_2 (—) as function of time during experiments of RWGS on 7mg CaO and 100 mg of Al_2O_3;* ***(a)****: feed is 10% H_2 and 0% H_2O, temperature is 640°C;* ***(b)****: feed is from 0.25 to 0.3% CO_2 and 0% H_2O, temperature is 640°C;* ***(c)****: feed is 0.3% CO_2, 10% H_2, 0% H_2O;* ***(d)****: feed is 10% H_2 and 0% H_2O, temperature is 640°C;* ***(e)****: feed is 0.3% CO_2, 0% H_2O, temperature is 640°C;* ***(f)****: feed is 0.3% CO_2, 0% H_2O, temperature is 640°C;* ***(g)****: feed is 0.3% CO_2, 10% H_2, 0% H_2O;* ***(h)****: feed is from 0.3% CO_2 and 0% H_2O, temperature is 700°C;* ***(i)****: feed is 10% H_2, 0% H_2O, temperature is 700°C;* ***(j)****: feed is 0.3% CO_2, 10% H_2, 0% H_2O;* ***(k)****: feed is 0.3% CO_2, 10% H_2, temperature is 750°C;* ***(l)****: feed is 0.3% CO_2, 0% H_2O, temperature is 750°C;* ***(m)****: feed is 0.4% CO_2, 5% H_2, 0.1% H_2O; flow rate is 90 ml min^{-1} and plasma power is 1W.*

Matlab script

The MATLAB script shown in the following pages uses the equation (4.2) with variables k_0, E_a, a, b and K_{H2O} to fit the CO_2 conversion levels (figures 4.2 and 4.4) by minimizing the Root Mean Square (RMS). The experimental error in the variables is estimated by varying their values, while accepting all combinations that fit all data points within their respective error margins, as illustrated in Figures 4.2 and 4.4.

```
%Introducing conditions applied for each experiment (T, Keq, [CO2]in,
[H2]in, [CO]in, [H2O]in), concentrations are expressed in ppm,
temperatures in °C.

Input = ...
[740    0.7511  3000    100000  0   2.5
720 0.6911  2980    100000  0   2.5
690 0.6054  2970    100000  0   2.5
660 0.5252  2970    100000  0   2.5
630 0.4507  3000    100000  0   2.5
740 0.7511  3000    100000  0   2.5
740 0.7511  2060    100000  0   2.5
740 0.7511  3840    100000  0   2.5
740 0.7511  5200    100000  0   2.5
740 0.7511  9850    100000  0   2.5
740 0.7511  3000    100000  0   2.5
740 0.7511  2990    80000   0   2.5
740 0.7511  2950    50000   0   2.5
740 0.7511  2880    20000   0   2.5
740 0.7511  3020    100000  0   2.5
740 0.7511  2890    100000  0   2500
740 0.7511  2950    100000  0   1000
740 0.7511  3000    100000  0   500
740 0.7511  3000    100000  0   2.5
720 0.6911  2980    100000  0   2.5
690 0.6054  2950    100000  0   2.5
660 0.5252  2960    100000  0   2.5
630 0.4507  2960    100000  0   2.5
820 1.012   3090    100000  0   2.5
800 0.9439  3030    100000  0   2.5
780 0.8776  2990    100000  0   2.5
760 0.7819  2970    100000  0   2.5
];

%Introducing concentrations measured at the outlet for each
experiment ([CO2]out, [H2]out, [CO]out, [H2O]out), expressed in ppm.

Output = ...
[860    97860   2140    2140
1150    98170   1830    1830
1600    98630   1370    1370
```

```
2020    99050   950     950
2390    99390   610     610
900     97900   2100    2100
410     98350   1650    1650
1420    97580   2420    2420
2370    97170   2830    2830
6130    96280   3720    3720
910     97910   2090    2090
1090    78100   1900    1900
1450    48500   1500    1500
2020    19140   860     860
920     97900   2100    2100
1580    98690   1310    3810
1240    98290   1710    2710
1110    98110   1890    2390
910     97910   2090    2090
1190    98210   1790    1790
1610    98660   1340    1340
2040    99080   920     920
2370    99410   590     590
300     97210   2790    2790
370     97340   2660    2660
500     97510   2490    2490
690     97720   2280    2280
];

%Introducing error margin of the CO concentrations in the outlet,
expressed in ppm.

Errppm = ...
[171
146
110
76
49
168
132
194
226
298
167
152
120
69
168
105
137
151
167
143
107
74
47
223
```

```
213
199
182
];

%Defining time step (s) and ideal gas constant (J mol-1 K-1).

t = 0.000002;
R = 8.314;

%Converting temperatures in K and concentrations in fractions.

Temp = Input(:,1) + 273;
Keq = Input(:,2);
CO2in = 1E-6.*Input(:,3);
H2in = 1E-6.*Input(:,4);
COin = 1E-6.*Input(:,5);
H2Oin = 1E-6.*Input(:,6);

CO2out = 1E-6*Output(:,1);
H2out = 1E-6*Output(:,2);
COout = 1E-6*Output(:,3);
H2Oout = 1E-6*Output(:,4);

Err = 1E-6*Errppm;

%Defining registers and collector arrays.

CO2 = [];
H2 = [];
CO = [];
H2O = [];
x = [];
xall = [];
Reg = [];
COprofileall = [];

%Scanning k0, Ea, a, b and KH2O values contained in the array x,
defining counter variables and initializing the registers.

for h = 1:5
for g = 1:8
for j = 1:6
for k = 1:6
for l = 1:5

x = [2*h*10^10 (14+0.5*g)*10^4 0.4+0.1*j 0.6+0.1*k 2*l*10^3];

m = 0;
n = 0;
i = 1;
Reg = [Temp,Keq,CO2in,H2in,COin,H2Oin];
COprofile = [];
COsample = [];
```

```
%Calculating the gases concentration within the reactor by applying
the rate equation iteratively in 10000 time steps. Note that all the
experiments are modeled at once. Temperatures and concentrations are
updated in Reg. The COprofile array collects the CO concentrations
at each step for one single experiment at our choice (e.g.
experiment 1), allowing to plot it afterward.

for i = 1:10000
    CO = Reg(:,5) + t.*(((x(1).*exp(-
x(2)./(R.*Reg(:,1))).*Reg(:,3).^x(3).*Reg(:,4).^x(4))./(1+Reg(:,6).*
x(5))));
    CO2 = CO2in - CO;
    H2 = H2in - CO;
    H2O = H2Oin + CO;
    Reg = [Temp,Keq,CO2,H2,CO,H2O];
    COsample = CO(1);
    COprofile = [COprofile, COsample];
end

%Acceptance criteria: if the CO outlet concentration of each
experiment calculated with the model fits with the experimental
data, the set of parameters in the array x is valid. If so, x will
be collected in xall and the CO concentration profiles (for each
valid x set) will be collected in COprofileall.

for m = 1:27
    if isreal(CO(m))
    A = abs(CO(m)-COout(m));
    E = Erry(m);
    if A < E
         n = n+1;
    end
    end
end
if n == 27
    COprofileall = [COprofileall; COprofile];
    xall = [xall; x];

%Ending variables scan.
end
end
end
end
end
end

%Transposing COprofileall matrix to allow copy-paste in Origin.

COprofileall = COprofileall.';
fclose('all');
```

A5 Calcium Carbonate Decomposition in a Dielectric Barrier Discharge hydrogen plasma

Decomposition in Hydrogen plasma of all the Samples

Figures A5.1–A5.4 show the results of the $CaCO_3$ decomposition experiments on samples A, B, C and D respectively, at 590°C in presence of plasma and without recycling. The results with power higher than 6 W of power have been rejected due to exhaustion.

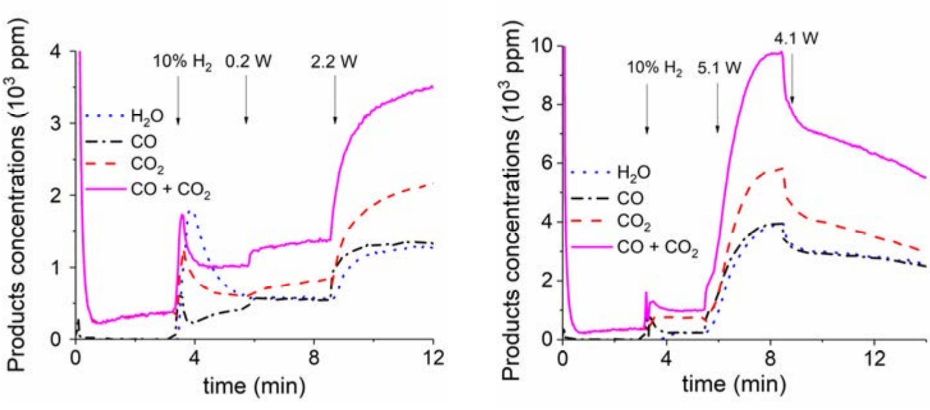

(a) **(b)**

Figure A5.1. *Concentration of the products of $CaCO_3$ decomposition (sample A) as function of time at 590°C in pure Ar and 10% H_2 in Ar and flow rate of 30 ml min^{-1}. Plasma power is 0.2 and 2.2 W **(a)**; 5.1 and 4.1 W **(b)**. Hydrogen is introduced after 3 to 4 min; plasma is turned on after 6 min and changed every 2 to 4 min.*

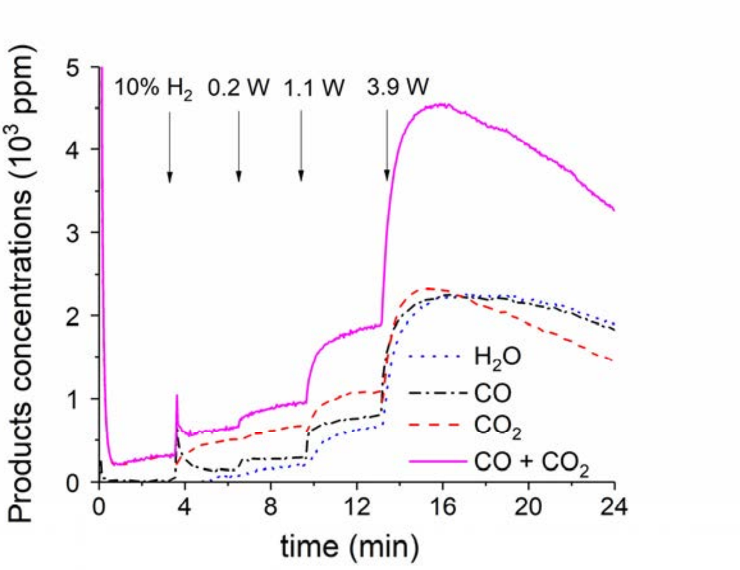

Figure A5.2. *Concentration of the products of $CaCO_3$ decomposition (sample B) as function of time at 590°C in pure Ar and 10% H_2 in Ar and flow rate of 30 ml min^{-1}. Plasma power is 0.2, 1.1 and 3.9 W. Hydrogen is introduced after 4 min, plasma is turned on after 6 min and changed every 4 min.*

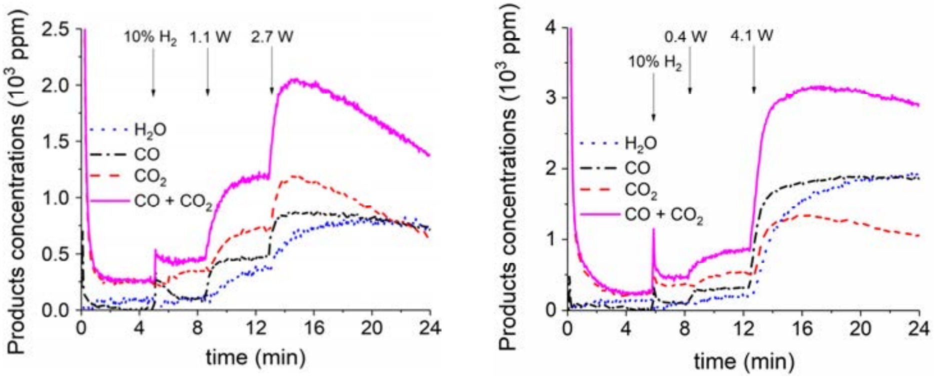

(a) **(b)**

Figure A5.3. *Concentration of the products of $CaCO_3$ decomposition (sample C) as function of time at 590°C in pure Ar and 10% H_2 in Ar and flow rate of 30 ml min^{-1}. Plasma power is 1.1 and 2.7 W* ***(a)****; 0.4 and 4.1 W* ***(b)****. Hydrogen is introduced after 5 min; plasma is turned on after 8 min and changed every 4 to 5 min.*

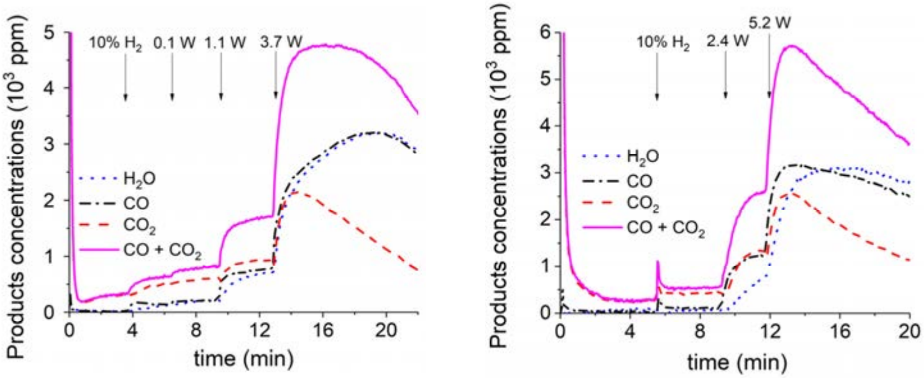

(a) **(b)**

Figure A5.4*. Concentration of the products of $CaCO_3$ decomposition (sample D) as function of time at 590°C in pure Ar and 10% H_2 in Ar and flow rate of 30 ml min^{-1}. Plasma power is 0.1, 1.1 and 3.7 W* ***(a)****; 2.4 and 5.2 W* ***(b)****. Hydrogen is introduced after 4 to 6 min; plasma is turned on after 6 to 9 min and changed every 3 to 4 min.*

Acknowledgements

And so, it begins. The most difficult part of this work, starring at this blank page trying to find the right words for the people which supported me during this journey, which made it possible for me to achieve this goal. Only by acknowledging all of you, this thesis will be complete.

When I look back at this journey's beginning in CPM, I see a fresh PhD student walking in Leon's office, trying to deal with a whole new scientific research field. Even though I usually had only confusing results which could barely answer some not well defined question, Leon was always ready to share with me his knowledge and expertise, to involve me in those scientific discussions driven by both pickiness and curiosity, to challenge me by playing the devil's advocate, sometimes with animosity, to keep me on track when I wandered and, most important, to let me deal with setbacks. I am lucky to have had him as guide and co-worker, God knows how I already miss all of this!

Nevertheless, my adventure started long before and two nice ladies were involved. Already one day before my intake interview, Kamilla opened me the forbidden door and accompanied me to Maaike, who simply made me feel at home. I cannot thank both of you for the help you gave me.

Seshan, I followed that advice you gave me during the intake: I went out from my nest and lived in a different country, the very thing that made this possible. What I gained is invaluable. You helped me a lot with your scientific contribution, always with a smile.

What is as worthy as a smile? Your menacing look, Bert, which I got every time I tried to access your Sanctum. When I step in (if allowed, always bowing), I'm aware that "I know nothing" and you know everything, it's a rule of nature. I only know that I could ask for anything and you were always willing to help, not only for technical, but also for personal issues. You are the most reliable person that I know, and I won't never thank you enough for that. Since you are an Emperor, you want to be pleased and I know how to do it… of course paying a round!

The technical staff was also of a great help. Karin, maybe sometimes I was a bit of a challenge for your nerves because of my messiness, but you were still patient, and you taught me a lot about BET. Tom, you gave me a lot of help with the XRF and TGA. Also, that concert in Hengelo was amazing, I think Alessandro enjoyed it from inside the belly.

Maaike, Jacqueline, Dorothy and finally Anne, thanks to all of you for making my life in CPM easier and funnier, sometimes adventurous during the group trips.

Jimmy, you were the last to arrive, but you really brought good latino vibes. With your knowledge I believe you can do very good things, both for your career and for the group. Thanks for the scientific discussions and para la deliciosa comida con tu familia.

Thanks a lot also to Michael and Tesfaye, you hosted me at DIFFER and helped me with complex DRIFTS measurement.

And so, CPM was like home. Several colleagues helped me bridging the gap between Physics and Chemistry. Pramod, Songbo, Kamilla, Kaisa, Roger, Joline, Chau, Rao, Jie, Yingnan, Tushar, Shilpa, Marta, Reza, Rolf, Pengyu, Maria, Nuria, Peppe, Kevin, Pengchen, I learned a lot from all of you, both on theory and working in the lab. Although you represent for me different generations, for me was a continuity of great life, hard work and even harder fun.

The office ME363 was a lovely place to spend time analyzing data and writing papers. Rolf, it was great to share the office with you, talking about everything, from science to Italian lessons, or simply making nasty jokes. Thanks also to Erwin, you helped me a lot to correct my google Dutch.

And then Friday comes, 5 o’clock, ring the bell!! Suddenly the coffee table becomes full of life. Songbo and Bert hide behind their empty beer bottles. Careful with the Emperor, don’t break the rules or pay one round! Roger, Tushar, Marta and Pramod, is a fact that an evening started with you could end up either in some diplomatic issues with the Iranian community, or in a bus to Prague, or simply dancing on the table. Kamilla, with you I mastered the subtle art of Saboteur. And then the next generation, going from political debates between James and the rest of the table, Pengyu teaching the good Chinese, Shahab and Kevin going on a whiskey competition, Maria teaching dirty Portuguese songs and then the frittissimi Peppe and Nuria singing karaoke… even though we ended barking sometimes, our good times were never enough!!

Talking about good times, I can safely say that most of them I lived together with my friends and paranimphs, Francesco and Federica. I think it is not possible and maybe not wise to unravel what occurred during these 5 years. Certainly, we had a lot of fun and lack of sleep, with many blurry memories and, as only proof, the expensive bills in

Friends. You both are on fire and gave me a lot of energy (or was because we drank 10 coffees per day???), which made for me the difference during these years.

Francesco, the dinners at your place were a must, Bert is still asking of that particular pasta you made at 4 in the morning… or, just to mention it, the ticket for London booked on the spot together with Mariangela. Hanging out with you, Hassan, Dimitri, Himanshu and Liqun were among the best moments lived in my life, I really miss you guys.

Federica, I don't need to mention any situation, your phone memory talks for itself…just one, the day we were elected in P-NUT, which at the end turned out to be a great experience, even though it is mostly your fault… like this, all what we did felt just different and fun. The parties in Stadsweide 303, when you were still an old sponge, reminded me of the Erasmus… you should start again to organize them, and gather back great people such as Valentina, Angelos, Josè, Alvaro, Alex, Alessio, Sirio, Fanny, the Greek girls, and many others.

Talking about P-NUT, I want to thank the other board members for the great experience and the work done together.

With the following people as housemates there was no need to go out to have good times: Bahruz the "Tigerrr", you brought the good spirit in the house, sometimes teaching me your combat skills in the early morning, other times singing "Besame Mucho" in a choir. Josh, Mourad, Ernesto, you made of that house a real jungle, staying there with you was never boring, only…. sorry for the nuisances 😊.

The Flying Nerds also deserve a special thanks, I spent amazing summer evenings with you playing beach volley or drinking beers at de Vluchte.

I met indeed a lot of people, some good friends, and most of them are now spread around the world. There is a saying: "the best ones are always the ones who leave", thus let's acknowledge the worst people that are still here, the gang of rotti nel cranio, which represent our large family in Enschede: Luigi "il Saggio", Iris, Califano, Sara, Ongaro (which is still present with his soul), Kenneth "uncle of the year", Raffa, the "trio" Daniele, Lara, and Mike, and others.

From Italy, I would like to thank Costantino, since he supports me every time and which is a brother rather than a friend.

In this colorful environment, what just happened is… a small family!

Thanks to mamma Michela and to the piccolo Alessandro, my little pucianello. You both support me every time and make every single day sound of happiness. I love you.

Finally, I want to acknowledge my family. Grazie di cuore per tutto l’amore e il coraggio che mi date ogni giorno. Quello che ho e quello che sono è solo grazie a voi.

List of publications

G. Giammaria, and L. Lefferts. Catalytic Effect of Water on Calcium Carbonate Decomposition. *J. CO_2 Util.* 2019, 33, 341-356.

G. Giammaria, G. van Rooij, and L. Lefferts. Plasma Catalysis: Distinguishing between Thermal and Chemical Effects. *Catalysts* 2019, 9, 2, 185.

G. Giammaria, and L. Lefferts. Synergy between Dielectric Barrier Discharge Plasma and Calcium Oxide for Reverse Water Gas Shift. Accepted on *Chem. Eng. J.*

List of oral and poster presentations

Oral

G. Giammaria, and L. Lefferts. Calcium carbonate decomposition enhanced by DBD plasma. NCCC XIX 2018 Noordwijkerhout, The Netherlands.

G. Giammaria, and L. Lefferts. Plasma enhanced $CaCO_3$ hydrogenation for direct fuel production. ISPC 24 2019 Naples, Italy.

Posters

G. Giammaria, and L. Lefferts. Plasma enhanced $CaCO_3$ hydrogenation for direct fuel production. EUROPACAT 2019, Aachen, Germany and NAM 2019, Chicago, IL.

G. Giammaria, and L. Lefferts. Plasma enhanced $CaCO_3$ hydrogenation for direct fuel production. EUROPACAT 2019, Aachen, Germany.

G. Giammaria, and L. Lefferts. $CaCO_3$ decomposition assisted by plasma to convert CO_2 into fuels. WELTPP Summer School 2016, Bad Honnef, Germany.

G. Giammaria, and L. Lefferts. Steam as a catalyst for $CaCO_3$ decomposition. EUROPACAT 2017, Florence, Italy and NAM 2017, Denver, CO.

G. Giammaria: poster presentations at NCCC 2015-17 and 2019, Noordwijkerhout, The Netherlands.

G. Giammaria: poster presentations at Physics@FOM 2016-17, Veldhoven, The Netherlands.

G. Giammaria: poster presentations at MESA+ Day 2015-16, Enschede, The Netherlands.

About the author

Guido Giammaria was born in Anagni, Italy on the 22nd of November 1985. He began a bachelor's degree in electrical engineering at the University of Rome "La Sapienza" in 2004. After obtaining his degree in 2009, he joined the master's degree in Nanotechnology Engineering at the same university. During this period, he performed an internship at the Interuniversity Microelectronics Center (IMEC) for 6 months, in 2013. Under the supervision of Umberto Celano, he characterized the reset transition of CB-RAM Resistive Memory devices by using Conductive – Atomic Force Microscopy (C-AFM), resulting in a master thesis dissertation. Following his passion for material science and characterization, Guido began his Ph.D. studies in 2014 at the Catalytic Processes and Materials group at the University of Twente. During his research under the supervision of Prof. Leon Lefferts, Guido gained further insights into the complexity of the interaction between a solid phase, namely decomposing calcium carbonate, and a non-thermal plasma phase. These findings are described in the present thesis. Alongside his Ph.D. work, Guido also joined the PhD Network at the University of Twente (P-NUT) in the role of president, which helps organising social and informative events.

Guido Giammaria was born in Anagni, Italy, in 1985. He obtained a bachelor's degree in electrical engineering at the University of Rome “La Sapienza” in 2009, then he joined the master's degree in Nanotechnology Engineering at the same university. During this period, he performed an internship at IMEC, Leuven, in 2013, characterizing Resistive Memory devices by using Conductive – Atomic Force Microscopy (C-AFM), resulting in a master thesis dissertation. Following his passion for material science and characterization, Guido began his Ph.D. in 2014 at the Catalytic Processes and Materials group. During his research, Guido gained further insights into the complexity of the interaction between a decomposing solid, namely $CaCO_3$, and a non-thermal plasma. These findings are described in the present thesis. Alongside his Ph.D. work, Guido also joined the PhD Network at the University of Twente (P-NUT) in the role of chair, which helps organising social and informative events.

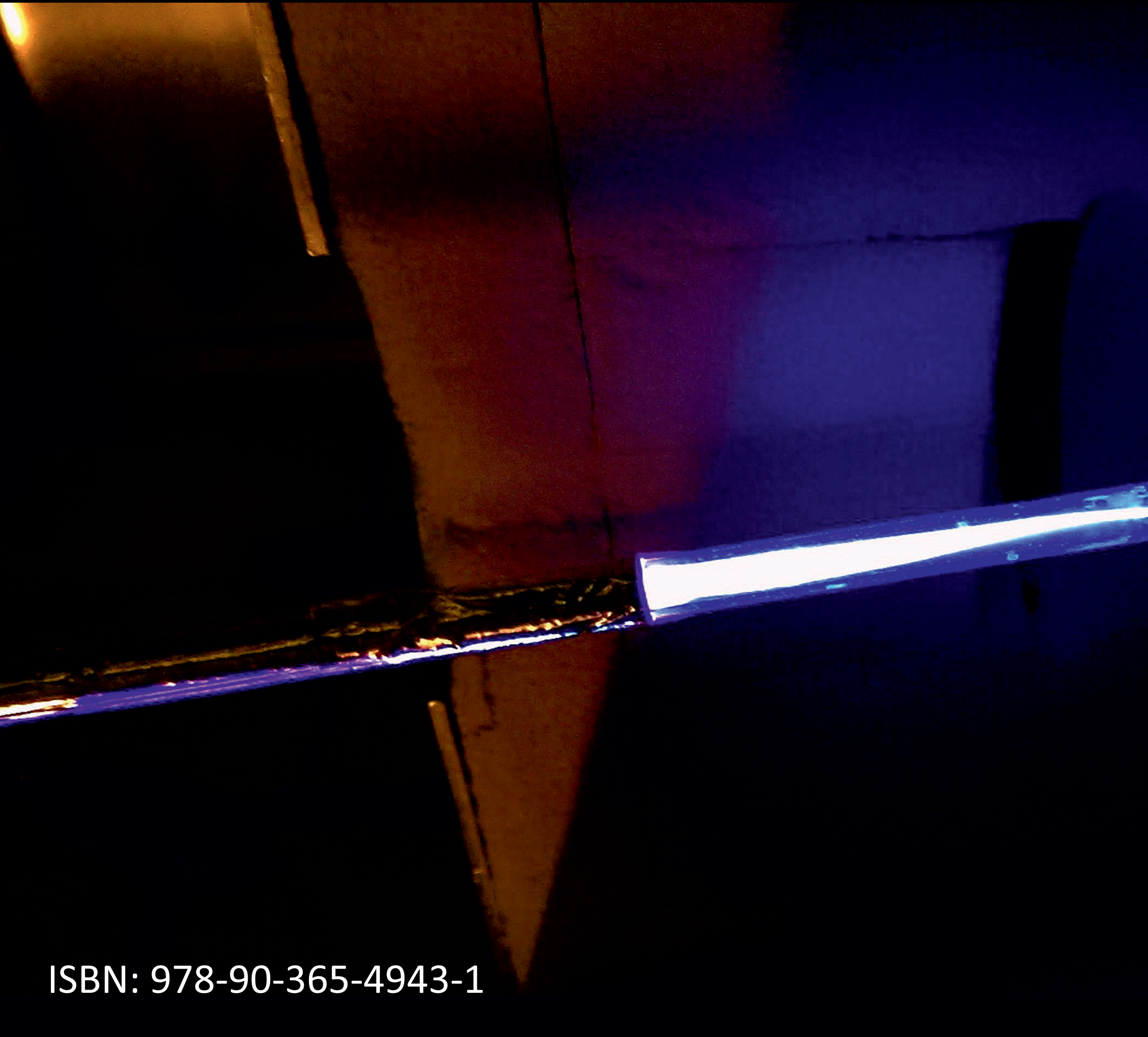

ISBN: 978-90-365-4943-1